UNIVERSIDADE FEDERAL DE SANTA CATARINA
CAMPUS FLORIANÓPOLIS
PROGRAMA DE PÓS-GRADUAÇÃO EM CIÊNCIA E ENGENHARIA DE MATERIAIS

Larissa da Silva Marques

Sol-gel synthesis of V and Ce-doped $Ba_{0.85}Ca_{0.15}Ti_{0.9}Zr_{0.1}O_3$: structural, dielectric, ferroelectric, and piezoelectric analysis

Florianópolis
2024

Larissa da Silva Marques

Sol-gel synthesis of V and Ce-doped $Ba_{0.85}Ca_{0.15}Ti_{0.9}Zr_{0.1}O_3$: structural, dielectric, ferroelectric, and piezoelectric analysis

Tese submetida ao Programa de Pós-Graduação em Ciência e Engenharia de Materiais da Universidade Federal de Santa Catarina como requisito parcial para a obtenção do título de Doutora em Ciência e Engenharia de Materiais.

Orientador: Prof., Dr. Carlos Renato Rambo
Coorientador: Prof., Dr. Tobias Fey

Florianópolis
2024

Marques, Larissa da Silva
Sol-gel synthesis of V and Ce-doped Ba0.85Ca0.15Ti0.9Zr0.1O3 : structural, dielectric, ferroelectric, and piezoelectric analysis /Larissa da Silva Marques ; orientador, Carlos Renato Rambo, coorientador, Tobias Fey , 2024.
109 p.

Tese (doutorado) - Universidade Federal de Santa Catarina, Centro Tecnológico, Programa de Pós-Graduação em Ciência e Engenharia de Materiais, Florianópolis, 2024.

Inclui referências.

1. Ciência e Engenharia de Materiais. 2. Sol-gel. 3. BCZT. 4. Dopagem. 5. Piezoelétricos. I. Rambo, Carlos Renato . II. Fey , Tobias . III. Universidade Federal de Santa Catarina. Programa de Pós-Graduação em Ciência e Engenharia de Materiais. IV. Título.

Larissa da Silva Marques

Sol-gel synthesis of V and Ce-doped $Ba_{0.85}Ca_{0.15}Ti_{0.9}Zr_{0.1}O_3$: structural, dielectric, ferroelectric, and piezoelectric analysis

O presente trabalho em nível de Doutorado foi avaliado e aprovado, em 26 de julho de 2024, pela banca examinadora composta pelos seguintes membros:

Prof.(a) Celso Peres Fernandes Dr.
Instituição Universidade Federal de Santa Catarina (UFSC)

Prof. Fabiano Raupp Pereira, Dr.
Universidade do Extremo Sul Catarinense (UNESC)

Prof. Sérgio Michielon de Souza, Dr.
Instituição Universidade Federal do Amazonas (UFAM)

Prof. Renato Henriques de Souza, Dr.
Instituição Universidade Federal do Amazonas (UFAM)

Certificamos que esta é a versão original e final do trabalho de conclusão que foi julgado adequado para obtenção do título de Doutora em Ciência e Engenharia de Materiais.

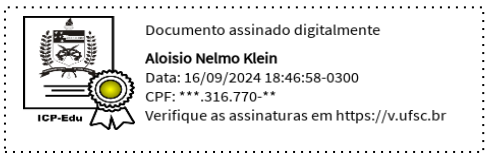

Coordenação do Programa de Pós-Graduação

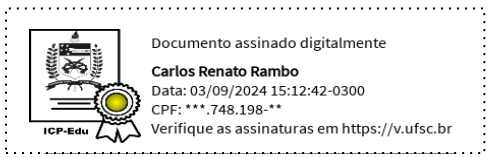

Prof. Carlos Renato Rambo, Dr.
Orientador

Insira neste espaço a

assinatura digital

Coorientador

Florianópolis, 2024.

ACKNOWLEDGEMENTS

Several people were vital while writing this thesis and working on this project. I hope to acknowledge them all. First, I would like to thank my colleagues at UFSC (Universidade Federal de Santa Catarina), laMatE (Laboratório de Materiais Elétricos), and my advisor, Professor Carlos Renato Rambo. I would also like to thank PGMAT (Programa de Pós-graduação em Ciência e Engenharia de Materiais) for their support. I am grateful to my colleagues at the WW3 (Glass and Ceramics Department) at FAU (Friedrich-Alexander-Universität Erlangen-Nürnberg), specifically, Professor Tobias Fey, who was fundamental to the conclusions of this work. I want to mention my friends at UFAM (Universidade Federal do Amazonas) and LabMat (Laboratório de Materiais), the most supportive people one could find. Additionally, I would like to thank the Multi-User Center for Analysis of Biomedical Phenomena (CMABio) for the SEM imaging. I would like to thank FAPESC (Fundação de Amparo à Pesquisa e Inovação do Estado de Santa Catarina) through grant No 03/2017. This study was financed in part by the Coordenação de Aperfeiçoamento de Pessoal de Nível Superior - Brasil (CAPES) - Finance Code 001. On a more personal note, I would like to thank my family, Léo, Nox, and all the people who in any way helped me get here. Thank you.

So dawn goes down to day.
Nothing gold can stay (Frost, 1923).

ABSTRACT

To understand the role of cerium (Ce = 0, 0.01, and 0.02 mol%) and vanadium-doping (V =0, 0.3, and 0.4 mol%) in the $Ba_{0.85}Ca_{0.15}Ti_{0.9}Zr_{0.1}O_3$ (BCZT) ceramic structure and possible synergetic effects in reducing the sintering temperature of BCZT, a novel straightforward sol-gel synthesis route is proposed. Furthermore, the impacts of cerium and vanadium doping are determined. Structural, microstructural, dielectric, ferroelectric, and piezoelectric analysis is performed to realize this comprehensive feat. In addition, sintering studies help elucidate how these dopants can become tools to improve the processing of BCZT. It is clear from X-ray diffraction measurements and Rietveld analysis that the proposed synthesis method, after calcination at 800 ºC for 5 hours, is successful in yielding crystalline BCZT and V and Ce-doped BCZT samples in the perovskite ferroelectric tetragonal structure (*P4mm*). Sintering at various temperatures, 1250, 1350, and 1450 ºC, does not induce the nucleation of secondary phases or phase transitions. From sintering studies, it is possible to determine that V reduces BCZT's sintering temperature to at least 1250 ºC, facilitating processing. Structural analysis of sintered samples, confirmed by Rietveld refinements, shows that Ce and V occupy the B site in the ABX_3 basic structure, considering the composition range studied. Piezoelectric measurements reveal that all samples underperform, which can be explained by the microstructure developed and observed by scanning electron microscopy (SEM) imaging. However, V can potentially improve dielectric performance compared to undoped BCZT. From the in situ dielectric measurements, Curie temperature (T_C) is increased to 120 ºC, an almost 70% increase compared to undoped BCZT. At the same time, room temperature permittivity values suffer a significant reduction of over 50% when vanadium doping is carried out. Polarization and strain responses show that vanadium is also responsible for increased remanent polarization and a softer ferroelectric behavior than undoped BCZT. Strain response is reduced when Ce and V enter BCZT's lattice, and the degree depends on dopant concentration; however, the reduction can be mild while the sintering temperature is relatively low for V-doped samples. Thus, vanadium doping can be a powerful tool in facilitating the processing of BCZT without compromising piezoelectric performance, allowing for higher thermal stability and an eco-friendly process.

Keywords: sol-gel; BCZT; doping; piezoelectrics.

RESUMO

Para compreender o papel da dopagem por cério (Ce = 0, 0.01, and 0.02 mol%) e vanádio (V =0, 0.3, and 0.4 mol%) na estrutura da cerâmica $Ba_{0.85}Ca_{0.15}Ti_{0.9}Zr_{0.1}O_3$ (BCZT) e possíveis efeitos sinergéticos na redução da sua temperatura de sinterização, uma nova e objetiva rota de síntese é proposta. Adicionalmente, os impactos da dopagem por cério e vanádio são determinados. Para realizar esse feito abrangente, são realizadas análises estruturais, microestruturais, dielétricas, ferroelétricas e piezoelétricas. Além disso, estudos de sinterização ajudam a elucidar como esses dopantes podem se tornar ferramentas para melhorar o processamento do BCZT. Fica claro por medidas de difração de raios-X e análise por Rietveld que o método de síntese proposto, após calcinação à 800 ºC por 5 horas, é bem-sucedido em produzir amostras de BCZT e BCZT dopado por V e Ce cristalino na estrutura perovskita tetragonal ferroelétrica (*P4mm*). Sinterização realizada em várias temperaturas, 1250, 1350, and 1450 ºC, não induzem nucleação de fases secundárias ou transição de fases. Por estudos de sinterização é possível determinar que V reduz a temperatura de sinterização do BCZT para ao menos 1250 ºC, facilitando o processamento. Análise estrutural das amostras sinterizadas, confirmadas por refinamento Rietveld, mostram que Ce e V, considerando o intervalo de composição estudado, ocupam o sítio B na estrutura básica ABX_3. Medidas piezoelétricas revelam que todas as amostras têm desempenho insatisfatório, o que pode ser explicado pela microestrutura desenvolvida e observada pelas imagens de microscopia eletrônica de varredura (MEV). Entretanto, V tem o potencial de melhorar a performance dielétrica quando comparado com BCZT não-dopado. Das análises dielétricas *in situ* é determinado que a temperatura Curie (T_C) é elevada para 120 ºC, um aumento de quase 70% quando comparado com o BCZT puro, enquanto valores de permitividade à temperatura ambiente sofrem grande redução acima de 50% quando a dopagem por vanádio é realizada. Respostas de polarização e deformação mostram que vanádio é também responsável pelo aumento da polarização remanescente e por um comportamento ferroelétrico "macio" em comparação ao BCZT não-dopado. A resposta de deformação é reduzida quando Ce e V entram na rede do BCZT, o grau depende do dopante e concentração, entretanto, a redução pode ser leve enquanto a temperatura de sinterização é consideravelmente baixa para as amostras dopadas por vanádio. Assim, dopagem por vanádio pode ser uma ferramenta poderosa na facilitação do processamento de BCZT sem comprometer de forma relevante a performance piezoelétrica e permitindo maior estabilidade de térmica e um processo mais amigável para o meio ambiente.

Palavras-chave: sol-gel; BCZT; dopagem; piezoelétricos.

RESUMO EXPANDIDO

Introdução

Materiais piezoelétricos são extraordinários, pois podem converter o estresse mecânico em uma resposta elétrica na forma de uma carga elétrica. Inversamente, quando submetidos a um campo elétrico externo, geram uma resposta mecânica correspondente na forma de deformação (Sekhar *et al.*, 2023; Shaukat *et al.*, 2023). Estes são, respectivamente, os efeitos piezoelétricos direto e indireto, e permitem uma multitude de aplicações interessantes, como em capacitores, supercapacitores, sensores autônomos, atuadores, transdutores em aplicações médicas, atuadores em mecanismos de supressão de vibração, microfones subaquáticos e alto-falantes, para citar algumas (Pyun; Kim; Park, 2023; Sezer; Koç, 2021; Shellaiah; Sun, 2020; Song *et al.*, 2022; Tichý *et al.*, 2010; Yamashita *et al.*, 2022). Naturalmente, materiais que apresentam tamanho potencial atraem considerável atenção, e as perovskitas assumem papel de destaque no campo de materiais piezoelétricos (Sezer; Koç, 2021). As perovskitas são materiais com estruturas semelhantes ou derivadas da estrutura básica ABX_3. Nela, A é um cátion maior, B é um cátion menor e X é um ânion (Tilley, 2016). Estes materiais apresentam características estruturais específicas, a não centrossimetria, que dão origem a fenômenos interessantes como ferroeletricidade, piroeletricidade e piezoeletricidade. As perovskitas tornaram-se um assunto de interesse na década de 1940, quando foi descoberto que elas apresentam valores de capacitância excepcionalmente elevados, mesmo na forma policristalina. Estes altos valores ocorrem devido à polarização não linear, característica dos materiais ferroelétricos. Outra característica essencial destes materiais é sua polarização permanente e reversível. Ao estudar as primeiras composições conhecidas destes materiais, como o titanato de bário, várias outras composições foram descobertas, o que permitiu a expansão do campo de aplicação dos ferroelétricos. Esse desenvolvimento fantástico levou a extensas investigações sobre dopagem e ao desenvolvimento de novas composições. Seus altos coeficientes piezoelétricos e dielétricos combinados com alto fator de acoplamento eletromecânico, propriedades especialmente ligadas ao PZT (solução sólida $PbZrO_3$–$PbTiO_3$), os transformaram em incríveis recursos tecnológicos. O PZT é o material piezoelétrico/ferroelétrico mais relevante e o padrão com o qual outros concorrentes são comparados. As propriedades notáveis do PZT se originam de sua MPB (*morphotropic phase boundary*), especialmente da sua inclinação acentuada (Wu, 2020). Na região da MPB, a coexistência de fases ferroelétricas dá origem a propriedades superiores. No entanto, o chumbo não é compatível com as regulamentações cada vez maiores contra o uso de produtos químicos nocivos (Chen *et al.*, 2020; Zimmerman *et al.*, 2020). Naturalmente, pesquisas consideráveis foram realizadas sobre obtenção de composições livres de chumbo. Para suprir essa demanda, vários sistemas têm sido investigados, como BT ($BaTiO_3$), KNN ($K_{0.5}Na_{0.5}NbO_3$), BNT ($Bi_{0.5}Na_{0.5}TiO_3$) e BFO ($BiFeO_3$) (Wu, 2020). Além disso, diferentes estratégias têm sido estudadas para melhorar o desempenho de composições de perovskitas livre de chumbo, como investigação de composições que contêm cátions de maior polarizabilidade, controle microestrutural quanto ao tamanho de grão e domínio ferroelétrico, engenharia de MPB e engenharia de defeitos (Waqar *et al.*, 2022). Novas aplicações no campo de dispositivos geradores MEMs/NEMs (micro e nanoeletromecânicos, respectivamente) e o surgimento da IoT (*Internet of Things*) criaram uma demanda ainda mais significativa por perovskitas sem chumbo de alto desempenho. Para este fim, um dos sistemas investigados é o sistema BCZT, uma solução sólida de titanato de bário com Ca e Zr ocupando os sítios A e B, respectivamente. Os primeiros a investigar este material foram Liu e Ren (Liu; Ren, 2009). Eles determinaram sua composição de PPB (*polymorphic phase boundary*), $Ba_{0.85}Ca_{0.15}Ti_{0.9}Zr_{0.1}O_3$ (BCZT), e estudaram a natureza de suas transições e dinâmica de transição de fase, especialmente no que compete a PPB. Desde então, muitos outros também se aventuraram, investigando sua verdadeira natureza do PPB, dopagem com vários elementos, determinando a estabilidade e a otimização do processamento, por exemplo (Bian; Zhou; Zhang, 2022;

Bijalwan *et al.*, 2019a, 2022; Buatip *et al.*, 2018, 2020; Chen; Chao; Yang, 2019; Coondoo *et al.*, 2018; Fadhlina; Atiqah; Zainuddin, 2022; Hanani *et al.*, 2019; Liu; Cheng; Li, 2019; Sahoo *et al.*, 2021; Wang *et al.*, 2022; You; Guo, 2022). A melhora de desempenho é crucial para o avanço do campo de perovskitas livres de chumbo, mas, além disso, o controle e a otimização do processamento também são uma demanda atual, como exemplificado por um trabalho recente sobre o processamento rápido de BCZT dopado com Ce, controlando parâmetros de sinterização, taxa de aquecimento e seus possíveis impactos nas propriedades gerais (Bijalwan *et al.*, 2022). O processamento, especialmente a sinterização, consomem tempo e energia significativos, e otimizar essa parte da cadeia de produção é extremamente importante. Embora cerâmicas BCZT possam ser obtidas por sinterização à 1300°C, temperaturas mais altas, em torno de 1475°C, são necessárias para atingir uma microestrutura ideal, ou seja, tamanho adequado de grão e tamanho ideal de domínio ferroelétrico, que permita propriedades funcionais ideais. Uma das maneiras pelas quais essa temperatura pode ser reduzida é por meio da dopagem, e a melhor ferramenta para promover a dopagem é por meio de processos químicos, como o método sol-gel, devido à fácil incorporação, dopagem uniforme e controle excepcional do processo (Navas *et al.*, 2021). No entanto, a dopagem em ferroelétricos livres de chumbo permanece pouco compreendida, e muitas das lições de materiais baseados em chumbo não podem ser facilmente transferidas para composições livres de chumbo (Genenko *et al.*, 2015). A dopagem é uma prática recorrente para ajustar o comportamento das perovskitas, uma vez que as perovskitas podem ser muito flexíveis, permitindo substituições aliovalentes e isovalentes nos sítios A e B, o que inclui o sistema BCZT. Especificamente, o processamento pode ser otimizado pela dopagem apropriada. Por exemplo, Ce e V demonstraram reduzir a temperatura de sinterização do BCZT (Bijalwan *et al.*, 2019b; Bijalwan; Tofel, 2019; Bijalwan; Tofel; Holcman, 2018; Hayati *et al.*, 2019; Verma *et al.*, 2021; Yang *et al.*, 2019). No entanto, pouco se sabe sobre a sinergia e os impactos estruturais de ambos os dopantes entrando na rede do BCZT simultaneamente. Além disso, o método de síntese pode desempenhar um papel crucial, que ainda não foi revelado no que diz respeito à co-dopagem de Ce e V do BCZT. Geralmente, a síntese e dopagem do BCZT é realizada por síntese de estado sólido, e os óxidos de Ce e V são adicionados ao pó de BCZT previamente calcinado para serem homogeneizados antes da sinterização. Prática comum para a adição de materiais que facilitam a sinterização. No entanto, para entender verdadeiramente o papel dos próprios elementos dopantes, sem a interferência de quaisquer características que possam surgir da dinâmica de sinterização de uma fase líquida, por exemplo, é necessária uma abordagem diferente. Para isso, o método sol-gel pode ser uma importante ferramenta para entender exclusivamente o papel desses dopantes, considerando a concentração ideal dos dopantes já revelada na literatura cientifica que trata da dopagem de Ce e V do BCZT. Assim, estudos de sinterização de BCZT sintetizado sol-gel por uma nova rota que revela os efeitos da co-dopagem por Ce e V aliados à investigação aprofundada do impacto estrutural de ambos os dopantes e seus efeitos nas propriedades funcionais críticas podem ajudar a determinar sua relevância no processamento do BCZT, o que é proposto nesta tese. Os resultados desta tese foram publicados em parte na revista *materials* (Marques *et al.*, 2024) o que destaca a relevância deste tópico.

Objetivos

Como objetivo principal, deseja-se revelar o potencial da dopagem por vanádio e cério no processamento e na performance da cerâmica piezoelétrica BCZT sintetizada pelo método sol-gel. Para alcançar esse objetivo propõe-se: 1) Desenvolver novas rotas de síntese para realizar a dopagem e co-dopagem da cerâmica BCZT por vanádio e cério, 2) Realizar caracterizações

estruturais e microestruturais extensas das cerâmicas obtidas e 3) Mensurar a performance através de extensas caracterizações ferroelétricas, piezoelétricas e dielétricas.

Metodologia

BCZT puro ($Ba_{0.85}Ca_{0.15}Ti_{0.9}Zr_{0.1}O_3$), BCZT dopado por cério (Ce = 0, 0,01, and 0,02 mol%), BCZT dopado por vanádio (V =0, 0,3, and 0,4 mol%) e BCZT co-dopado por vanádio e cério foram sintetizados pelo método sol-gel. Primeiramente foram produzidas soluções das composições desejadas seguido por envelhecimento de 24 horas e posterior gelificação através do aquecimento gradual até 215 ºC por meio de uma placa aquecedora (WiseStir MSH-200). Posteriormente foi realizada secagem does géis obtidos por 24 horas à 250 ºC, produzindo os correspondentes xerogéis. As amostras foram devidamente cristalizadas após tratamento térmico à 800 ºC por 5 horas adotando taxa de aquecimento de 5 ºC/minuto. Após a obtenção das amostras cristalinas foi realizada a moagem por 96 horas em etanol estabelecendo uma BPR (*ball-to-powder ratio*) de 5:1, usando esferas de zircônia como corpos moedores. Após esta etapa, os pós calcinados moídos foram secos à 90 ºC usando uma chapa aquecedora. Prensagem uniaxial foi adotada para obter corpos verdes para sinterização adotando os seguintes parâmetros: 125 MPa de pressão por 3 minutos. Solução de PVA foi usada como ligante, um molde de aço de 10.2 mm de diâmetro interno foi empregado para obter os corpos verdes. A sinterização foi realizada sem controle de atmosfera, empregando um forno programável (Haraeus). Uma etapa de eliminação de ligante foi estabelecida à 500 ºC, com uma isoterma de uma hora e taxa de aquecimento até esta temperatura de 3 ºC/minuto. Sinterização foi realizada à três temperaturas distintas, 1250, 1350 e 1450 ºC com uma isoterma de 4 horas, adotando taxa de aquecimento de 4 ºC/minuto até a temperatura de sinterização. Após sinterização as amostras tiveram suas superfícies preparadas através de lixamento usando lixa de carbeto de silício seguida por uma etapa de lixamento em uma máquina de lixamento automático Jung (JF415-S) para obter faces em plano paralelo com espessura final de aproximadamente 0.8 mm. Caracterização estrutural foi realizada por difração de raios-X usando um difratômetro Bruker (D8-Advance), radiação de cobre, realizando medidas entre 15 e 90º, adotando tempo por passo de 1 segundo e passo de 0,002º, voltagem de 40 kV e corrente de 25 mA. Os padrões de difração obtidos foram refinados pelo método de Rietveld usando o software GSAS (Toby; Von Dreele, 2013), seguindo as recomendações da IUCr (*International Union of Crystallography*) (McCusker *et al.*, 1999). Para realizar os cálculos necessários para o refinamento, o CIF (*Crystallographic Information file*) número 230567 (Coondoo *et al.*, 2018) do ICSD (*Inorganic Crystal Structure Database)* (Fluck, 1996) foi usado como modelo estrutural e uma amostra padrão de alumina foi utilizada para criar o arquivo contendo a contribuição instrumental para o alargamento dos picos de difração. Polinómios de Chebyschev, sétima ordem, foram utilizados para modelar o background produto do espalhamento inelástico. A microestrutura foi investigada por MEV (Microscopia Eletrônica de Varredura) através de um microscópio JEOL (JSM – IT500HR), usando o software ImageJ (versão 1.54j) para análise das imagens (Schneider; Rasband; Eliceiri, 2012). Densificação foi determinada através da pesagem das amostras antes e depois da sinterização e expressa em termos de perda de massa em função da temperatura de sinterização. Densidade foi medida pelo método de Arquimedes usando uma balança analítica (Mettler Toledo AG204) e água como líquido auxiliar. Para realizar as caracterizações dielétricas, ferroelétricas e piezoelétricas contatos elétricos foram criados com tinta prata (G302-Leitsilber) aplicada em ambas as superfícies e deixando secar naturalmente por 1 hora. Medidas dielétricas *in situ* foram realizadas usando um medidor LCR (Keysight E4980AL) acoplada a um forno (Nabertherm LE 4/11/3216) para obter permissividade elétrica e tangente de perda em função da temperatura, realizando medidas entre 20 e 200 ºC, empregando uma taxa de aquecimento de 2 ºC/minuto e frequências entre 10 Hz e 1 MHz, realizando medidas por década. d_{33} e capacitância foram medidos usando o equipamento

PiezoMeter System PM300 (110 Hz de frequência e 10 N de força) após polarização em óleo (Wacker Silicone Fluid AP 150) à temperatura ambiente por 30 minutos, aplicando 3 kV/mm de campo elétrico. Curvas de polarização e deformação em função do campo elétrico foram obtidas pelo aixACCT (Systems GmbH, Alemanha), usando acoplado o TF analyzer 2000, unidade de porta amostra para cerâmicas em bulk, amplificador TREK 2020C, aplicando 3 kV/mm de campo elétrico e frequências para obtenção das curvas de histerese de 16.6667 and 1.66667 Hz, 3 ciclos e forma de onda triangular.

Resultados e Discussão

Padrões de difração obtidos das amostras calcinadas para todo o range de composição indicou a cristalização das amostras e introdução bem-sucedida dos dopantes Ce e V da rede do BCZT. Adicionalmente, nenhuma fase amorfa pôde ser identificada. Todos os picos de difração puderam ser indexados pelo padrão número 230567 (Coondoo *et al.*, 2018) do ICSD (Fluck, 1996) que apresenta a estrutura tetragonal ferroelétrica (*P4mm*, grupo espacial número 99). O que também foi confirmado por posteriores refinamentos Rietveld dos padrões de difração das amostras calcinadas. Uma fase minoritária de óxido de titânio, 24.3º, foi identificada nas amostras dopadas por cério indexada pelo padrão número 1537224 (Lacks; Gordon, 1993) do ICSD. Medidas de difração de raios-X e refinamento Rietveld revelaram que sinterização, para todas as temperaturas adotadas, não induziram transição de fase, ou, nucleação de fases indesejadas. Também foi confirmado que o ligante, PVA, foi devidamente eliminado durante o processo de sinterização. Adicionalmente, foi possível determinar através do deslocamento dos picos de difração para maiores ângulos que os dopantes ocupam o sítio B, substituindo os átomos de Zr e Ti. Medidas de densificação e de densidade em função da temperatura de sinterização mostraram que o vanádio é responsável por reduzir significativamente a temperatura de sinterização do BCZT em até 200 ºC através da estabilidade dos valores de densificação e de densidade quando a temperatura é aumentada no processamento das amostras dopadas por V. Ce, nas concentrações adotas, tem efeito limitado na temperatura de sinterização. Imagens de MEV confirmaram estas afirmações. Amostradas dopadas por V apresentam média de tamanho de grão maior e desvios padrão significantes, o que indica grão não-uniformes, o que pode ter efeito deletério nas propriedades piezoelétricas destes materiais, enquanto o aumento do tamanho médio de grão tem efeito positivo e explica a melhor performance piezoelétrica destas amostras. Isso acontece devido a maior mobilidade dos domínios ferroelétricos, o que favorece a polarização. Isso é mais explícito quando comparadas com a amostra não dopada que possui grãos mais finos o que prejudica a performance piezoelétrica, mesmo apresentando alta densificação, próximo de 98%. A presença de Ce pôde ser associada com maior porosidade e grãos excessivamente finos, o que explica a performance inferior destas amostras. Em materiais piezoelétricos, poros dificultam o movimento dos domínios ferroelétricos o que tem efeito deletério na performance piezoelétrica. As medidas de coeficiente piezoelétrico em função da temperatura de sinterização confirmam estas afirmações. Todas as amostras apresentaram performance inferior ao que apresentado na literatura científica. O que pode ser explicado pela microestrutura desenvolvida. As amostras dopadas por Ce apresentaram redução do coeficiente piezoelétrico enquanto capacitância se mostrou pouco sensível a adição de Ce. Naturalmente, nas amostras dopadas por Ce e não dopada, o aumento na temperatura de sinterização acarretou uma melhora da performance piezoelétrica. Fenômeno diretamente ligado ao aumento do tamanho médio de grão. Para as amostras dopadas com V, a performance é superior, especialmente, quando a temperatura de sinterização é baixa, 1250 ºC, enquanto a capacitância sofre redução significativa. Nas amostras co-dopadas a melhora de performance também é significativa, o que demonstra que o V é o agente causador. Nas medidas dielétricas *in situ* é possível determinar que o V aumenta significativamente a temperatura Curie do BCZT, aproximadamente 70%, até mesmo para amostras sinterizadas à

1250 ºC. Estas medidas também revelam baixas perdas dielétricas para todas as amostras e que a variação de frequencia tem efeito limitado na permissividade, o que confirma o comportamento ferroelétrico clássico. Curvas de polarização e deformação em função do campo elétrico revelam a grande estabilidade das amostras dopadas de BCZT dopadas com V. As curvas de histerese se sobrepõem para todas as temperaturas de sinterização, mostrando impacto limitado. Todas as curvas apresentam uma descentralização que pode ser associada à defeitos carregados que tem efeito negativo nas propriedades piezoelétricas já que estes defeitos são responsáveis por dificultar o movimento dos domínios ferroelétricos. A deformação das amostras de BCZT dopadas com V apresentam pequena redução, entretanto o ganho relacionado à menor temperatura de sinterização é mais significante. De forma geral, comparando o desempenho das amostras de BCZT dopadas por V com as composições sem chumbo convencionais e com aquela das composições baseadas em chumbo fica claro que as amostras produzidas aqui se encaixam no primeiro grupo. Entretanto, as otimizações da polarização e o refinamento da estrutura em relação ao tamanho de grão e sua uniformidade tem grande potencial quando considerado que a temperatura de sinterização é significativamente reduzida e a estabilidade térmica é favorecida.

Considerações Finais

A rota de síntese proposta foi bem-sucedida na incorporação de cério e vanádio na rede da cerâmica BCZT após calcinação à 800 ºC por 5 horas, como demonstrado pelas análises de DRX e refinamentos Rietveld. Pela metodologia proposta nesta tese é possível obter todas as composições cristalizadas na fase tetragonal ferroelétrica, *P4mm*. Sinterização, em todas as temperaturas adotadas, não induz transição de fases ou nucleação de fases indesejadas. Considerando a ocupação dos dopantes, após sinterização, ambos ocupam o sítio B substituindo átomos de titânio e zircônio. Foi demonstrado que vanádio, em concentrações de 0.3 and 0.4 mol%, tem a capacidade de reduzir a temperatura de sinterização do BCZT em até 200 graus Celsius. Embora a dopagem por V tenha efeitos limitados nas propriedades piezoelétricas do BCZT, a temperatura Curie sofre um aumento significativo de quase 70%, chegando a valores próximos à 120 ºC. Em contrapartida, valores de permissividade dielétrica à temperatura ambiente sofrem uma redução considerável, superior a 50%, quando a dopagem por vanádio é realizada. Através das caracterizações dielétricas *in situ* foi possível determinar que a dopagem por vanádio confere maior estabilidade térmica ao BCZT. Curvas de polarização e deformação em função do campo elétrico levantadas para duas frequências distintas confirmaram que todas as amostras exibem comportamento ferroelétrico clássico. O deslocamento das curvas de polarização indica a presença defeitos, incluindo a composição não-dopada. Ocorre uma redução na resposta de deformação quando vanádio está presente no BCZT, entretanto a redução é limitada enquanto a redução na temperatura de sinterização é considerável. A polarização remanescente pode ser melhorada, como foi visto em amostras dopadas com vanádio, de 16 para até 24 $\mu C/cm^2$. Dessa forma, foi determinado que vanádio pode ser uma ferramenta poderosa no processamento do BCZT, reduzindo a energia necessária para o seu processamento e tendo efeito positivo significativo principalmente envolvendo a estabilidade térmica.

Palavras-chave: sol-gel; BCZT; dopagem; piezoelétricos.

LIST OF FIGURES

LIST OF TABLES

TABLE OF CONTENTS

1 INTRODUCTION

Piezoelectric materials are remarkable as they can convert mechanical stress into an electrical response in the form of an electrical charge. Conversely, when subjected to an external electrical field, they generate a correspondent mechanical output, a strain (Sekhar *et al.*, 2023; Shaukat *et al.*, 2023). These are respectively the direct and converse piezoelectric effects, and enable a multitude of exciting applications such as capacitors, supercapacitors, self-powering sensors, actuators, transducers in medical applications, actuators in vibration suppression mechanisms, underwater microphones, and speakers, to cite a few (Pyun; Kim; Park, 2023; Sezer; Koç, 2021; Shellaiah; Sun, 2020; Song *et al.*, 2022; Tichý *et al.*, 2010; Yamashita *et al.*, 2022). All of these applications are possible due to specific structural features.

Naturally, materials that present this much potential attract considerable research, and perovskites take the lead (Sezer; Koç, 2021). Perovskites consist of materials with similar or derivate structures from the ABX_3 basic structure. A is a larger cation, B is a smaller cation, and X is an anion (Tilley, 2016). They present specific structural features, i.e., noncentrosymmetry, that give rise to interesting phenomena such as ferroelectricity, pyroelectricity, and piezoelectricity.

Perovskites became a subject of interest in the 1940s when it was discovered that they presented unusually high capacitance values through polarization, even in the polycrystalline form. These high values occur due to non-linear polarization, characteristic of ferroelectric materials. Another essential characteristic is their permanent and reversible polarization. In studying earlier materials such as barium titanate, various compositions were discovered, which allowed the expansion of ferroelectrics' field of application. This fantastic development prompted extensive investigations regarding doping and the development of new compositions. Their high piezoelectric and dielectric coefficients combined with high electromechanical coupling factor, properties especially linked to PZT ($PbZrO_3$–$PbTiO_3$ solid solution), transformed them into incredible technological assets.

PZT is the paramount piezoelectric/ferroelectric material and the standard to which other contenders must be compared. PZT's remarkable properties originate in its MPB (*morphotropic phase boundary*), especially its steepness (Wu, 2020). In the MPB region, a coexistence of ferroelectric phases gives rise to superior properties. However, lead is not compatible with the ever-increasing regulations against the use of harmful chemicals (Chen *et*

al., 2020; Zimmerman *et al.*, 2020). Naturally, considerable research has been conducted on lead-free options for PZT. To supply this demand, various systems have been investigated, such as BT ($BaTiO_3$), KNN ($K_{0.5}Na_{0.5}NbO_3$), BNT ($Bi_{0.5}Na_{0.5}TiO_3$), and BFO ($BiFeO_3$) (Wu, 2020). Additionally, different strategies have been studied to improve the performance of lead-free composition, such as investigation of compositions that contain cations of higher polarizability, microstructural control regarding grain and domain size, MPB engineering, and defects engineering (Waqar *et al.*, 2022). New applications in the field of MEMs/NEMs (micro and nanoelectromechanical, respectively) generator devices and the rise of the IoT (Internet of Things) have created an even more significant demand for high-performance lead-free perovskites.

For this purpose, one of the systems investigated is the BCZT system, a solid solution of barium titanate with Ca and Zr occupying the A and B sites, respectively. The first ones to investigate this material were Liu and Ren (Liu; Ren, 2009). They determined its PPB (polymorphic phase boundary) composition, $Ba_{0.85}Ca_{0.15}Ti_{0.9}Zr_{0.1}O_3$ (BCZT), and studied the nature of its transitions and phase dynamics, especially revolving around the PPB. Since then, many others have ventured as well, investigating its PPB true nature, doping with various elements, determining stability, and processing optimization, for example (Bian; Zhou; Zhang, 2022; Bijalwan *et al.*, 2019a, 2022; Buatip *et al.*, 2018, 2020; Chen; Chao; Yang, 2019; Coondoo *et al.*, 2018; Fadhlina; Atiqah; Zainuddin, 2022; Hanani *et al.*, 2019; Liu; Cheng; Li, 2019; Sahoo *et al.*, 2021; Wang *et al.*, 2022; You; Guo, 2022).

Improved performance is crucial to the rise of lead-free perovskites, but in addition to it, processing control and optimization are also a current demand, as exemplified by a recent work regarding the rapid processing of Ce-doped BCZT controlling sintering parameters, heating rate, and the possible impacts on overall properties (Bijalwan *et al.*, 2022). Processing, especially sintering, takes significant time and energy, and optimizing this part of the production chain is incredibly important. Although dense BCZT ceramics can be obtained by sintering at 1300°C, higher temperatures, around 1475°C, are necessary to achieve an ideal microstructure, i.e., adequate grain and ferroelectric domain size, that allows optimal functional properties. One of the ways this temperature can be reduced is through doping, and the best tool to promote doping is through chemical processes, such as the sol-gel method, due to easy incorporation, uniform doping, and exceptional process control (Navas *et al.*, 2021). However, doping in lead-free ferroelectrics remains poorly understood, and many of the lessons from lead-containing materials cannot be easily transferred to lead-free compositions (Genenko *et*

al., 2015). Doping is a recurrent practice to adjust perovskites' behavior since perovskites can be very flexible, allowing aliovalent and isovalent substitutions in the A and B sites, which includes the BCZT system. Specifically, the processing can be optimized by the appropriate doping. For example, Ce and V were shown to reduce BCZT's sintering temperature (Bijalwan *et al.*, 2019b; Bijalwan; Tofel, 2019; Bijalwan; Tofel; Holcman, 2018; Hayati *et al.*, 2019; Verma *et al.*, 2021; Yang *et al.*, 2019). However, little is known about the synergy and structural impacts of both dopants entering the lattice of BCZT simultaneously. Additionally, the synthesis method can play a crucial role, which is yet to be unveiled as far as Ce and V co-doping of BCZT is concerned. Usually, the synthesis and doping of BCZT is performed by solid-state synthesis, and Ce and V oxides are added to calcinated BCZT powder to be homogenized before sintering. Practice that is common for the addition of sintering aids. However, to truly understand the role of the doping elements themselves, without the interference of any features that may arise from the sintering dynamics from a liquid phase, for example, a different approach is necessary. For this, the sol-gel method can be an important tool for understanding exclusively the role of these dopants, considering the optimum concentration range for the dopants already gathered from previous works dealing with the Ce and V doping of BCZT. Thus, sintering studies of sol-gel synthesized BCZT by a novel route gauging the effects of co-doping by Ce and V allied to the in-depth investigation of the structural impact of both dopants and their effects on critical functional properties can help determine their placement in the processing of BCZT, which is proposed in this thesis. The findings of this thesis have been published in part in the *materials* journal (Marques *et al.*, 2024) which highlights the relevance of this topic. As the main objective, we aim to reveal the potential of V and Ce-doping in the processing and performance of sol-gel synthesized BCZT ceramic. To achieve this goal, we set to i) develop novel synthesis routes for the doping and co-doping of BCZT with V and Ce ii) perform extensive structural and microstructural characterizations and iii) gauge performance through in-depth ferroelectric, piezoelectric, and dielectric measurements.

2 BIBLIOGRAPHIC REVIEW

This bibliographic review addresses topics related to the synthesis method adopted in this research, the sol-gel method. The sol-gel method was carried out to produce the desired $Ba_{0.85}Ca_{0.15}Ti_{0.9}Zr_{0.1}O_3$ (BCZT), Ce-doped, V-doped, and V and Ce co-doped BCZT samples. So, the synthesis process performed is elucidated regarding important process parameters, general structures obtained, drying processes, and products. To understand the structure of BCZT, a chapter of this thesis was dedicated to perovskites, a class in which BCZT is inserted. Naturally, all relevant data on BCZT, considering its structure and properties, and especially how BCZT can be tailored by doping, regarding properties and processing, focusing on vanadium and cerium doping, is shown. As it is necessary to understand the overall behavior of BCZT, important topics such as dielectrics, ferroelectricity, and piezoelectricity are addressed. Phenomena that make them such important assets. With this review, we hope to shed light on why we set out to investigate this material and the potential in the process we put forward.

2.1 THE SOL-GEL METHOD

Although the sol-gel method in its beginning, more than a century ago, was restricted to academic research purposes, decades later, it has established itself as a powerful tool for the synthesis of organic and hybrid materials. It allows a high control of composition, structure, and microstructure (Nabavi *et al.*, 1990). Key discoveries in drying and synthesis control measures and techniques paved the progress for this synthesis method and made it more popular than ever (Danks; Hall; Schnepp, 2016).

Succinctly, the sol-gel process can be understood as the gelation of a sol. Whereas the sol is a colloidal suspension in a liquid, a gel is a solid, tridimensional, and continuous network that provides elasticity to the semisolid, confining and supporting a liquid phase that is also continuous. Both constitute a semisolid of colloidal dimensions (Brinker; Scherer, 1990). A colloidal suspension is formed by solid particles dispersed in a liquid phase. Particles that are so small, on the nanometric scale, that they exhibit Brownian movement and are virtually not subjected to gravitational forces. The dispersed particles can be crystalline or amorphous, alternatively, polymeric, systems in which no dense particles of oxides are bigger than 1 nanometer (Brinker; Scherer, 1990; Danks; Hall; Schnepp, 2016).

Gel formation is based on different interactions: covalent bonds, Van der Waals interactions, hydrogen bonds, and chain entanglement. Different types of bonds grant different degrees of stability. Rapid evaporation of solvents can also result in gelation, a common practice in the case of film fabrication. Covalent bonds are stronger and give rise to more stable gels, while gels formed through Van der Waals interactions are destabilized by mere agitation (Brinker; Scherer, 1990).

The process of microstructure formation passes through the dynamics of solubilization and condensation. The formation of more rounded structures or more fractal ones relies heavily on the solid phase solubility or, more precisely, its existence. When it does, species in positive curvatures can be solubilized and condensate again in regions of negative curvature. The solubility for non-aqueous systems is limited, and because of that, there is a tendency to give rise to fractal microstructures. In gelation, the solid phases produced tend to aggregate and finally form a continuous structure, creating a gel (Brinker; Scherer, 1990).

A more detailed description must start by discussing the precursors used in the process. The precursors for the sol-gel process might be salts or organic compounds, like the alkoxides, in aqueous and non-aqueous solvents, respectively.

Alkoxides present the general formula $M(OR)_Z$. In this instance, M is the valence or oxidation number of the metal and is equal to z. OR is the alkoxide group and has the general formula $R = C_nH_{n+1}$. Alkoxides react promptly with water, which is favorable for hydrolysis reactions. The reactivity of the alkoxides depends essentially on the force of the nucleophiles and the electropositivity of the metals (Livage; Sanchez, 1992). Alkoxides may present excessive reactivity, in this case, it must be limited to prevent precipitation instead of the formation of a uniform gel when such a product is desired (Nabavi *et al.*, 1990). The reactivity control of precursors can be performed by alcohol exchange reactions, nucleophilic addition, or substitution. These chemical modifications alter the precursors and their hydrolyzation and condensation behavior (Levy; Zayat, 2015; Nabavi *et al.*, 1990).

The sol-gel synthesis can be divided into two basic steps: hydrolysis and condensation. Solvation occurs when dealing with salts in an aqueous medium. Depending on the pH and valence of the metallic element, there may be present aquo, hydroxo, oxo groups, or a combination of these groups, as seen in Figure 1 (Brinker; Scherer, 1990; Levy; Zayat, 2015). For condensation to occur, hydroxo groups must be present in the coordination of the metallic atom. For that to happen, pH can be adjusted by acid or base addition (Brinker; Scherer, 1990).

Figure 1 – Ligands as a function of pH and oxidation number

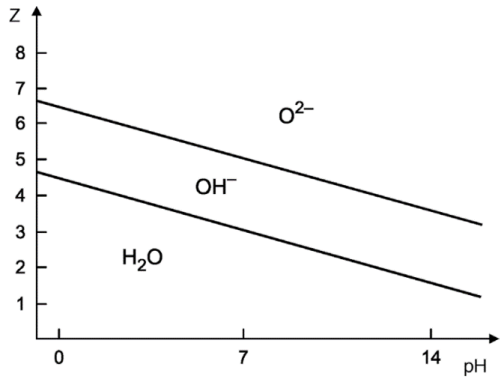

Source: (Levy; Zayat, 2015).

In hydrolysis, OH groups replace the OR groups in nucleophilic reactions. Condensation consists of the reaction between M – OH molecules with themselves and with M – OR molecules to create M – O – M bridges.

Condensation produces molecules of small molecular weight, like alcohol or water molecules, by two types of reaction: nucleophilic addition or nucleophilic substitution. These reactions happen by mechanisms where a nucleophile attacks the molecule that contains the metal and has a positive partial charge, and a group that contains the greater positive charge then leaves the molecule. Nucleophilic addition is exclusive to metals that have their preferred coordination not met, called unsaturation. This happens because the preferred coordination, N, in the transition metals exceeds the valence, z. Thus, coordination can be expanded under certain conditions.

Salts, on the other hand, when in aqueous conditions, can condensate by olation or oxolation depending on the coordination saturation of the metallic atom (Brinker; Scherer, 1990; Levy; Zayat, 2015). Olation consists of the formation of hydroxo bridges between the

metallic centers, water as the positive partial charge leaves the molecule, following the reaction (1) between aquo and hydroxo ligands (Brinker; Scherer, 1990).

$$M - OH + M - OH_2 \longrightarrow M - OH - M + H_2O \quad (1)$$

Via oxolation, oxo bridges are formed by the nucleophilic addition of metal's oxo ligands that have unsaturated coordination. Oxolation may also happen by nucleophilic substitution between oxo and hydroxo ligands followed by nucleophilic addition, and water molecules are released (Brinker; Scherer, 1990).

In hydrolysis, the OR groups present in alkoxides are substituted by OH groups, as in reaction (2).

$$\equiv M - OR + H_2O \longrightarrow \equiv M - OH + ROH \quad (2)$$

Condensation can also happen by alcoxolation, reaction (3), and oxolation, reaction (4), for species that contain metals with unsaturated coordination. The preference for a specific condensation route depends on the electropositivity of the metals, preferred coordination, and H_2O/M ratio (Brinker; Scherer, 1990; Charleux; Copéret; Lacôte, 2014).

$$\equiv M - OH + \equiv M - OR \longrightarrow \equiv M - O - M \equiv + ROH \quad (3)$$

$$\equiv M - OH + \equiv M - OH \longrightarrow \equiv M - O - M \equiv + H_2O \quad (4)$$

As an example, the behavior of a $Ti(OR)_4$ precursor is discussed. The OR group represents an alkoxide as in the precursor $Ti[OCH(CH_3)_2]_4$, titanium isopropoxide. Due to the size of the ligands coordinating the titanium atom, titanium isopropoxide does not tend to oligomerize, remains as a tetracoordinated monomer, and reacts promptly with water. Therefore, the formation of a stable gel would be nearly impossible. However, alterations in this precursor can be such that they change the hydrolysis and condensation dynamics and work to stabilize suspensions (Levy; Zayat, 2015). An approach to control the reactivity of these precursors is the addition of alcohol to promote nucleophilic substitution as follows in reaction (5) or nucleophilic addition for a metal of unsaturated coordination (Brinker; Scherer, 1990).

$$Ti(OR)_4 + xR'OH \longrightarrow Ti(OR)_{4-x}(OR')_x + xROH \quad (5)$$

This exchange depends on the size of the alkoxide group. The bigger it is, the more difficult it is for its substitution. This exchange does happen in ambient conditions. The order in which hydrolysis happens depends on the partial charge of the groups involved; groups with bigger positive partial charges leave the molecule faster, and usually, the modified ligands leave the molecule later in the condensation reactions (Charleux; Copéret; Lacôte, 2014).

Another form to control the formation of precipitates is the utilization of condensation inhibitors, complex ligands that coordinate the metallic atom, like inorganic acids. Again, titanium isopropoxide is used as an example.

The addition of acetic acid expands the coordination of the Ti atom in this molecule from 4 to 6 (Brinker; Scherer, 1990). The acid is consumed, alcohol is formed as a byproduct, and the OPr^i are removed swifter than the acetate groups (Charleux; Copéret; Lacôte, 2014). The usual pathway for condensation of titanium alkoxide precursors involves the nucleophilic attack of oxygen present on the nucleophile, proton transfer from the water molecule to the titanium ligand, and, at last, the release of an ROH group. Coordination expansion of the metallic atom can occur by nucleophilic addition and olation between partially hydrolyzed precursors. Hydroxyl groups create bridges that coordinate metallic atoms. In this process, ROH groups are removed. Nucleophilic substitution reactions follow, as do possibly hydrolysis reactions, which depend on the H_2O/M ratio, and lastly, oxolation and alcoxolation reactions occur where OR and OH groups are released and give place to oxo bridges between metallic centers releasing ROH or H_2O groups, reactions (3) and (4) respectively (Charleux; Copéret; Lacôte, 2014; Nabavi *et al.*, 1990).

If successful, condensation leads to gelation, which happens as a culmination of the solid phase formation. Visually, this point is relatively easy to determine. The once-liquid phase becomes firmer as it gains mechanical resistance. This happens because the fractals that are formed tend to aggregate, forming clusters that also join/bond, creating a network. This turning point is called the percolation threshold. The time needed to achieve gelation varies depending on the precursor and other processing parameters. This process can take hours or minutes (Aegerter; Mennig, 2004).

Once gelation is achieved there are different forms to dry the monoliths, a gel of millimetric dimension (Brinker; Scherer, 1990). The drying process has a considerable impact on the product obtained. Drying in ambient conditions, room temperature, and pressure without controlling the solvent evaporation produces a xerogel. By this method, the wet gel suffers a significant retraction due to capillary forces that exert pressure in the pores, which collapses them, reducing the gel volume by five to ten times the initial one (Brinker; Scherer, 1990). This happens because the liquid/vapor interface is generated when the liquid on the gel transits from the first to the second state, giving rise to capillary forces (Brinker; Scherer, 1990).

Another method for drying a gel is the supercritical drying. In this process, extraordinary drying conditions are created that allow the liquid in the gel to reach the supercritical state. In this state, the liquid behavior can be seen as a liquid that resembles a gas concerning the velocity of the particles and one of a gas that resembles a liquid regarding packing. This translates into the absence of surface tension of the liquid when it's drained from the gel as a gas when the pressure is reduced gradually inside the chamber in an isotherm (Brinker; Scherer, 1990). In supercritical drying, the pore structure is mainly maintained, and the product presents exceptionally low density, keeping its form from before the drying process, the monolith's shape, in what is called an aerogel. CO_2 can be used in supercritical drying when solvent exchange takes place, which can be a slow process but has the advantage of processing at lower temperatures, closer to ambient conditions, which is safer (Klein; Aparicio; Jitianu, 2018).

Gels can also be dried in ambient conditions with subsequent solvent exchange of decreasing surface tension. This solvent exchange allows the permanence of most of the pores, and the gels' retraction is reduced compared to the xerogel. The product of this drying process is the ambigel, like the SiO_2 ambigels (Bay De S. *et al.*, 2017).

Another option is freezing and sublimating the solvent, forming a cryogel (Izadi *et al.*, 2023). All these products have high porosity and specific surface area in different degrees. In Figure 2 a) it can be seen a $BaTiO_3$ gel and b) the aerogel formed after supercritical drying.

Figure 2 – $BaTiO_3$ gel and aerogel

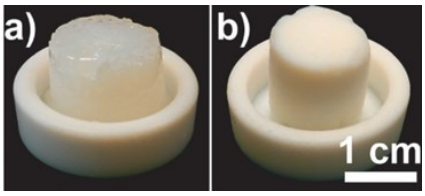

Source: (Rechberger *et al.*, 2014)

Caption: a) Barium titanate gel and b) Barium titanate aerogel.

These different drying processes give rise to different products, aerogels, cryogels, ambigels, and xerogels, that present decreasing degrees of surface area and are generally amorphous solids.

In the processing of perovskites, the sol-gel method can be an important tool mainly due to the synthesis control allowed by the technique, which is a great advantage compared to more traditional synthesis methods, such as solid-state synthesis. The sol-gel method has many advantages and permits the production of a multitude of materials, such as films, thin films, composites, coatings, fibers, and spheres, for example. It's an excellent process to discover new compositions and improved properties. High purity and high homogeneity are easier to achieve as well. Usually, it also requires less energy since the reactions take place at temperatures lower than 220 ºC. It allows complete control of morphology and particle size. As the beginning point is a solution, the reaction steps permit the introduction of doping elements quantitatively and homogeneously. Of course, there are disadvantages, such as the sensibility to moisture, especially due to the alkoxide precursors, the difficulty in scaling up, and the fact that processes can have multiple, time-consuming steps. There is a change in volume during the process, which can be cumbersome during a scaled-up process (Navas *et al.*, 2021). Another disadvantage is that although the number of parameters grants tailorability, it also adds to the complexity of the process.

The process overall is very flexible due to the various parameters that can be optimized to obtain extremely tailored structures and microstructures. Another interesting advantage is the reduction of crystallization temperature, which reduces energy and time consumption when calcination can be performed at lower temperatures (Wang *et al.*, 2016).

Usually, the gels produced by the sol-gel method are amorphous and continue to be so after either supercritical or natural drying, i.e., aerogels or xerogels. However, crystallinity is

mandatory for ferroelectricity (Kao, 2004). This means that heat treatments must be performed to achieve it, which is seen in published papers regarding the sol-gel synthesis of bulk perovskites by this method (Coondoo *et al.*, 2018; Navas *et al.*, 2021). Of course, there has been some research on the topic of crystalline gels, specifically PZT compositions (Löbmann *et al.*, 1998, 1999; Löbmann; Glaubitt; Geis, 2000), but in the majority of cases, the product of the sol-gel method is an amorphous gel.

2.2 DIELECTRICS AND FERROELECTRICS

Dielectrics are better known for being insulants but additionally present a plethora of important phenomena that include relaxation, electric polarization, energy storage, and dissipation, which are incredibly important to describe ferroelectricity and piezoelectricity (Kao, 2004). In dielectrics, the bandgap between the conduction and the valence band is bigger than a few electron volts, which sets them apart from semiconductors; the latter, with the increase of thermal agitation, presents the transition of electrons from the valence to the conduction band. Additionally, ideal dielectrics do not possess charge carriers, although they do exist and originate from electric contacts.

Ferroelectric and piezoelectric materials are dielectrics, and to understand their behavior, some topics on electromagnetism must be discussed, which is done herein.

Maxwell amalgamated electromagnetism into four equations. From these equations, important constants can be obtained: magnetic permeability, μ, electric permittivity, ε, and electric conductivity, σ (Kao, 2004). Through these constants, it is possible to characterize materials' response concerning electromagnetic fields, which is described by equations (1), (2), and (3) where E is the electric field, D is the electric displacement, H is the magnetic field, B is the magnetic induction and J is a vector denoting the electric current density.

$$B = \mu H \quad (1)$$

$$D = \varepsilon E \quad (2)$$

$$J = \sigma E \quad (3)$$

Faraday and Cavendish were the first to observe that capacitance depends solely on the insulant material between the plates of a capacitor, independently of its geometry (H. M. Nussenzveig, 2022). The material is a dielectric, and the property that rules its behavior is the relative permittivity, ε_r, also known as the dielectric constant. The relative permittivity is a dimensionless constant that characterizes the response of a material to an applied electric field, described by equation (4), whereas ε_r is the relative permittivity, and ε_o is the permittivity in a vacuum. ε_r expresses how much the permittivity of the material exceeds the one of the vacuum (Kao, 2004).

$$\varepsilon_r = \frac{\varepsilon}{\varepsilon_o} \tag{4}$$

The dielectric constant, albeit its name, strongly depends on the frequency of the applied electric field. This happens because of the time-dependent polarization phenomena due to the different mechanisms by which they manifest. This means there are different response times in reaction to the applied electric field, i.e., a delay in following the electric field variation (Kao, 2004). Faster mechanisms promptly manifest and more easily follow the externally applied electric field. Usually, the dielectric constant is measured in frequencies that are considered low, 1 MHz if not stated differently, and vary with the structure presented, if the material is piezoelectric when it is not polarized, if relaxation effects are present for higher frequencies, and if the material is above its transition temperature to the paraelectric state (Cardarelli, 2018; Fleisch, 2008; Kao, 2004). Pressure, composition, temperature, and defect configuration are other parameters that interfere with the dielectric constant (Kao, 2004). Ferroelectrics present as one of the most poignant characteristic values of permittivity way greater than most dielectrics, and that is why they have first become subjects of interest. Permittivity stays under 100 for simple dielectrics, while ferroelectrics can reach 10^5 (Kao, 2004). This has everything to do with polarization, which is discussed herein.

Polarization occurs when an insulant is in the presence of an electric field. Polarization consists of the relative position change in charges, redistribution of charges, induction of dipoles, or orientation of existing ones. Polarization can occur through different mechanisms. The one associated with permanent dipoles is called spontaneous and is a slower process than one of the ions. This fact makes the polarization process frequency-dependent (Cardarelli, 2018; Fleisch, 2008; Kao, 2004). When polarization occurs, positive charges follow the direction of

the electric field, and the negative ones in the opposite direction, this phenomenon creates its own electric field. The charges in the contacts of the capacitors do the same, and this field opposes the external electric field, reducing the internal electric field (Bain; Chand, 2017; Fleisch, 2008). This reduction causes an increase in capacitance; thus, the voltage is reduced by a $1/\varepsilon_r$ factor, because it depends on the electric field, it is also reduced by the same factor and has a discontinuity due to the presence of the dielectric, and a reduction of potential energy because of it (H. M. Nussenzveig, 2022).

Polarization can be characterized by the constant α (polarizability). It expresses how easily the electric field polarizes a material, described in equation (5), q is the charge, and δ is the distance between charges. Polarizability is a proportionality constant between the local electric field ($\overrightarrow{E_{loc}}$) and the average values of the dipole moment ($\langle\vec{u}\rangle$), shown in equation (5), in which it is considered that the vectors have the same direction, although this is not often the case for most materials that possess permanent dipoles (Kao, 2004).

$$\langle\vec{u}\rangle = \langle q\delta\rangle = \alpha\overrightarrow{E_{loc}} \quad (5)$$

The dielectric constant, polarizability, and electric susceptibility (χ), the electric counterpart of magnetic susceptibility, are linked by equations (6) and (7). Whereas N is the number of dipoles, α is the polarizability, P is the polarization, and D_o is the electric flux density for the free charge (H. M. Nussenzveig, 2022). Thus, it is possible to correlate a measurable quantity, the dielectric constant, to the polarization of a dielectric material and characterize it.

$$\varepsilon_r = 1 + \frac{N\alpha}{\varepsilon_o} = 1 + \chi \quad (6)$$

$$\chi = \varepsilon_r - 1 = \frac{P}{D_o} \quad (7)$$

Polarization faces intrinsic inertia to the movement necessary for it to occur, being the displacement of ions, clouds, and permanent or induced dipoles. This loss is called dielectric loss and is generally expressed as a loss tangent, the energy consumed to counter the inertia inherent to the material (Cardarelli, 2018; Kao, 2004). Loss tangent is important for dielectric materials because it is a limiting factor for application. Bigger dielectric losses are related to a bigger relative permittivity, and the opposite also occurs (Cardarelli, 2018).

Ferroelectric materials present spontaneous and reversible polarization in a specific temperature range. In ferroelectric materials, the symmetry center for the negative charges does not coincide with the center of the positive ones; ions in the unit cell can be viewed as charges, and their position within the cell creates permanent dipoles associated with the unit cell structure. For this to occur, these materials must be crystalline, and their structures must be noncentrosymmetric (Cardarelli, 2018; Kao, 2004).

The permanent dipoles present in ferroelectric materials align themselves in parallel in the direction of the crystalline axis, called the polar axis, which forms ferroelectric domains similar to the Weiss domains for ferromagnetic materials (Bain; Chand, 2017; Cardarelli, 2018; Tichý *et al.*, 2010). When these domains reach a critical size in a ferroelectric material, forming domains with different orientations is energetically favorable. The walls that separate these domains also have energy associated with them. The domain formation reduces the energy of the system by reducing the electrostatic energy formed due to the decrease in the depolarizing field, and this process limits itself because the walls themselves store energy (Kao, 2004). The energetic balance between the energy of the walls and one of the domains themselves rules the mechanism of ferroelectric domain formation. Otherwise, this energy would be exceedingly large, making the system unstable (Kao, 2004). A domain has a liquid polarization, which is called spontaneous. However, the orientations of all the domains present in the material are randomized, so their sum is zero, and, in its entirety, the material does not present polarization. Single crystals, through polarization, can present one large domain. Polycrystalline material, however, cannot. This occurs because the crystallite axes are randomly arranged in polycrystalline materials, and the electric field cannot reorient them.

Domain configuration is incredibly important, especially domain size. Optimum domain size permits easy motion of domains when being polarized which results in improved piezoelectric performance. The optimum domain size depends on composition. If the domains are too small, piezoelectric is curbed configuring the scale effect. If the domains are excessively small, the size effect takes place, and ferroelectricity is extinguished (Ihlefeld *et al.*, 2016).

Additionally, depending on the structure, ferroelectrics can either be multiaxial or uniaxial, depending on relative domain orientation. Uniaxial domains can only present two dipole directions opposite to an adjacent domain, forming a 180^{o} wall. In multiaxial ferroelectric, there are more possibilities of arrangements of domains and non-180^{o} are possible.

For example, barium titanate (in the tetragonal phase) has six polarization directions, and walls can be formed at right angles (Kao, 2004).

In ferroelectrics, the redirection of polarization vectors formed by the domains in response to the incident electric field is called polarization reversibility (Tichý *et al.*, 2010). The ferroelectric domains interact with each other and are responsible for structure deformation. This leads to an aging phenomenon, whereas the relaxation of this tension causes the reduction of the dielectric constant, which is also dependent on the applied voltage and fabrication history (Cardarelli, 2018).

The electric field applied in these materials causes the growth of favorable domains, increasing the polarization and dielectric susceptibility. The polarization vectors are oriented in the direction of the applied electric field, which results in liquid polarization. Ferroelectric polarization is way superior to the polarization of common dielectrics (Cardarelli, 2018). Ferroelectric materials present a non-linear relation between polarization and the applied electric field, resulting in a hysteresis loop, which appears because of the domain configuration due to the energy demanded to move them and leads to the creation of a remanent polarization when the electric field is suspended. The spontaneous polarization that ferroelectrics possess eclipses the remaining types of polarization (Cardarelli, 2018). Temperature influences polarization, and its effects can be observed in the hysteresis loop. Higher temperatures allow the domains more mobility for their reorientation and the electric field necessary to do so is smaller up to the Curie temperature (T_C). At temperatures higher than the T_C, the material begins to present paraelectric behavior and the linear relation between polarization and the electric field is observed. The transition between the ferroelectric and the paraelectric state at the T_C is marked for the ferroelectrics by a progressive increase of the dielectric constant up to the end of the transition. This atypical value for the dielectric constant is also followed by anomalous polarization and piezoelectric behavior due to the instability region linked to the phase transition. The Curie temperature is a few degrees below the transition temperature for the tetragonal to cubic symmetries (Kao, 2004; Tichý *et al.*, 2010).

The transition to the paraelectric state can be a first-order or a second-order transition, the latter continuous, the first discontinuous. There is a change in entropy and latent heat for a first-order transition, but this does not occur for the second-order transition. Nearing the T_C, dielectric permittivity values are unusually high. However, at temperatures superior to the Tc,

i.e., in the paraelectric state, ε_r decreases following the Currie-Weiss relation, seen in equation 8, where C is the Curie constant, and T is the temperature (Kao, 2004).

$$\varepsilon_r = \frac{C}{T - T_C} \quad (8)$$

The relation between polarization and the electric field can usually be obtained by a Sawyer-Tower circuit, in its simpler form, consisting of a capacitor constructed from the sample that must be studied, a standard capacitor, an AC source, and an oscilloscope at frequencies up to 60 Hz (Kao, 2004). The electric field intensity is usually expressed in kV per mm, and its magnitude is a few kV/mm. Usually, measurements are not performed over breakdown since it destroys the sample. However, it can be an interesting option when it is necessary to investigate the behavior right before the breakdown occurs. Alterations to the circuit and compensation mechanisms can be made; however, the compensation method is rarely described. In this case, the circuit is called a modified Sawyer-Tower circuit (Cain, 2014). By this method, it is possible to obtain a hysteresis loop like the one in Figure 3. This, of course, is not the only way to get the P-E loop; automated systems have been created for this purpose. Usually, they operate based on an internal compensating system like the TF analyzers from AixACCT Systems GmbH, Germany. This system, and others like this, demand less work since the entire set-up is already ready to perform the desired measurements, leaving the operator to determine measurement parameters, place the sample, and determine its relative position with the help of an interferometer. During this measurement, the sample is kept immersed in oil, usually silicon, similar to what is done during the polarization process.

Figure 3 – Ferroelectric hysteresis loop

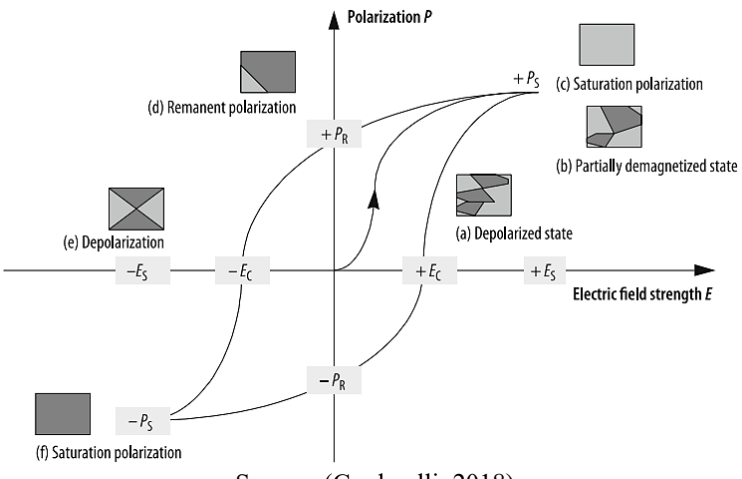

Source: (Cardarelli, 2018)

When a ferroelectric material is subjected to a P-E measurement, initially, without the presence of the electric field, it does not present liquid polarization, as seen in Figure 3 state a). In the presence of an electric field, the ferroelectric domains favorably aligned grow in favor of the non-aligned ones up to saturation, as seen in c). Initially, the path to the saturation point is almost linear because the electric field is not strong enough to orient the domains. Once it is, the polarization maintains a non-linear path until most of the ferroelectric domains are oriented by the electric field applied. Once the electric field is suspended, the material presents a remanent polarization, smaller than spontaneous polarization, because some domains can return to their initial positions due to their metastable configuration. An opposite electric field called the coercive field (Ec) must be applied to remove this polarization. With this new alignment, there is no polarization, e), and the magnitude of this field depends on temperature, frequency, and electric field waveform. This value is also called coercivity. Continuing the cycle, with the increase of the electric field, polarization reaches saturation, f), and finally, in removing the electric field again, there is a remanent polarization. The term reversible polarization implies the possibility of obtaining a polarization with an inverse orientation by applying an electric field in the opposite direction. It is an effect of the domain configuration.

The initial state of the ferroelectric can only be established again if heated above the Curie temperature and cooled. By doing so, the domains will be randomly oriented again. The area of the loop in the P-E graph, polarization as a function of the electric field, corresponds to the energy dissipated and demonstrates the irreversibility of the process (Cardarelli, 2018).

2.3 PIEZOELECTRICITY

Piezoelectricity is the phenomenon described as the linear relation between a mechanical phenomenon and an electrical counterpart. A material is piezoelectric if the tension applied to it causes a dielectric displacement. This displacement manifests itself as a change in the polarization and causes a variation in the superficial density charge (Fleisch, 2008; Tichý *et al.*, 2010).

The direct piezoelectric effect was discovered in 1880 by the Curie brothers in tourmaline and quartz (Uchino, 2017). The direct piezoelectric effect manifests when electricity surges as a response to a change in the tension state, traction, or compression. The deformation

proportional to the electric field applied is called the converse piezoelectric effect, or indirect, and it was discovered one year later (Bowen; Topolov; Kim, 2016; Uchino, 2017).

The piezoelectric phenomenon is characteristic of materials that possess noncentrosymmetric unit cells, and it is not restricted to the ferroelectric state. When subjected to an electric field, all materials present a response that is not necessarily piezoelectric. More precisely, electric constriction might happen. If the change in the tension state causes a change in the dimension that leads to a change in the polarization state, the piezoelectric effect occurs. For this to happen, the material must be polar and crystalline because tension is a symmetric tensor, and only if the unit cell is not, the interaction has, as a result, an asymmetrical charge distribution (Tichý *et al.*, 2010).

Piezoelectricity, as ferroelectricity, results from specific structural features, i.e., noncentrosymmetry. Of the 32 point groups, 21 are not centrosymmetric, and from those, 20 present piezoelectricity. Of these, 20, 10 present reversible and spontaneous polarization, ferroelectrics, and the other 10 present piezoelectricity because they become polarized when subjected to a mechanical or electrical stimulus. Perovskites are widely known for presenting piezoelectricity and are the focus of this review later (Bain; Chand, 2017; Kao, 2004).

The polar crystal may present piezoelectricity and pyroelectricity (Tichý *et al.*, 2010). Pyroelectricity consists of the polarization state dependence, magnitude, and direction of heat transfer. The converse effect, on the other hand, is the change in the polarization state caused by temperature change and is called the electrocaloric effect (Tichý *et al.*, 2010).

In a practical sense, if we consider a tension state as shown in Figure 4 a), when the response of a material to a force (F) generates a piezoelectric charge (P) proportional to this force, the direct piezoelectric effect occurs. If the force is compressive, the polarization has an opposite direction. In the converse piezoelectric effect, Figure 4 b), an electric field generated by two charged plates results in deformation.

Figure 4 – Direct and converse piezoelectric effect

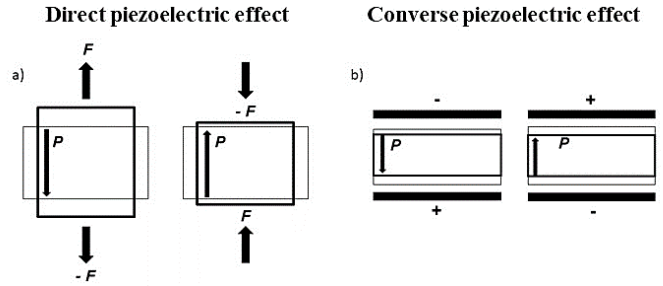

Source: Own authorship

Caption: a) Representation of the direct piezoelectric effect and b) Representation of the converse piezoelectric effect.

In both cases, the direction of the stimulus changes, and so does the polarization direction (Tichý *et al.*, 2010). These linear relations can be described by the equations (9) and (10) (Bain; Chand, 2017).

$$P_i = d_{ijk}\, T_{jk} \quad (9)$$

$$S_i = d_{ij}\, E_{Xj} \quad (10)$$

Equation (9) describes the direct piezoelectric effect, P_i is the polarization vector, d_{ijk} and T_{jk} are the tensors that represent the piezoelectric constant and tension, respectively. In equation (10), S_i is the strain and E_{Xj}, is the tensor that describes the electric field. In both equations, the polarization associated with the strain is always the same, regardless of its nature, in the case of mechanical input, direct piezoelectric effect, or caused by an electric field, converse piezoelectric effect. Both can be described by the piezoelectric constant (Tichý *et al.*, 2010).

One crucial characteristic of piezoelectrics is the magnitude of the mechanical strain when the material is subjected to an external electric field. All materials suffer a change in dimension when subjected to an external electric field. This happens because the electric field interferes with the electron clouds within the materials and changes their distribution, causing a distortion (Cardarelli, 2018; Kao, 2004). This phenomenon is called electrostriction, and although it is ubiquitous when materials are subject to an external electric field, its effect is mostly negligible. For ferroelectric materials, however, the converse piezoelectric effect is responsible for greater and more noticeable impacts.

Two cases may happen when a piezoelectric material is subjected to an external electric field. In the first one, the dipoles cancel each other in the unstrained condition. In this case, for a non-centrosymmetric material, the relation between the electric field and the generated mechanical strain is linear. In the second case, the dipoles add to the moment along the polar axis, the “stretched” axis. This means that in addition to the piezoelectricity, there is also pyroelectricity due to spontaneous polarization. This difference is easily spotted when strain is measured as a function of the applied electric field. For unstrained piezoelectrics, this measurement results in a straight line. For ferroelectrics, a butterfly loop is seen, which is formed due to hysteresis and non-linearity caused by polarization (Kao, 2004). The S-E graph shows mechanical strain as a function of an external electric field, which is essential in characterizing ferroelectric materials. For most ferroelectrics, the strain is proportional to the square of polarization, and through this measurement, hysteresis can be quantified, similar to the dielectric loss. In summary, in noncentrosymmetric materials, thermal, mechanical, and electrical phenomena are linked, as shown in Figure 5.

Figure 5 – Link between electrical, thermal, and mechanical phenomena in noncentrosymmetric materials

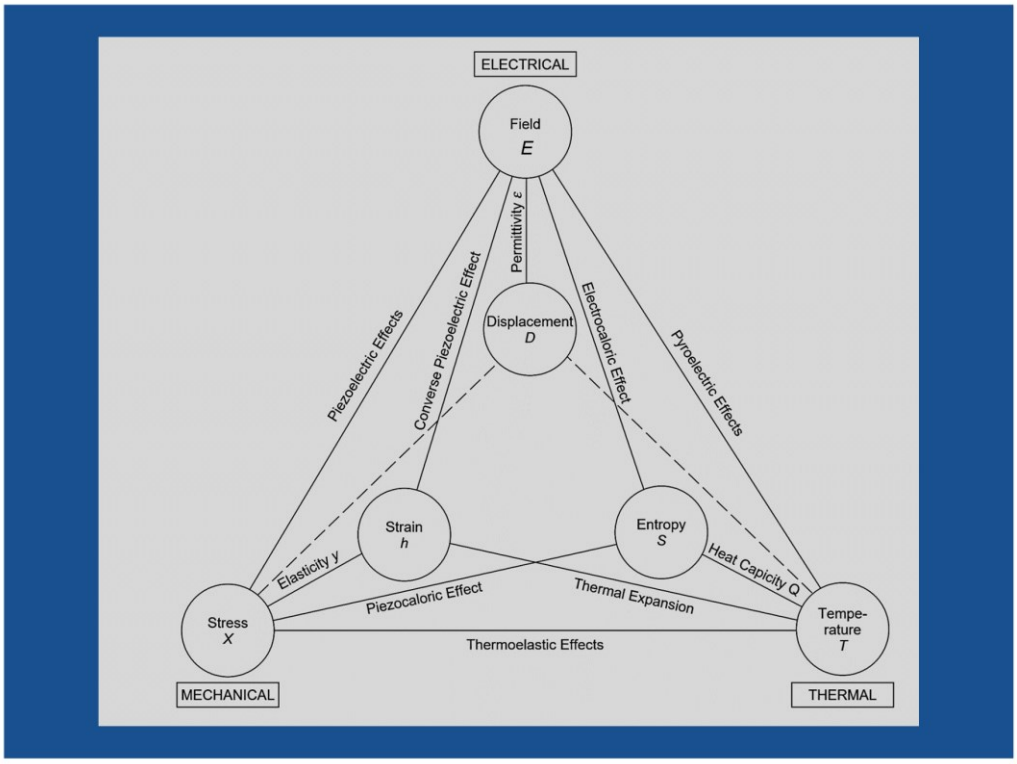

Source: (Kao, 2004)

From these relations, it is possible to characterize ferroelectric and piezoelectric materials and gauge performance. The most important figures of merit to characterize

piezoelectric materials are piezoelectric strain constant d, piezoelectric voltage constant g, the electromechanical coupling factor k, the mechanical quality factor Q_m, and the acoustic impedance Z (Uchino, 2017). The piezoelectric strain constant linearly links the electric field to the induced strain. This figure of merit is especially important for actuator applications. The voltage constant links linearly the applied stress to the electric field induced; this figure of merit is especially important for sensor applications. The electromechanical coupling factor measures the ability of the materials to convert electrical into mechanical energy. Other figures of merit link these quantities, but this specific one stands for the stored mechanical energy divided by the stored electrical energy, considering the converse piezoelectric effect. The electric energy obtained from conversion divided by the total input of mechanical energy gives the electromechanical coupling factor considering the converse piezoelectric effect (Kao, 2004). The mechanical quality factor characterizes the resonance spectra and assesses if the material is suitable for applications in resonance or off-resonance. The acoustic impedance is a parameter that describes the acoustic transference between two different materials (Uchino, 2017).

Considering the direct piezoelectric effect, the piezoelectric constants, or piezoelectric charge constants d_{13} and d_{33}, are extremely important for sensor applications (Zheng et al., 2018). In these constants, indexes 3 and 1 indicate the relative direction in which the stimulus and response to it occurs. In the dielectric constant d_{13}, the tension is applied in direction 1, and the induced electric field manifests in direction 3, perpendicularly, thus is a transversal electric coefficient. For d_{33}, the direction of the applied tension is the same as that of the electric field induced; this coefficient is called longitudinal (Bain; Chand, 2017).

Fundamentally, the application of piezoelectrics is divided into two major categories: sensor and actuator. Actuators are based on the converse piezoelectric effect, and sensors in the direct piezoelectric effect (Tichý *et al.*, 2010). The modern application of piezoelectrics is based on discovering that ferroelectrics have excellent piezoelectric properties and are more sensitive (Bain; Chand, 2017; Tichý *et al.*, 2010). Piezoelectric materials are intelligent because they can sense the environment and react predictably to a stimulus. They can be applied in this context as sensors and actuators or performing both operations acting as transducers (Hong *et al.*, 2016). Of the possible applications of these devices energy harvesting is considered promising, establishing the field of piezogenerators and piezonanogenerators, which have been gaining traction since the increased potential of the Internet of Things (IoT) and MEMs/NEMs

(microelectromechanical and nano-electromechanical systems) (Bain; Chand, 2017; Waqar *et al.*, 2022). Precision applications, use in severe environments, absence of lubrication, wear resistance, and low heat generation are some of the interesting characteristics of these devices that can be profitable in the ongoing increase of their usage.

To realize the full potential of these remarkable applications, piezoelectric materials have to be investigated regarding these major points: thermal stability, greater sensibility, higher electromechanical coupling, increased temperature-stable piezoresponse, development of fabrication-friendly processes, and tailorable compositions (Tichý *et al.*, 2010; Waqar *et al.*, 2022).

2.4 PEROVSKITES

In ferroelectrics and piezo-responsive-based devices, perovskites have been the paramount materials since the discovery of ferroelectricity in barium titanate. Perovskite is the name given to a group of compounds that present the ABX_3 general formula or formula derived or close to this basic one and encompasses a vast number of compositions. In the ABX_3 structure, A is a bigger cation, B is a smaller cation, and X is an anion. Further in this chapter, detailed structure descriptions will be given. The term perovskite itself comes from the mineral perovskite, $CaTiO_3$, calcium titanate, which lends its name to this whole group of compounds that encompasses materials that show interesting phenomena such as ferroelectricity, piezoelectricity, pyroelectricity, magnetism, and superconductivity. These phenomena make them candidates for applications in different fields such as catalysis, capacitors, sensors, actuators, superconductors, photovoltaic technology, photocatalysis, optoelectronics, and magnetoresistance amongst many others (Borowski, 2010; Fu *et al.*, 2019; Mahani *et al.*, 2010; Pan; Zhu, 2016; Panda, 2009; Vidyasagar; Muñoz Flores; Jiménez Pérez, 2018; Zhang *et al.*, 2010). Perovskites present behaviors that go from insulators to superconductors (Pan; Zhu, 2016), and a significant number of compounds follow the formula ABX_3 or derived formulas. This also explains the variety of properties and applications shown by these compounds and the great research demand on this topic.

These incredible properties, phenomena, and applications are based on specific structural features. The idealized structure, or aristotype, for perovskites, is presented by strontium titanate, $SrTiO_3$, at ambient conditions (Tilley, 2016). The structure is cubic, and the lattice cell parameters are as follows: $a = b = c = 0.3905$ nm belonging to the space group $Pm\bar{3}m$ (221), shown in Figure 6, obtained from the ICSD database (Inorganic Crystal Structure Database) (Fluck, 1996), card number 94573. The central position is occupied by titanium, the B cation in the ABX_3 structure, the atoms in the facets are oxygen, the X anions, and the ones in the vertices are strontium atoms, the bigger A cations. The oxygen atoms create an octahedron while coordinating the titanium atom.

Figure 6 – $SrTiO_3$ structure

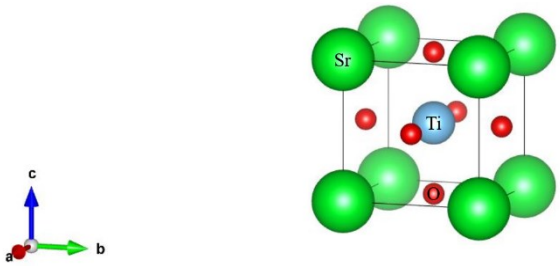

Source: Vesta (Momma; Izumi, 2011).

The idealized structure for perovskites obeys strict rules, and compositional change obligatorily leads to a change in the lattice parameters of the unit cell. It is essential to take into consideration that perovskites can be understood as ionic compounds, which is helpful to visualize why they can be so inflexible regarding the ideal structure.

The unit cell must be electrically neutral, and the oxide perovskites in which oxygen presents oxidation number (2-) must have two cations whose sum of oxidation states is equal to (6+) for the charge equilibria to be met. There is a multitude of possible arrangements that respect this criterion, such as $A^{1+}B^{5+}O_3$, $A^{4+}B^{2+}O_3$, $A^{3+}B^{3+}O_3$, and $A^{2+}B^{4+}O_3$. There is also the possibility for solid solution formation, such as $A_{1-x}A'_xB_{1-y}B'_yO_3$, and doping of these materials (Borowski, 2010; Pan; Zhu, 2016). Perovskites, however, are not restricted to oxides. There are several compounds related to its basic structure, such as nitrides and oxynitrides, antiperoviskites (A_3BX), organic-inorganic hybrids $(CH_3NH_3)PbX_3$, and halide perovskites. This number of possible configurations attests to its flexibility, which is used to tailor properties

and applications. Naturally, these structural alterations result in correspondent structural distortions parting from the ideal structure (Tilley, 2016).

To understand perovskites' features, it is helpful to consider some structural aspects. Analyzing the aristotype unit cell, assuming that B and X atoms touch each other and the unit cell is electrically neutral, one edge must have the length of two bonds between the atoms X and B, or in the examples given in Figure 6, oxygen and titanium. The diagonal in the cube's face has the length $\sqrt{a}$, in which a is the edge with the length two times the bond length between the atoms A and X. This distance is relevant because of the width of the octahedral site. These geometric considerations can be easily seen in Figure 7. The crystallographic plane highlighted in red is the (110).

These geometric relations were investigated first by Goldschmidt, considering the ionic radius instead of bond length, which the latter is more common nowadays (Borowski, 2010; Tilley, 2016). Through these geometric considerations, we have equations (11) and (12) that correlate the size of the ions in the unit cell for a cubic system, determining the viability of perovskite formation where R_A is the radius of the A atom, R_B is the radius of the B atom, and R_X the radius of the X atom.

Figure 7 – $SrTiO_3$ octahedral site

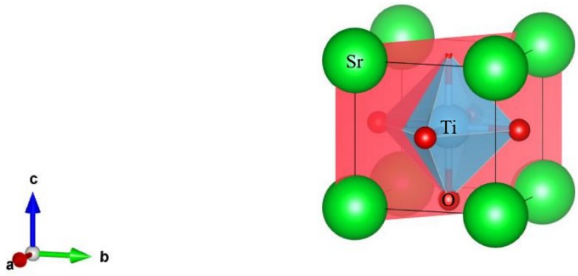

Source: Vesta (Momma; Izumi, 2011)

$$\frac{(R_A - R_X)}{(R_B - R_X)} = \sqrt{2} \quad (11)$$

$$\frac{(R_A - R_X)}{\sqrt{2}(R_B - R_X)} = 1 \quad (12)$$

The observed tolerance factor (t) is used to predict the structures of perovskites. Ideally, it must assume the value of 1. However, experimentally, since the bond lengths are measurable, it is between 0.9 and 1. In this case, the cubic perovskite is more probable. A hexagonal structure is more probable for t values above 1, where the A atom is much bigger than B. For t values between 0.71 and 0.9, structures less symmetric than cubic are formed, such as the orthorhombic (Borowski, 2010; Pan; Zhu, 2016; Tilley, 2016). Through equation (13), it is possible to predict the probability of perovskite formation using the calculated tolerance factor.

$$t = \frac{(R_A - R_X)}{\sqrt{2}(R_B - R_X)} = 1 \qquad (13)$$

The space group in which these compounds crystallize depends on the identity of the A, B, and X ions, which is an intrinsic factor. However, extrinsic factors come into play, i.e., temperature and pressure. In perovskites, the high-temperature phase is usually the paraelectric cubic phase.

In perovskites, most properties depend on the atoms that form the BX_6 octahedron and their relative orientation, showed in Figure 7. Alterations in this polyhedron can induce more expressive alterations in properties. Although the A atom is not irrelevant to the properties of these materials, it has a smaller impact on them. The simpler way to change the properties in a perovskite is to change the identity of the B atom, which can cause the structure to crystallize in a less symmetrical crystalline system, such as the tetragonal or orthorhombic. This is how permanent dipoles are formed in these compounds, and their electronic properties are altered (Pan; Zhu, 2016). The substitution of atoms in the A and B sites significantly impacts the structure, even in small concentrations, and has two primary aims. First to improve properties and second to extend pressure and temperature working range, and it's a common practice to control the ferroelectric and piezoelectric properties of perovskites (Tilley, 2016; Waqar *et al.*, 2022).

Dopants present either the same or a different oxidation number than the atoms they are substituting. The first case is configured as isovalent doping, and the second is aliovalent doping. Aliovalent dopants can either present a lower or higher oxidation number than the substituted atom; the first case is configured as acceptor doping, and the latter is donor doping. Aliovalent doping has several repercussions revolving majorly around maintaining neutrality.

Acceptor doping generates compensating methods such as oxygen vacancies and electron holes. This can generate complex defects arising from the interactions between dopant ions and the oxygen vacancies, which causes a local distortion in the elastic and electrostatic fields. This causes pining centers responsible for ferroelectric "hardening," meaning that they hinder wall motion. Hardening is characterized by i) pinched hysteresis loop, ii) reduced dielectric response, iii) reduced piezoelectric response, and iv) reduced dissipation (Acosta *et al.*, 2017).

In the case of donor doping in the A or B-sites, charge compensation occurs through the presence of free electrons, reduction of oxygen vacancies, and formation of cation vacancies. The effect of donor doping is the opposite of acceptor doping, and there is ferroelectric "softening" and increased domain wall mobility, resulting in greater dielectric loss, high remanent polarization, improved dielectric and piezoelectric properties (Acosta *et al.*, 2017).

Additionally to these structural considerations, three major types of distortions can be presented by perovskites: cationic displacement, rotation, or inclination of the BX_6 octahedron, and the octahedron's distortion by elongation or flattening (Tilley, 2016). In the cationic displacement, the B atom is smaller than in the idealized structure for the octahedral site, causing the perovskite to crystallize in a structure not as symmetrical, which depends on the degree of distortion caused by the direction of the displacement. Rotation and inclination of the octahedron occur by the presence of an A cation smaller than the idealized one. Incidentally, the octahedron adjusts itself to fill this cavity, reducing the symmetry of the structure. The distortion of the octahedron occurs due to a change in the valence of the atoms, where cations of different sizes also form octahedra of different sizes. Interaction between orbitals in cations and anions also leads to distortions, as it happens for B cations that present electronic configuration d^n, explained by the Jahn-Teller effect. In this case, d^n cations are more stable in a distorted octahedron than in a perfect one. These phenomena can occur separately or simultaneously (Tilley, 2016).

Defects, doping, chemical heterogeneities, and structural distortions directly impact properties, but extrinsic factors such as temperature and pressure also critically impact performance. As applications under a temperature gradient are more prevalent than the ones under an important pressure range, temperature-induced phase transitions are discussed herein. This is especially true for perovskites since they usually experience a sequence of phase transitions and flux from paraelectric to ferroelectric phases, which limits applications. For

example, if excellent piezoelectric properties are desired, the sample must crystallize in the noncentrosymmetric phase in the working temperature range. The most critical impacts of temperature in perovskites arise from the transition that occurs from ferroelectric to the paraelectric phase at the Curie temperature, which has already been discussed, as well as possible MPB (morphotropic phase boundary) or PPB (polymorphic phase boundary) formation.

Using barium titanate (BT) as an example since it is the base composition from which the BCZT system originates, the impact of temperature on phase dynamics can be exemplified as follows. Barium titanate experiences a series of first-order temperature-induced phase transitions. At room temperature, barium titanate crystallizes in the tetragonal structure, the ferroelectric phase. However, the structure presented depends on the temperature. Under -90 ^{o}C, barium titanate presents a rhombohedral structure (R3m). Between -90 and 5 ^{o}C, the structure is orthorhombic (Amm2). Between 5 and 120 ^{o}C presents the tetragonal phase (P4mm), and over 120 ^{o}C undergoes a phase transition to the cubic phase ($Pm\bar{3}m$), the paraelectric phase (Acosta *et al.*, 2017; Kao, 2004). As it occurs at the T_C, a softening occurs at this transition point, which results in the increase of ε_r at three maxima points. Additionally, it's a region where mechanical thermal, dielectric, and piezoelectric properties present anomalies that are exploited in device applications (Acosta *et al.*, 2017). These phase transitions directly impact polarization and, consequently, are crucial to piezoelectric, dielectric, and ferroelectric properties, but they are not exclusive to BT. This behavior is characteristic of perovskites overall.

These phase transitions may present special features, such as a coexistence of phases that facilitates polarization, which results in superior performance and properties. The MPB is a phase boundary (between rhombohedral and tetragonal phases). This unstable region is composition-dependent with a vertical phase boundary where the flattening of the free-energy profile facilitates polarization. This occurs because polarization takes place in more orientations, so more domains are aligned to be polarized (Tichý *et al.*, 2010; Waqar *et al.*, 2022; Wu, 2020). The greater the polarization, the greater the piezoresponse, resulting in improved performance. This fact makes MPB engineering an exciting technique for obtaining superior properties. Regarding the MPB, there is also a distinction between a "true" MPB, which is virtually unaffected by temperature, and a temperature-dependent MPB, which is called a PPB. An example of a "true" MPB is the one present in PZT; a temperature-dependent

MPB occurs in lead-free perovskites such as BCZT, which is more unstable (Wu, 2020). For the latter, a change in temperature leads to the dissolution of the multiple-phase arrangement.

Perovskites are often classified based on lead presence. This happens because the PZT system ($PbZr_{1-x}Ti_xO_3$) is the paramount perovskite material due to its exceptional performance and thermal stability, and it has been studied for over 40 years. This is entirely connected to its steep MPB, around x = 0.48, which allows for outstanding properties (Wu, 2020). PZT is a solid solution. On one end, there is the PZN composition $Pb(Zn_{1/3}Nb_{2/3})O_3$ that presents a trigonal ferroelectric structure (3m). On the other end, the PT composition ($PbTiO_3$) presents a tetragonal ferroelectric structure, both at room temperature. At the Curie temperature, both compositions transit to the paraelectric cubic phase ($m\bar{3}m$), which is high, varying from 150 to 250 ^oC depending on the lead titanate concentration (0 to 20% PT content). The MPB content is in the range of 8 to 10% PT concentrations and consists of the coexistence of tetragonal and rhombohedral phases, allowing for 8 domain states for the rhombohedral and 6 for the tetragonal phase (Tichý *et al.*, 2010).

However, it is widely known that lead is detrimental to human health, and stronger regulations against its use inhibit its application, although compounds that have lead in their composition present excellent piezoelectric properties and are commercially popular (Chen *et al.*, 2020; Wu, 2020; Zheng *et al.*, 2018; Zimmerman *et al.*, 2020). Even though lead-free perovskites present high spontaneous polarization, they still have challenges to surpass to become a viable option for lead compositions. First, the complexity of the compositions and, second, the temperature dependence and sensibility regarding properties and the MPB must be solved (Waqar *et al.*, 2022). For these reasons, lead-free perovskite compositions are in demand for research.

2.4.1 BCZT ceramics and the influence of Ce and V doping

In the field of perovskites, lead-free systems have been extensively studied as a solution for greener and more eco-friendly options to PZT. Amongst them, the BCZT system has gained considerable traction. BCZT is a substitutional solid solution of barium titanate in which calcium occupies barium's site and zirconium titanium's site, the A and B sites, respectively. In this solid solution, zirconium and calcium are soluble in any concentration. Barium titanate presents a tetragonal structure at room temperature. However, the presence of Ca smaller atoms

(1.35 Å) in the A site substituting barium's larger atoms (1.60 Å), and Zr (0.72 Å) substituting the Ti smaller atoms (0.605 Å) causes a distinctive structural change.

This system was first brought to the attention in 2009 and extensive research on its structural, ferroelectric, piezoelectric, and dielectric properties was performed (Liu; Ren, 2009). After this groundbreaking work, BCZT became a topic of interest due to its PPB composition, $Ba_{0.85}Ca_{0.15}Zr_{0.1}Ti_{0.9}O_3$ (Bai *et al.*, 2015; Buatip *et al.*, 2020; Hanani *et al.*, 2019; Kou *et al.*, 2022; Sahoo *et al.*, 2021). Since the discovery of PZT MPB composition, there has been a movement to determine similar composition points for other perovskites due to the possibility of obtaining superior properties. Considering the work of Liu and Ren, BCZT has a critical triple point where tetragonal, rhombohedral, and cubic phases coexist, as shown in Figure 8 a). The two ferroelectric phases would then form the MPB; however, there has been discussion about the presence of an intermediate phase instead.

This symmetry break has been investigated and was deemed to consist of an alternative lower symmetry phase. According to Keeble, see Figure 8 b), alternatively to Liu and Ren, BCZT presents an orthorhombic intermediate phase (Keeble *et al.*, 2013). Regardless, excellent properties can be found near this composition point due to an easier polarization caused by the reduction of the energy barrier to 0 between polarization direction vectors of both terminal phases at the tricritical point (TCP), cubic, tetragonal, and rhombohedral phases, which incidentally impacts positively in dielectric permittivity and piezoelectric coefficient values (Bao *et al.*, 2010). Thus, the best properties of this system can be found at the MPB. Slightly away from it, the properties are less impressive but can be more thermally stable (Liu; Cheng; Li, 2019; Liu; Ren, 2009).

Figure 8 – Proposed phase diagrams for BCZT

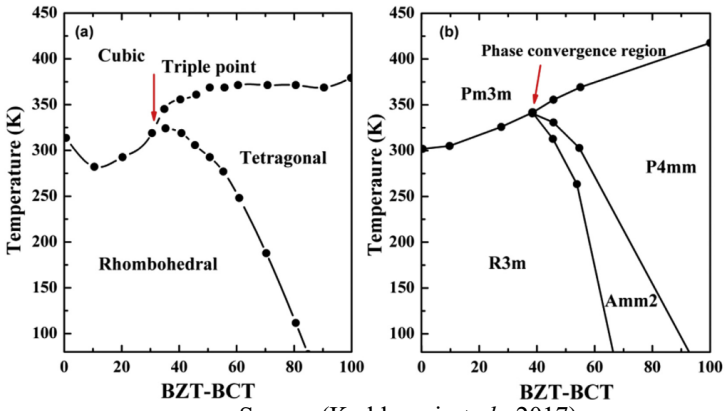

Source:(Kaddoussi *et al.*, 2017)

Caption: a) Phase diagram of BCZT as proposed by Liu and Ren and b) Revised phase diagram of BCZT as proposed by Keeble.

As with most ferroelectric ceramics, solid-state sintering is the most common synthesis method for BCZT, but sol-gel is also reported quite frequently (Mezzourh *et al.*, 2021). The properties presented by BCZT ceramics produced by the sol-gel method are consistent with the ones of BCZT synthesized by the solid-state method while also presenting lower calcination temperatures (Belkhadir *et al.*, 2019; Coondoo *et al.*, 2018; Mezzourh *et al.*, 2021; Praveen *et al.*, 2015). Another critical point is that the properties of BCZT vary significantly between different works. Microstructure plays a significant role in this variation, and processing is the primary factor (Bai *et al.*, 2015).

The major appeal of BCZT PPB composition is the superior properties found at this compositional point, summarized in the next paragraph.

The PPB is known for its softness, exemplified by the low E_c of 1.68 V/cm, high permittivity of 3060, high remanent polarization of almost 16 μC/cm^2, and high piezoelectric coefficient of 620 pC/N, T_C decreases to 75 ºC, considerably lower in comparison to BT, which is 120 ºC (Liu; Ren, 2009). Considering these properties, BCZT presents an excellent potential for energy harvesting applications, and doping can further improve these properties, as it happens with the addition of acceptor dopants such as zinc and manganese and donor dopants such as lanthanum, chromium, and gallium (Liu; Cheng; Li, 2019).

BCZT ceramics have a high sintering temperature necessary to develop dense microstructures, around 1300 ºC, at the optimum point or even higher, around 1475 ºC (Bijalwan *et al.*, 2019b; Liu; Ren, 2009; Wang; Li; Lu, 2011).

Doping generally has as objectives the control and improvement of the properties of materials. In perovskites, these improvements are associated with better dielectric, ferroelectric, and piezoelectric performances for a specific application. In these materials, doping is amply applied, partly due to the great malleability allowed by the structure in exchange for structural alterations. Firstly, before considering the effects of doping, it is necessary to have a brief discussion about the relaxor behavior in perovskites.

When ferroelectricity is discussed, for our work, we can divide its behaviors into two different types: the classic ferroelectric behavior and the relaxor behavior. This review has already discussed the classic ferroelectric behavior, whereas the relaxor behavior is discussed herein. The relaxor behavior occurs due to ionic substitution in the A and B sites. The general tendency is that a greater concentration of dopants, aliovalent doping, co-doping, and doping of ferroelectrically active sites more easily induce relaxor behavior (Mahajan *et al.*, 2009). The

control of these doping factors determines if the composition will present a classic or relaxor ferroelectric behavior.

The relaxor behavior can be explained as a significant frequency dependence of the dielectric constant, more specifically, a dispersion of the maximum value of the dielectric constant as a function of frequency and temperature (Aoujgal *et al.*, 2011).

It is possible to tailor properties, optimize processing, and improve overall piezoelectric, ferroelectric, increase thermal stability, and dielectric properties through doping. Considering the improvement of processing, doping can be a helpful tool in reducing sintering temperature. This is the case for vanadium and cerium doping.

As a donor dopant, cerium can act as a sintering aid, reducing sintering temperature and controlling grain growth. The addition of Ce significantly impacts microstructure, and due to its relation to densification and grain size, it will directly affect piezoelectric properties. First, it promotes lower sintering temperature and, second, permits greater grain size control.

Cerium is a lanthanide with an atomic mass of 140.116 amu. Its abundance on earth is 66.5 mg/kg, the most abundant lanthanide. This element was discovered in Sweden in 1801 and was named in homage to the asteroid Ceres (Cardarelli, 2018). In the BCZT structure, Ce is a donor dopant in the A site because of its size, although due to different oxidation states, +3 and +4, it can also be a B site isovalent dopant (Cui *et al.*, 2012; Hayati *et al.*, 2019). For atomic coordination 8, Ce^{4+} has a 0.97 Å ionic radius, and Ce^{3+} has a 1.14 Å ionic radius (Shannon; Prewitt, 1969).

At the PPB composition, BCZT presents a mix of tetragonal and rhombohedral structures or an intermediate phase (Kaddoussi *et al.*, 2017; Liu; Ren, 2009). Regardless, Ce doping certainly is responsible for structural changes in this composition. The alteration of lattice parameters when the Ce atoms enter either A or B sites is the most blatant one, observable by X-ray diffraction patterns.

Most structural investigations are done through XRD analysis and are subjected to its limitations, mainly related to sensitivity. Additionally, structurally solving structures in transition phase regions is not trivial. Generally, the structure evolution for BCZT passes from the lower Ce concentration that allows the maintenance of the PPB to the extreme of higher concentrations that leads to a cubic structure formation, which induces the paraelectric state at lower temperatures. The best piezoelectric properties for Ce-doped BCZT are reported to be

around 0.02 mol% concentration, and the PPB is expected to be maintained. Table 1 summarizes the structural data related to BCZT Ce-doped compositions with all the references needed.

Table 1 – Structural data on Ce-doped BCZT

Composition		Crystalline system				Reference
		C	O	T	R	
$[(Ba_{0.85}Ca_{0.15})_{1-x}Ce_{x/2}](Zr_{0.1}Ti_{0.9})O_3$ for $0 \leq x \leq 0.05$	Ce = 0 mol%	0%	86%	14%	-	(Hayati *et al.*, 2019)
	Ce = 0.025mol%	0%	91%	9%	-	
	Ce = 0.05 mol%	0%	96%	4%	-	
	Ce = 0.25 mol%	11.2%	75%	15%	-	
	Ce = 2.5 mol%	88.9%	10%	2%	-	
$(Ba_{0.85}Ca_{0.15-x}Ce_x)(Zr_{0.1}Ti_{0.9})O_3$	x = 0–0.00131	-	-	x	x	(Bijalwan; Tofel; Holcman, 2018)
	x = 0.02	x*	-	-	-	
$(Ba_{0.85}Ca_{0.15})(Ti_{0.9}Zr_{0.1})O_3$ – 0.1 mol %		x	-	-	-	(Praveen *et al.*, 2015)
$(Ba_{0.85}Ca_{0.15})(Zr_{0.1}Ti_{0.9})O_3$	0 – 0.125 mol%	-	-	x	x	(Bijalwan *et al.*, 2019b)
	0.625-3.75 mol%	-	-	-	x	
$(Ba_{0.85}Ca_{0.15})(Ti_{0.9}Zr_{0.1})O_3$	0 – 0.125 mol%	-	-	x	x	(Cui *et al.*, 2012)
$(Ba_{0.85}Ca_{0.15})(Zr_{0.1}Ti_{0.9})O_3$ for 0 – 0.875 mol%		-	-	x	-	(Bijalwan; Tofel, 2019)

Source: Own authorship.

Caption: * Pseudo-cubic C stands for cubic, O, is for orthorhombic, T, is for tetragonal, and R for rhombohedral.

In most reports regarding the sol-gel synthesis of Ce-doped BCZT compositions, Ce is added as a sintering aid in the form of CeO_2 to the calcinated BCZT powder prepared by the sol-gel method. The work of Chandrakala is the exception. In this case, Ce is added in mol% during the sol-gel process, and calcination is carried out afterward (Chandrakala *et al.*, 2020).

It is helpful to notice that a 0.08 wt% CeO_2 concentration corresponds to a 0.02 mol% Ce concentration in BCZT, Ce occupying either A or B site. For the first work reviewed herein, the powder resulting from the sol-gel synthesis was calcinated at 1000 ºC for 4 hours, 0.08 wt% of CeO_2 was mixed into the calcinated powder, and after incorporation, pellets were sintered at 1550 ºC for 2 hours. Through XRD, a single cubic phase was identified. Concerning microstructure, the pellets presented 97% relative density and 15 μ medium grain size. These samples presented P_r of 1.58μC/cm^2 and Ec of 1.6 kV/cm. Under optimum poling parameters

of $3E_c$, for 30 minutes at 50 ºC, a piezoelectric charge coefficient of 667 pC/N was obtained (Chandrakala; Praveen; Das, 2016).

The second work reports the investigation of Ce-doped BCZT samples, with Ce concentration varying between 0.02 and 0.10 wt% CeO_2. Cerium oxide is added as a sintering aid to the calcinated BCZT powder. A calcination temperature of 1000 ºC for four hours and a sintering temperature between 1350°C and 1550°C for two hours were performed to obtain dense samples. Sintered samples showed no sign of second phases through XRD patterns' analysis. Lattice parameters reduction attests to the Ce substitution in the B site due to cerium's bigger ionic radius than Ti and Zr. For $x \leq 0.04$ wt% CeO_2, samples present a tetragonal structure. Over 0.06 wt% CeO_2, samples show signs of mixed phases nearing the PPB from the tetragonal side. For 0.08 wt% CeO_2 concentration, there is a mix of rhombohedral and tetragonal structures, and at 0.1 wt% CeO_2, there is only a rhombohedral structure present. Another impact of Ce addition is the increase in tetragonality in the range from 0.02 to 0.04 wt% CeO_2. The structural features of this composition give origin to an increase of strain in the lattice and induce phase transition (Chandrakala *et al.*, 2016). The optimum value for CeO_2 doping is 0.08 wt%, considering all properties. Please refer to Table 2.

Considering reports on Ce-doped BCZT synthesized by solid-state reaction, CeO_2 is commonly added in weight percentage (%wt) to the BCZT powder. In Table 2, the relevant data is assembled for easier understanding. An extensive array of data and multiple microstructural factors must be considered; however, some important information can be extracted. The ideal concentration of CeO_2 on BCZT is found to be around 0.1 wt%. Moreover, It is important to notice that Ce has 0.131 mol%, or 0.1048 wt% CeO_2, solubility limit in BCZT (Bijalwan; Tofel; Holcman, 2018). From all the works reported here, the best densification is obtained when two-step sintering is performed, with 99% relative density. However, the samples in this case present grain size under 10 μm, which is not ideal (Bijalwan; Tofel, 2019). This is easily remediable by controlling sintering parameters to favor grain growth to at least 15 μm, maintaining almost full densification. Another important factor is the determination of optimum poling conditions. This is required to obtain the best possible values for piezoelectric properties, and this was the case for the excellent value of 670 pC/N obtained for 0.08 wt% CeO_2. In the most recent work regarding Ce-doping, Ce doping is allied to a rapid sintering technique to potentialize sintering optimization, which shows how important this subject is (Bijalwan *et al.*, 2022). Aligning increased densification, adequate grain size, optimum Ce concentration, and optimum poling parameters, above-average properties can be obtained.

Table 2 – Ce-doped BCZT data

Synthesis method	Optimum composition	ε_r	P_r ($\mu m/cm^2$)	E_c (kV/cm)	d_{33} (pC/N)	Tc (°C)	Grain size (µm)	Reference
Solid state	BCZT - 0.07 wt% CeO_2	4091	16.32	2.13	507	104.6	~ 15	(Bijalwan *et al.*, 2019b)
Sol-gel	BCZT - 0.08 wt% CeO_2	-	11.58	1.6	670	-	~ 15	(Praveen *et al.*, 2015)
Solid state	BCZT – 0.1 wt%	~ 11000	12.19	4.57	501	108.1	11.26	(Bijalwan; Tofel; Holcman, 2018)
Ceramic process	BCZT – 0.04wt%	4843	-	-	600	~ 90	-	(Cui *et al.*, 2012)
Solid State	$(Ba_{0.85}Ca_{0.15})_{1-x}Ce_{x/2}(Zr_{0.1}Ti_{0.9})_3$ – 0.05 mol% - Ce	2730	11.6	2.4	1189@	93		(Hayati *et al.*, 2019)
Sol-gel	BCZT - 0.08 wt% CeO_2	~ 12500	12.01	1.57	673	110	18	(Chandrakala *et al.*, 2016)
Sol-gel	BCZT - 0.08 mol% CeO_2	3070** 4890***	12.36**	1.55**	703** 660***	123** 104***	-	(Chandrakala *et al.*, 2020)
Solid state*	BCZT - 0.07 wt% CeO_2	3393	11.45	2.32	353	96.2	7.96	(Bijalwan; Tofel, 2019)
Solid state@@	BCZT - 0.07 wt% CeO_2	3180	8.37	2.33	515	102 - 103	30–35	(Bijalwan *et al.*, 2022)

Source: own authorship.

Caption: * Two-step sintering; ** Substitution in the Ti site; *** Substitution in the Zr site; @ pm/V. @@ rapid pressureless sintering (RPLS)

Related to processing, an increase in sintering temperature typically leads to improved properties when densification and grain size increase to a limit. However, it is more interesting to have a lower sintering temperature, and due to the impact of Ce on densification and grain growth, it is possible to process Ce-doped BCZT at a lower temperature. Table 3 showcases calcination temperature, calcination time, sintering time, and temperature for Ce-doped BCZT ceramics.

Table 3 – Thermal treatment data on Ce-doped BCZT

Synthesis method	Optimum composition	Calcination temperature (ºC) /Time (h)	Sintering temperature (ºC)/Time (h)	Grain size (µm)	Reference
Solid-state	BCZT - 0.07wt% CeO_2	1250 / 2	1350 / 4	~ 15	(Bijalwan *et al.*, 2019b)
Sol-gel	BCZT - 0.08wt% CeO_2	1000 / 4	1550 / 2	~ 15	(Praveen *et al.*, 2015)
Solid-state	BCZT – 0.1wt%	1250 / 2	1350 / 4	11.26	(Bijalwan; Tofel; Holcman, 2018)
Ceramic process	BCZT – 0.04wt%	1250 / 2	1350/ 4	-	(Cui *et al.*, 2012)
Sol-gel	BCZT - 0.08mol% CeO_2	1000/4	1550/2	-	(Chandrakala *et al.*, 2020)
Sol-gel	BZT-BCT–0.08 wt% CeO_2	1000/4	1550/2	2-18	(Chandrakala *et al.*, 2016)
Solid-state*	BCZT - 0.07wt% CeO_2	1250 / 2	1400 / 0.5 – 1275 /4	7.96	(Bijalwan; Tofel, 2019)
Solid-state	$Ba_{0.85}Ca_{0.15}$ $Zr_{0.9\ -x}Ce_{0.01}Ti_{0.1}O_3$	1150/4	1500/0.5**	2.37	(Kola; Ramesh; Swamy, 2023)

Source: Own authorship.

* Two-step sintering ** Microwave sintering.

Less investigated, vanadium was also determined to lower the sintering temperature of BCZT. Vanadium, atomic number 23, relative atomic mass 50.9415(1), density 6110 kg · $m^{-3,}$ is a metal and can be inserted into the structure of BCZT, substituting Zr or Ti (Cardarelli, 2018). V^{4+} (0.59 Å) and V^{5+} (0.54 Å), due to their size, occupy the B site in the ABX_3 structure when doping takes place (Shannon; Prewitt, 1969). Herein, recent works related to BCZT doping with vanadium are discussed.

Considering synthesis, the conventional solid-state is usually the chosen method and vanadium pentoxide (V_2O_5) is the precursor chosen to introduce vanadium into the BCZT

lattice. One important factor is the toxicity of vanadium compounds, considering the safety sheets of both compounds, V_2O_5 is considerably more deleterious to human health during its handling than $VOSO_4 \cdot 5H_2O$, for example. In the work of Yang, the solid-state method is carried out to produce samples with the following compositions $(Ba_{0.85}Ca_{0.15})(Ti_{0.9}Zr_{0.1})O_3$-x mol% V_2O_5 (x = 0, 0.05, 0.15, 0.20 and 0.50) to understand the impact of vanadium pentoxide especially in sintering temperature (Yang *et al.*, 2019). The sintering temperature indeed is reduced to 1350 ºC in addition to the increase in density and grain size. Considering the properties presented, 0.5 mol% seems to be the limit in which optimum properties can be found. For x = 0.2 mol%, optimum performance is achieved and the following figures of merit were determined: d_{33} = 466 pC/N, k_p = 32.5%, Q_m = 162, Pr = 7.735 μC/cm^2, ε_r = 3104 and tan δ = 0.03 (Yang *et al.*, 2019). Looking closely at the processing, we see that the calcination temperature carried out is considerably high, 1200 ºC. The incorporation of vanadium pentoxide was done after the calcination of BCZT, followed by pressing and sintering at 1350 ºC. Regarding the structure of sintered samples, XRD attests to the full introduction of the dopant; no second phase was identified, and a pure perovskite phase was formed. The introduction of V caused the diffraction peaks to shift to lower diffraction angles, which is deemed to happen due to the substitution of V^{5+} in the B site, considering the ionic radius of vanadium to be 0.74 Å, as referenced by Yang. This causes the lattice parameters to increase. Over x = 0.50, the ions start to occupy the A site. In this case, there's a subtle peak shift to higher angles. Up to x = 0.20, the structure presented is tetragonal. Over x = 0.20, there is a coexistence of tetragonal and rhombohedral phases (Yang *et al.*, 2019).

In more recent work, the composition $Ba_{0.9}Ca_{0.1}Ti_{0.9-x}V_xZr_{0.1}O_3$ (x = 0, 0.01, 0.02, 0.03, 0.04) was obtained from conventional solid-state synthesis. All samples crystallized in a tetragonal structure, *P*4*mm*, and a secondary phase of $Ba_3V_2O_8$ was nucleated in all samples. Calcination was performed at 1150 ºC to obtain dense samples, with 3 hours dwell time. After pressing, sintering was carried out at 1350 ºC for four hours. XRD patterns attested to the vanadium, V^{4+}, occupation of the B site causing the promotion of the tetragonal phase and the increase of unit cell volume with the increase of vanadium concentration. Tetragonality, c/a, suffered little change due to the presence of V, only noticeable when x is 0.04, when a slight reduction occurs, from 1.003 to 1.002. Crystallite size, on the other hand, increases with vanadium content, from 48.099, for x = 0, to 54.269, for x = 0.04. It is worth noticing that V^{+5} is also present, modulates the structural, electrical, and optical properties, and directly relates to the oxygen vacancies. From this exact measurement, it is possible to infer that the solubility

limit of vanadium in BCZT is 1 mol percentage. In those samples, vanadium doping caused the reduction of BCZT's Curie temperature with the increase of its concentration to the remarkably low value of 31 ºC when x = 0.04 (Verma *et al.*, 2021).

3 EXPERIMENTAL PROCEDURES

This section describes the experimental procedure for synthesizing and characterizing BCZT, Ce-doped BCZT, V-doped BCZT, and Ce and V co-doped BCZT samples.

3.1 SOL-GEL SYNTHESIS

Pure BCZT ($Ba_{0.85}Ca_{0.15}Ti_{0.9}Zr_{0.1}O_3$), cerium-doped BCZT, vanadium-doped BCZT, and vanadium and cerium co-doped BCZT gels were synthesized by the sol-gel method. The synthesis process is divided into two parts: the production of solutions 1 and 2, which are mixed and agitated once prepared to obtain the desired stoichiometry. For the labeling and composition of the samples, refer to Table 4. The original synthesis route from Köllner for BCZT was adapted to perform the doping and co-doping by Ce and V exclusively by the sol-gel method (Köllner *et al.*, 2023). This route has advantages, first, the use of barium and calcium oxides as well as ethanol instead of isopropanol, which are less expensive options. Secondly, the use of $VOSO_4 \cdot 5H_2O$ as vanadium precursor instead of V_2O_5 is a safer option to produce the V-doped compositions.

Table 4 – Composition and labeling of samples

Composition	Sample Labeling
$Ba_{0.85}Ca_{0.15}Ti_{0.9}Zr_{0.1}O_3$	BCZT-U
$Ba_{0.85}Ca_{0.15}Ti_{0.9}Zr_{0.1}O_3$ - 0.02% mol of Ce	BCZT-A
$Ba_{0.85}Ca_{0.15}Ti_{0.9}Zr_{0.1}O_3$ - 0.01% mol of Ce	BCZT-C
$Ba_{0.85}Ca_{0.15}Ti_{0.9}Zr_{0.1}O_3$ - 0.4% mol of V	BCZT-B
$Ba_{0.85}Ca_{0.15}Ti_{0.9}Zr_{0.1}O_3$ - 0.3% mol of V	BCZT-D
$Ba_{0.85}Ca_{0.15}Ti_{0.9}Zr_{0.1}O_3$ - 0.02% mol of Ce, 0.4% mol of V	BCZT-AB
$Ba_{0.85}Ca_{0.15}Ti_{0.9}Zr_{0.1}O_3$ - 0.02% mol of Ce, 0.3% mol of V	BCZT-AD
$Ba_{0.85}Ca_{0.15}Ti_{0.9}Zr_{0.1}O_3$ - 0.01% mol of Ce, 0.4% mol of V	BCZT-CB
$Ba_{0.85}Ca_{0.15}Ti_{0.9}Zr_{0.1}O_3$ - 0.01% mol of Ce, 0.3% mol of V	BCZT-CD

Source: Own authorship.

For pure BCZT, the synthesis is performed as follows. To produce solution 1, 175 g (9.7 mol) of distilled water was poured into a glass bottle and placed under agitation over a magnetic stirrer/hot plate (WiseStir MSH-200). 75 g (1.2 mol) of 100% glacial acetic acid (Supelco.) was added to the water. Under continuous agitation, 2.7 g (0.026 mol) of $CaCO_3$ (Sigma Aldrich, 99%) was added slowly to the solution, followed by the addition of 30.1 g (0.15 mol) of $BaCO_3$ (Alfa Aesar, 99%). This solution was left under agitation until no discernible particles were identified and until the second part of the synthesis process was completed. To produce solution 2, 49 g (1.1 mol) of ethanol (Euro denatured VNR Chemicals, 99%) was poured into a second glass bottle and kept under agitation, followed by the addition of 45.9 g (0.16 mol) of 97% titanium isopropoxide IV (Sigma Aldrich) slowly with a pipette. 5.9 g (0.018 mol) of zirconium IV n-propoxide 70% w/w in n-propanol (Alfa Aesar) was added with a pipette under continuous agitation. Finally, 117 g (1.9 mol) of glacial acetic acid was added to the same bottle. Solution 2 was under agitation until it was time to pour into solution 1.

After confirming that there were no discernible particles in both solutions, solution 2 was poured into solution 1 bottle. This sol was left to age for 24 hours under continuous agitation on a magnetic stirrer. Mass was measured on a precision balance (Kern 572). The overall process can be seen in Figure 9.

A similar synthesis process was adopted for the cerium-doped samples, except after the barium and calcium carbonate addition, an extra step of $CeCl_3 \cdot 7H_2O$ (Alfa Aesar, 99%) addition was taken. To produce Ce-doped BCZT sols, 0.067 g (0.18 mmol) of $CeCl_3 \cdot 7H_2O$ for the BCZT-A composition and 0.0335 g (0.9 mmol) for the BCZT-C composition were added. Ce chloride mass measurement was carried out in an analytical balance (Sartorius A200S). Refer to Table 4 for sample composition and labeling. The process can be seen in Figure 9.

First, the appropriate vanadium precursor solutions were prepared for the vanadium-doped samples. Vanadyl sulfate pentahydrate (VWR chemicals, Technical) was dissolved under agitation in distilled water. Water was the chosen solvent because, per the supplier's technical information, vanadyl sulfate pentahydrate is readily soluble in water and is already the solvent used for solution A. For the BCZT-B composition, 0.89 g (3.53 mmol) of vanadyl sulfate was dissolved in 5.4 g (0.3 mol) of distilled water. For the BCZT-D composition, 0.7 g (2.77) mmol was dissolved in the same solvent, 4.37 g (0.24 mol). The vanadium precursor was added to solution 1 before the carbonates were added; refer to Table 4 for sample composition and labeling. The process can be seen in Figure 9.

Figure 9 – Synthesis process

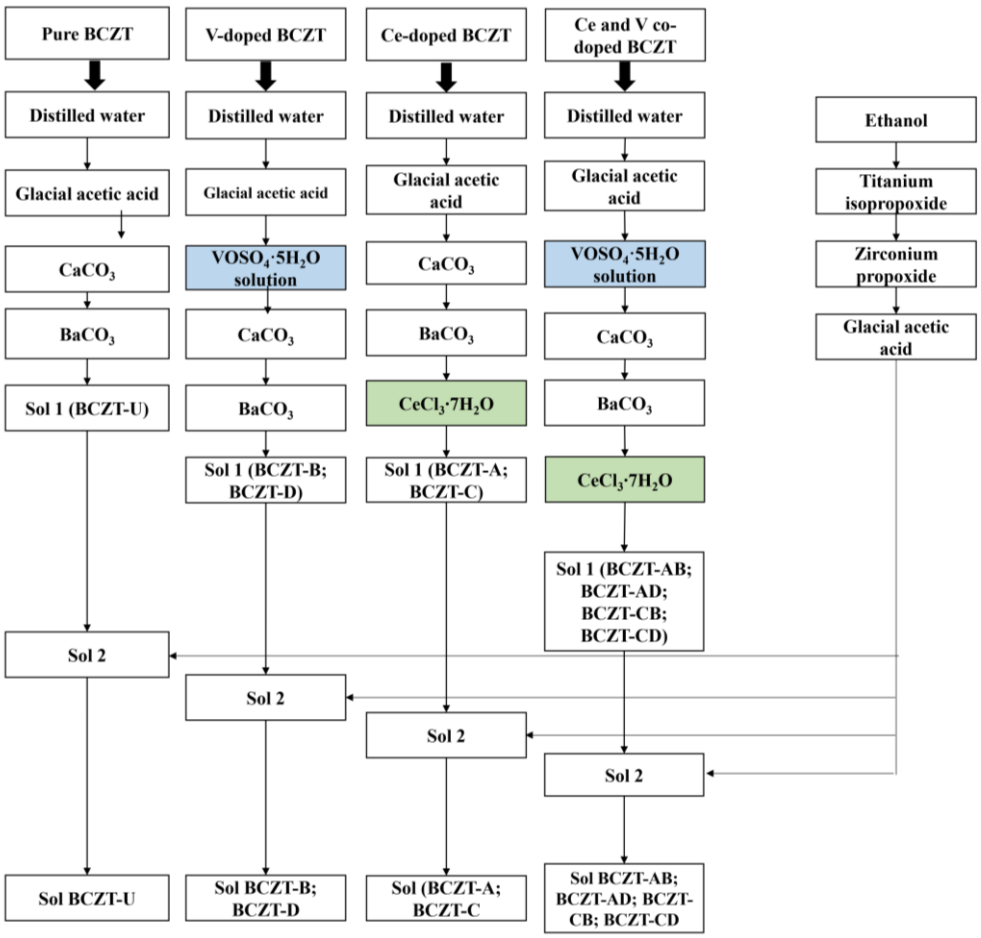

Source: Own authorship

For the Ce and V co-doped samples, the appropriate amounts of dopants were added to BCZT in the same respective steps as the doped compositions. Refer to Table 4 for sample composition and labeling. The process can be seen in Figure 9.

The samples were gelled after aging for 24 hours. Gelling was promoted by pouring the aged solution into a disposable aluminum tray and gradually increasing the temperature using a hot plate. First, 10 minutes at 190 ºC, then 20 minutes at 200 ºC, and last, rising to 215 ºC and maintaining this temperature until complete gelation was achieved.

Pure BCZT and cerium-doped samples went from transparent to dark blue during gelation. Co-doped and V-doped samples went from a light brown to a darker brown color. It was observed that undoped BCZT takes longer to reach gelation than doped and co-doped samples.

After gelling, samples were dried in a muffle furnace (Heraeus) for 24 hours at 250 ºC to obtain xerogels.

3.2 CALCINATION AND SINTERING

Calcination was performed in a muffle furnace (Heraeus) in a non-controlled sintering atmosphere at 800 ºC, at a 5 ºC/minute heating rate for 5 hours, to promote the crystallization of xerogels. For this, samples were placed over a zirconia plate using an alumina plate as a base.

After calcination, samples were milled in ethanol for 96 hours in a 3D mixer (Turbula) using 5 mm zirconia beads as milling elements and maintaining a BPR (ball-to-powder ratio) of 5:1.

After homogenization, the calcinated powders were dried at 90 ºC for 4 hours using a heat plate.

Calcinated powders were prepared for sintering by uniaxial pressing. PVA (polyvinyl alcohol, Sigma Aldrich) 8 wt% solution was used as a binder agent. One drop of PVA solution to each 0.4 g was established as the ideal concentration. 125 MPa pressure was applied for 3 minutes to press the samples, and a 10.2 mm intern diameter hardened steel die was used as a mold for the pressing.

After pressing, samples were sintered in a non-controlled atmosphere using a programable furnace (Heraeus) to obtain dense samples and conduct sintering studies. Binder elimination was performed by heating the samples to 500 ºC at a 3 ºC/minute heating rate and carrying out one hour of soaking time. Sintering was performed by heating the samples at a 4 ºC/minute heating rate up to three different temperatures, 1250, 1350, and 1450 ºC, for 4 hours of soaking.

3.3 STRUCTURAL AND MICROSTRUCTURAL CHARACTERIZATIONS

After sintering, pellets had their surfaces made plane parallel by grinding them with SiC paper (Struers, 500 grit), followed by a final grinding step using a Jung (JF415-S) surface grinding machine to the thickness of 0.8 mm. To alleviate tensions caused by the grinding process, the samples were annealed at 500 ºC for 2 hours, carrying out a 2 ºC/minute heating rate. Cooling was carried out without rate control.

Structural characterization was performed by analyzing the diffraction patterns of calcinated and sintered samples obtained in reflection mode in a Bruker diffractometer (D8-Advance),

equipped with a copper target, step size of 0.02, scan step time of 1 s, voltage of 40 kV, current of 25 mA, and measuring range from 15 to 90º. Further structural analysis was performed by applying the Rietveld method to the diffraction patterns using the GSAS software package (Toby; Von Dreele, 2013) to refine structural parameters and line widths from the XRD patterns following the IUCr (McCusker *et al.*, 1999) recommendations. To perform the necessary calculations, the CIF number 230567 (Coondoo *et al.*, 2018) was used as the structural model for the samples, and a standard alumina sample was used to create the instrumental file responsible for accounting for the diffraction patterns' instrumental broadening. Chebyschev polynomials, seventh order, were used to fit the inelastic scattering background.

SEM imaging of selected sintered samples was performed using a JEOL JSM – IT500HR Emission Scanning Electron Microscope (SEM), and analysis of the images was performed using ImageJ (Version 1.54j) (Schneider; Rasband; Eliceiri, 2012).

Densification was calculated by weighting the samples before and after sintering and expressing the mass reduction percentage as a function of sintering temperature.

Density values for all sintered samples were calculated using the Archimedes method, using an analytical balance (Mettler Toledo AG204) and distilled water as the auxiliary liquid. Standard values for distilled water's density were used for the calculations considering its temperature at the moment of measurement. This thesis references these values (American Institute of Physics; Gray, 1972). Equation 14 was used for this purpose, where ρ_{sample} is the sample density, ρ_{water} is the water density for the correspondent temperature, $weight_{air}$, the sample weight outside the auxiliary liquid, and $weight_{water}$, the sample weight immersed in the auxiliary liquid.

$$\frac{\rho_{sample}}{\rho_{water}} = \frac{weight_{air}}{weight_{air} - weight_{water}} \quad (14)$$

3.4 DIELECTRIC, FERROELECTRIC, AND PIEZOELECTRIC CHARACTERIZATION

To perform dielectric, ferroelectric, and piezoelectric characterizations of the samples, metallic contacts were created by applying silver paint (G302-Leitsilber) to both sides of the sintered samples and letting them naturally dry for 1 hour.

Dielectric measurements were performed on sintered samples using an LCR meter (Keysight E4980AL) coupled with a programable furnace (Nabertherm LE 4/11/3216) to obtain permittivity (ε_r) and dissipation factor (tan δ) as a function of temperature, from room temperature to 200 ºC, at a 2 ºC/minute heating rate for frequencies from 10 to 1 MHz, performing measurements by decade.

$d_{33,}$ capacitance (C), and tan δ measurements were performed on sintered samples at room temperature using high precision, piezoelectric testing equipment PiezoMeter System PM300 (110 Hz and 10 N gripping force) after polarization in oil (Wacker Silicone Fluid AP 150), applying 3 kV/mm, for 30 minutes at room temperature.

Polarization loops and strain loops measurements (P-E and S-E) were performed at room temperature for sintered samples in an aixACCT (Systems GmbH, Germany) utilizing a TF analyzer 2000, a piezo sample holder unit for bulk ceramics, a TREK 2020C amplifier, applying a 3 KV/mm electric field and hysteresis frequencies of 16.6667 and 1.66667 Hz for 3 cycles, triangular waveform.

4 RESULTS AND DISCUSSION

In this section, the results from the experimental procedures performed are presented. It focuses on the analysis of the BCZT piezoceramic and the impacts of vanadium and cerium doping and co-doping in its sintering temperature, considering densification as a function of sintering temperature, and incidental impacts on structural, microstructural, dielectric, ferroelectric, and piezoelectric properties developed.

4. 1 STRUCTURAL AND MICROSTRUCTURAL ANALYSIS

X-ray diffraction analysis was able to determine that the heat treatment at 800 ºC was successful in promoting the crystallization of all samples, and no trace of an amorphous phase can be detected in any of the patterns considering the detection limit of the equipment, as it can be seen in Figure 10.

Through the XRD analysis, it is possible to confirm that the employed novel route effectively produces the desired Ce-BCZT, V-BCZT, and co-doped BCZT ceramics in the ferroelectric tetragonal phase. Considering the composition range studied, it is observed that the perovskite structure is maintained for doped and co-doped BCZT samples. No composition-induced phase transition can be observed. The ICSD (Inorganic Crystal Structure Database) (Fluck, 1996) CIF (Crystallographic Information File), collection code number 230567 (Coondoo *et al.*, 2018) was able to index all diffraction peaks to the tetragonal *P4mm* space group (space group number 99). A minor secondary phase can be observed in Ce-doped calcinated BCZT samples (BCZT-A and BCZT-C) at 24.3°. This peak can be attributed to titanium oxide, space group $P3_121$. The secondary phase can be indexed with the ICSD (Fluck, 1996) collection code number 1537224 (Lacks; Gordon, 1993), shown in Figure 10 a) as the fuchsia dashed line. The match between the peak position at 24.3 degrees and the most intense titanium oxide peak is evident.

Figure 10 – Calcinated samples XRD patterns

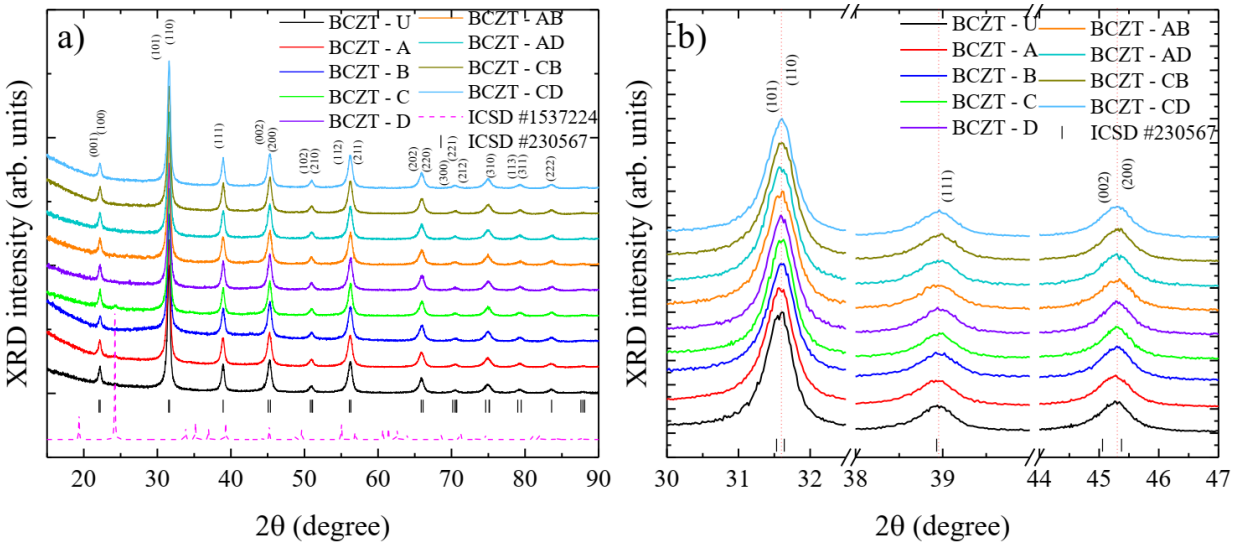

Source: Own authorship

Caption: a) XRD measurement from 15 to 90° and b) XRD measurement from 30 to 47° with breaks to showcase peak shifting.

Analyzing the diffraction patterns, it's clear that Ce and V doping cause the diffraction peaks to shift depending on concentration and, of course, the dopant itself. Its analysis shows Ce occupies distinct crystallographic sites in BCZT's structure depending on the concentration. Vanadium, however, occupies exclusively the B site. These shifts in the diffraction peaks corroborate the assessment that V and Ce enter the structure of BCZT to form a solid solution, altering its lattice parameters.

When present in low concentration (BCZT-C sample), Ce causes the diffraction peaks to shift to higher diffraction angles, which happens because the lattice parameters shorten as a result of the substitution of the bigger Ba^{2+} ion (ionic radius 1.60 Å) for the smaller Ce ion in the A site, as can be seen in Figure 10 b). On the other hand, diffraction peaks shift to lower angles when Ce concentration is higher (BCZT-A sample), which indicates cerium's occupation of the B site. This phenomenon is corroborated by findings confirming that the Ce ion can occupy both A and B crystallographic sites depending on cerium's oxidation state due to a change in ionic radius. The Ce^{3+} ion (ionic radius, 1.29 Å) occupies the A site as a donor dopant, and Ce^{4+} (ionic radius, 0.80 Å) the B site as an isovalent dopant. When Ce^{4+} substitutes either Ti^{4+} (ionic radius 0.605 Å) or Zr^{4+} (0.72 Å) atoms, lattice parameters expand, and peaks shift to lower diffraction angles (Cui *et al.*, 2012; Shannon; Prewitt, 1969).

For V-doped BCZT samples, increasing vanadium concentration causes the diffraction peaks to shift to higher diffraction angles due to the reduction of lattice parameters, as seen in Figure 10 b). In this case, the vanadium ion (either V^{4+}, 0.59 Å or V^{5+}, 0.54 Å) is substituting the bigger Ti^{4+} or Zr^{4+} ions, as has been reported elsewhere and is corroborated by this thesis (Shannon; Prewitt, 1969; Verma *et al.*, 2021).

Increasing doping concentration when co-doping is in play, from BCZT-CD to BCZT-AB, causes the diffraction peaks to continuously shift to higher angles, meaning a reduction of lattice parameters, which is consistent with the dopants' substitutions discussed. These shifts attest to their successful simultaneous introduction into BCZT's structure. However, a more in-depth structural investigation is needed to fully reveal how these ions occupy A and B sites when competing for the same site.

Further investigation into the diffraction patterns of the calcinated samples was performed using the Rietveld method, which results can be seen in Figure 11 and summarized in Table 5.

All refinements reached an excellent agreement between the experimental patterns and simulated values, as can be attested by how similar both patterns are, seen in Figure 11, and by the Rietveld discrepancy values in Table 5, which are within the acceptable range.

From the refinements, lattice parameters, unit cell volume, and tetragonality values were determined as a function of composition or doping content. These values further corroborate the successful introduction of both Ce and V into the structure of BCZT. Ce doping first

decreases unit cell volume for the BCZT-C composition and, for higher concentrations, increases it (BCZT-A) considering the undoped composition.

Figure 11 – Rietveld refinements of calcinated samples

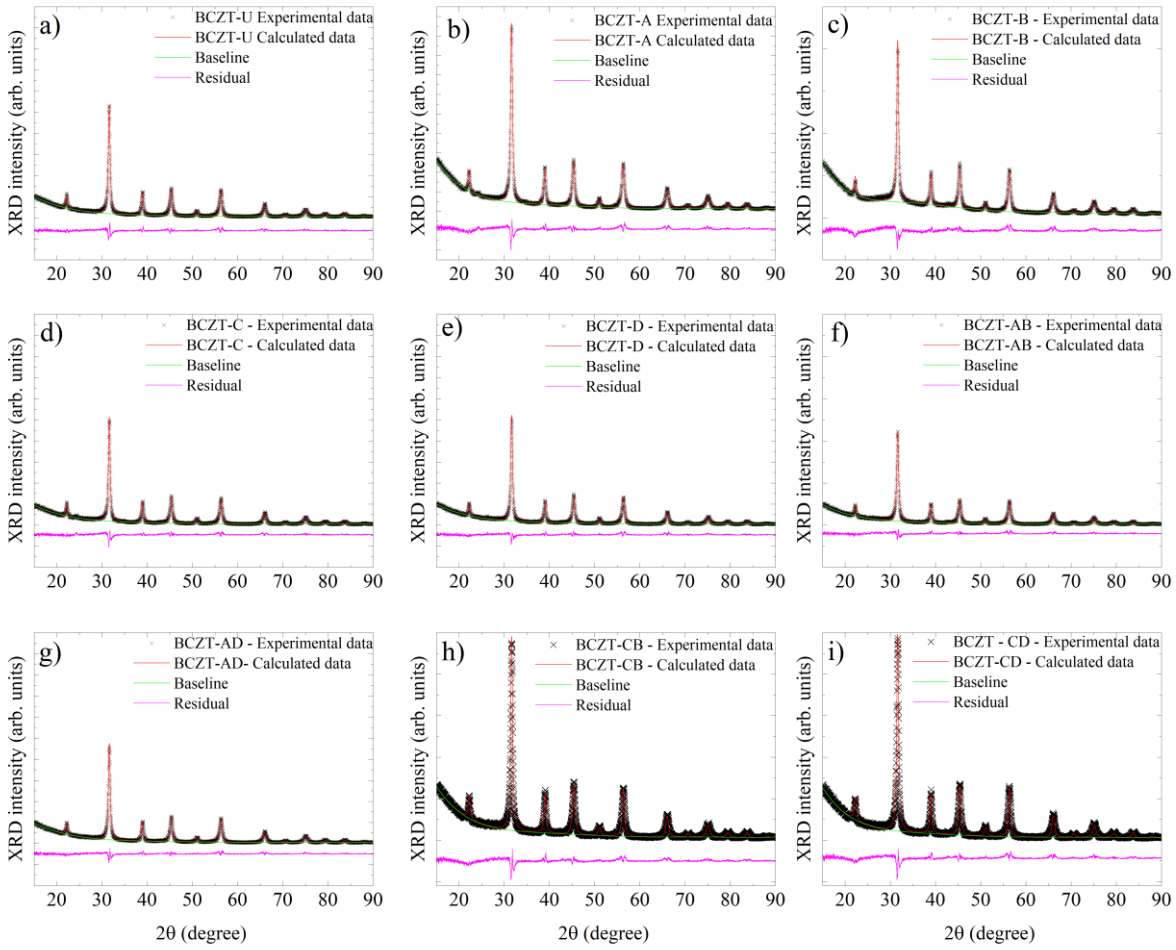

Source: Own authorship

Caption: a) BCZT-U sample refinement, b) BCZT-A sample refinement, c) BCZT-B sample refinement, d) BCZT-C sample refinement, e) BCZT-D sample refinement, f) BCZT-AB sample refinement, g) BCZT-AD samples refinement, h) BCZT-CB samples refinement, and i) BCZT-CD samples refinement.

Because Ce doping is carried out in low concentrations, its structural effects are subtle, and tetragonality values, for example, are quite similar to the one of the undoped sample, which is also corroborated by the technological properties measured, shown further in this thesis.

Table 5 – Lattice parameters and discrepancy values obtained from Rietveld refinement for calcinated samples

Sample	χ^2	R_{wp} (%)	R_p (%)	Lattice parameters
BCZT-U	1.958	11.71	8.66	a = b = 3.992287 (0.000326); c = 4.019372 (0.000491) volume = 64.062 (0.014) c/a = 1.0068
BCZT-A	3.086	9.89	7.52	a = b = 3.992695 (0.000333); c = 4.019515 (0.000508) volume = 64.078 (0.014) c/a = 1.0067
BCZT-C	2.131	12.54	9.41	a = b = 3.991076 (0.000351); c = 4.017221 (0.000551) volume = 63.989 (0.015) c/a = 1.0065
BCZT-B	3.240	9.48	7.42	a = b = 3.993230 (0.000429); c = 4.015145 (0.000715) volume = 64.025 (0.017) c/a = 1.0055
BCZT-D	2.082	12.19	8.88	a = b = 3.990091 (0.000347); c = 4.016041 (0.000543) volume = 63.939 (0.015) c/a = 1.0065
BCZT-AB	2.074	12.44	9.17	a = b = 3.991934 (0.000403); c = 4.018826 (0.000643) volume = 64.042 (0.017) c/a = 1.0067
BCZT-AD	1.840	11.72	8.69	a = b = 3.991104 (0.000355); c = 4.017467 (0.000562) volume = 63.994 (0.015) c/a = 1.0066
BCZT-CB	3.134	9.91	7.58	a = b = 3.991427 (0.000344); c = 4.016892 (0.000558) volume = 63.995 (0.014) c/a = 1.0064
BCZT-CD	3.291	10.39	7.84	a = b = 3.991643 (0.000329); c = 4.017990 (0.000502) volume = 64.019 (0.014) c/a = 1.0066

Source: Own authorship

Vanadium doping, as expected, causes more profound structural changes in BCZT, partly because it is carried out in higher concentrations. Tetragonality, for example, decreases compared to the undoped calcinated samples, BCZT-U, for both V-doped samples, BCZT-D and BCZT-B, accompanied by a reduction of unit cell volume. This is more pronounced in the high-content V-doped samples. Regarding the co-doped samples, due to the complex occupation of the A and B sites by the dopants, overall tetragonality values are quite similar to the undoped sample.

Analyzing the diffraction patterns to understand the impact of sintering temperature on the structural properties of the samples, it is possible to observe that its increase causes a correspondent sharpening of the diffraction peaks for all samples, while lattice parameters vary

depending on dopant concentration as it can be seen in Figure 12. The narrowing of the peaks indicates a correspondent reduction in strain and, most importantly, an increase in crystallite size, directly impacting technological properties (Cullity; Stock, 2014; Hassanzadeh-Tabrizi, 2023). This phenomenon is quite common and observed in ceramic and metallic materials overall.

Comparing Ce-doped BCZT sintered samples to the undoped ones, it is noticeable that with the increase of cerium concentration, diffraction peaks shift to smaller diffraction angles, contrasting to what happens to some calcinated samples, Figure 12 b). When samples are sintered, Ce occupies exclusively the B site in the structure of BCZT. This happens to all Ce-doped samples regardless of sintering temperature, except for the BCZT-A sample sintered at 1450 ºC. The increase in sintering temperature induces a different dynamic when Ce is introduced into the structure of BCZT.

When vanadium doping is considered, there is a constant peak shift to higher diffraction angles with the increase of vanadium concentration, the same observed in the calcinated samples caused by the substitution of Zr and Ti by vanadium in the B site decreasing lattice parameters, Figure 12 c) and d).

For the co-doped samples, there is a shift to higher diffraction angles in comparison to the one of the BCZT-U sample due to the introduction of the dopants into the lattice of BCZT, which means that they experiment reduction due to the introduction of smaller Ce and V atoms replacing the bigger Zr and Ti atoms, Figure 12 e) and f). This is consistent with the peak shifts presented by the V and Ce-doped BCZT samples that have already been discussed.

Figure 12 –XRD patterns of sintered samples

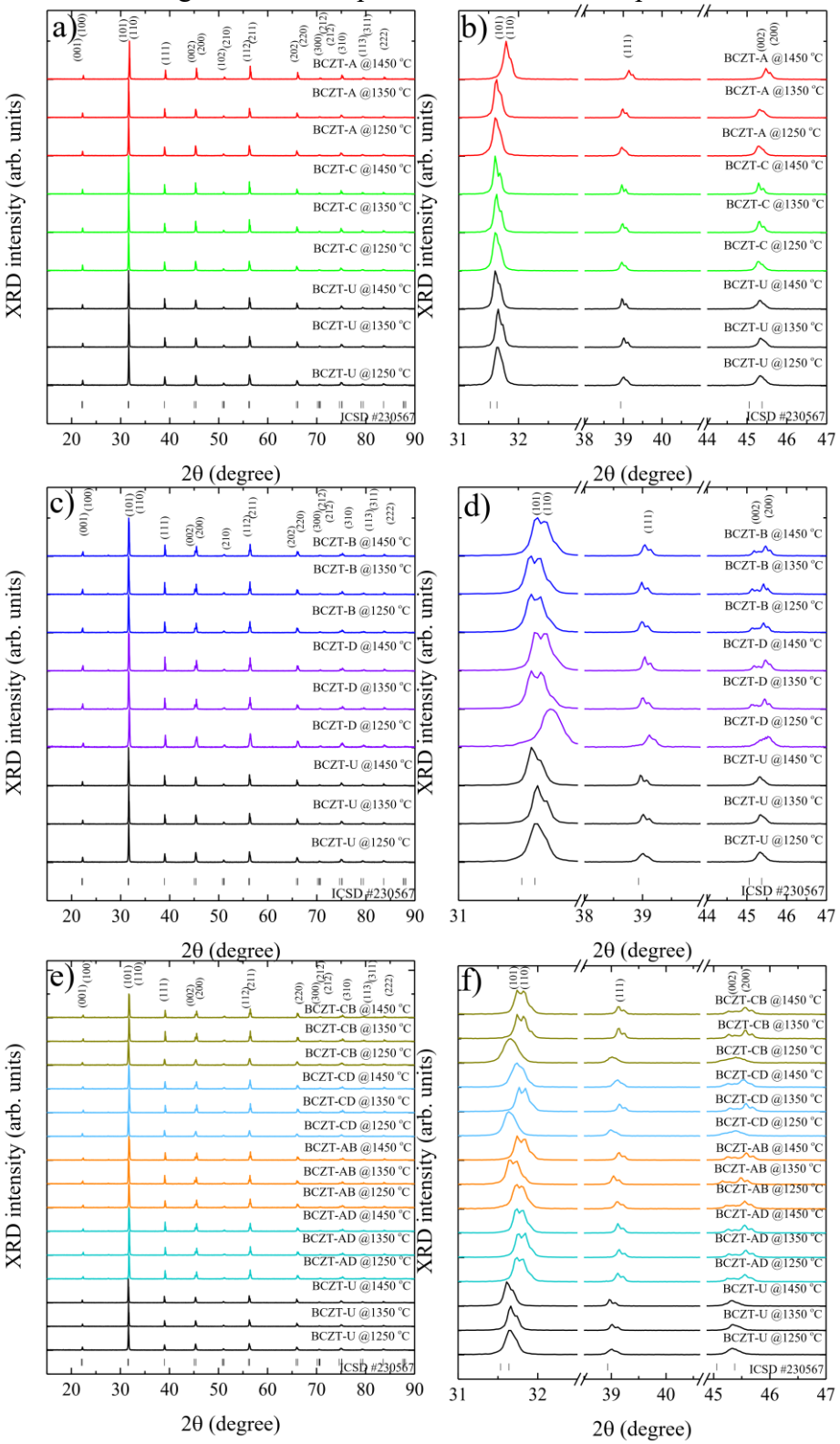

Source: Own authorship

Caption: a) XRD measurements of sintered Ce-doped BCZT samples from 15 to 90°, b) XRD measurements of sintered Ce-doped BCZT samples from 31 to 47° with breaks to showcase peak shifting, c) XRD measurements of sintered V-doped BCZT samples from 15 to 90°, d) XRD measurements of sintered V-doped BCZT samples from 31 to 47° with breaks to showcase peak shifting, e) XRD measurements of sintered co-doped BCZT samples from 15 to 90°, f) XRD measurements of sintered co-doped BCZT samples from 31 to 47° to showcase peak shifting.

Rietveld refinement was performed on sintered samples to conduct more in-depth structural investigations. Rietveld refinements were performed using the same parameters, and a structural model was used to refine the patterns of the calcinated samples. Figure 13 a) to i) shows the results of the refinements performed for the undoped and Ce-doped patterns of the samples. It's noticeable that the calculated patterns agree with the measured data.

Figure 13 – Rietveld refinement of Ce-doped and undoped samples

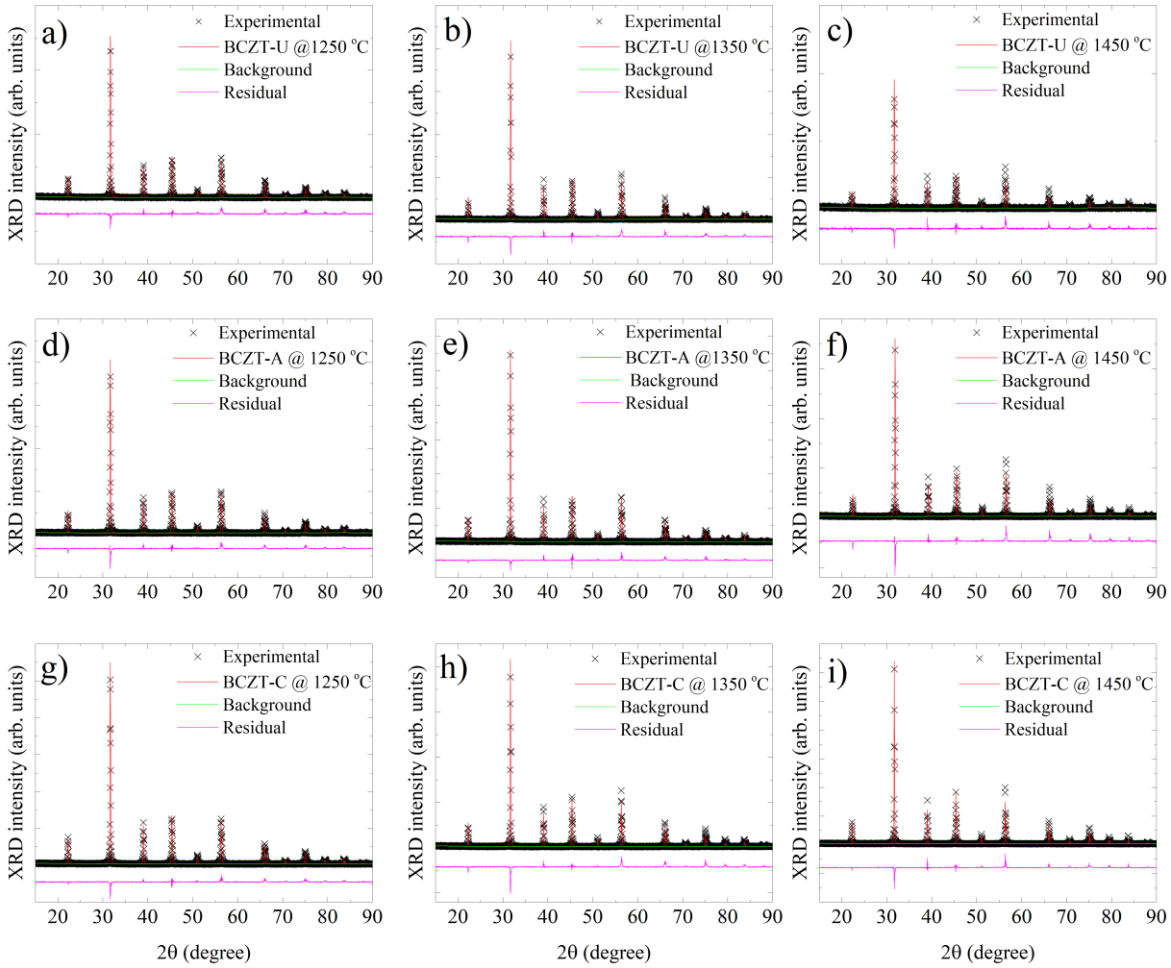

Source: Own authorship

Caption: a) Rietveld refinement of BCZT-U sample sintered at 1250 ºC, b) Rietveld refinement of BCZT-U sample sintered at 1350 ºC, a) Rietveld refinement of BCZT-U sample sintered at 1450 ºC, d) Rietveld refinement of BCZT-A sample sintered at 1250 ºC, e) Rietveld refinement of BCZT-A sample sintered at 1350 ºC, f) Rietveld refinement of BCZT-A sample sintered at 1450 ºC, g) Rietveld refinement of BCZT-C sample sintered at 1250 ºC, h) Rietveld refinement of BCZT-C sample sintered at 1350 ºC, and i) Rietveld refinement of BCZT-C sample sintered at 1450 ºC.

Vanadium-doped samples presented the same good agreement between experimental and calculated patterns, as seen in Figure 14 a) to f).

Figure 14 – Rietveld results for V-doped sintered samples

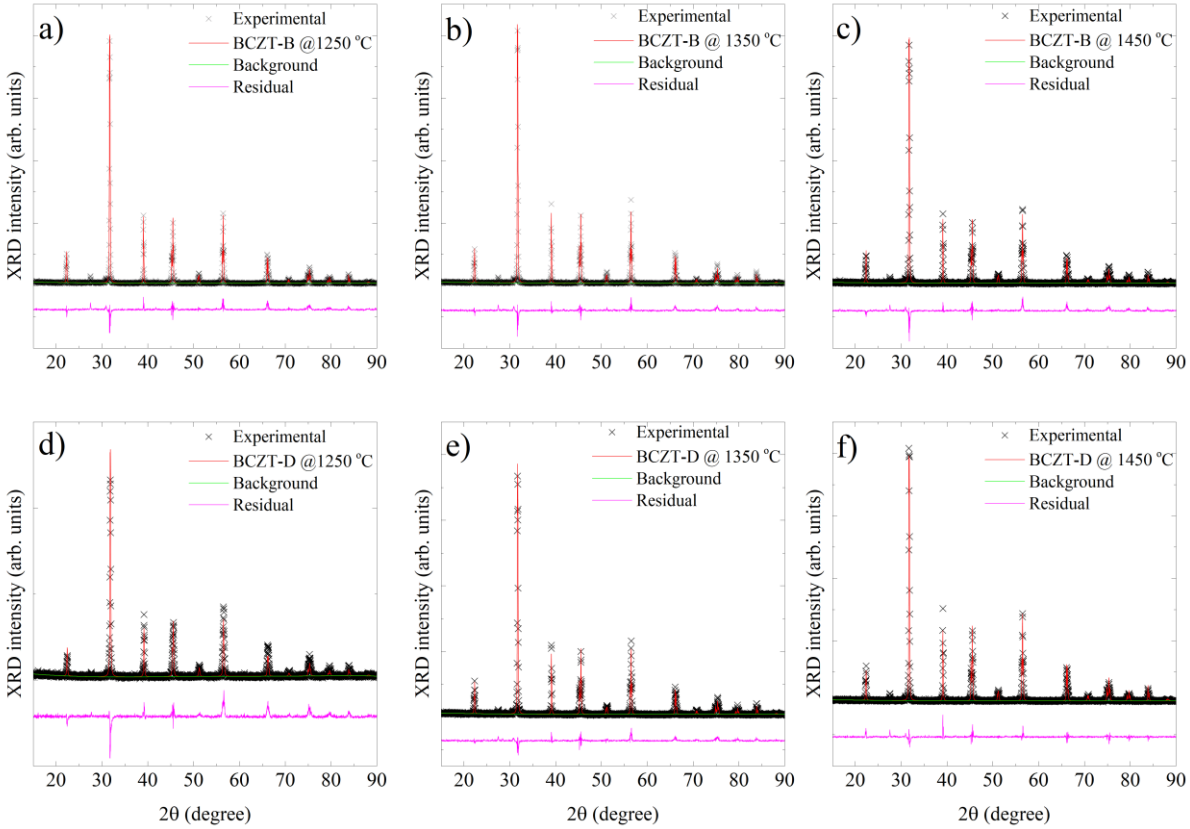

Source: own authorship

Caption: a) Rietveld refinement of BCZT-B sample sintered at 1250 ºC, b) Rietveld refinement of BCZT-B sample sintered at 1350 ºC, a) Rietveld refinement of BCZT-B sample sintered at 1450 ºC, d) Rietveld refinement of BCZT-D sample sintered at 1250 ºC, e) Rietveld refinement of BCZT-D sample sintered at 1350 ºC, f) Rietveld refinement of BCZT-D sample sintered at 1450 ºC.

A good fit can also be verified in co-doped sintered samples, as seen in Figure 15 and Figure 16 a) to f). In this case, it is important to stress that doping concentrations are small and that the XRD technique has limited sensitivity. However, it can still yield helpful information, such as lattice parameters and the presence of secondary and amorphous phases.

Figure 15 – Rietveld refinement results for low-vanadium co-doped samples

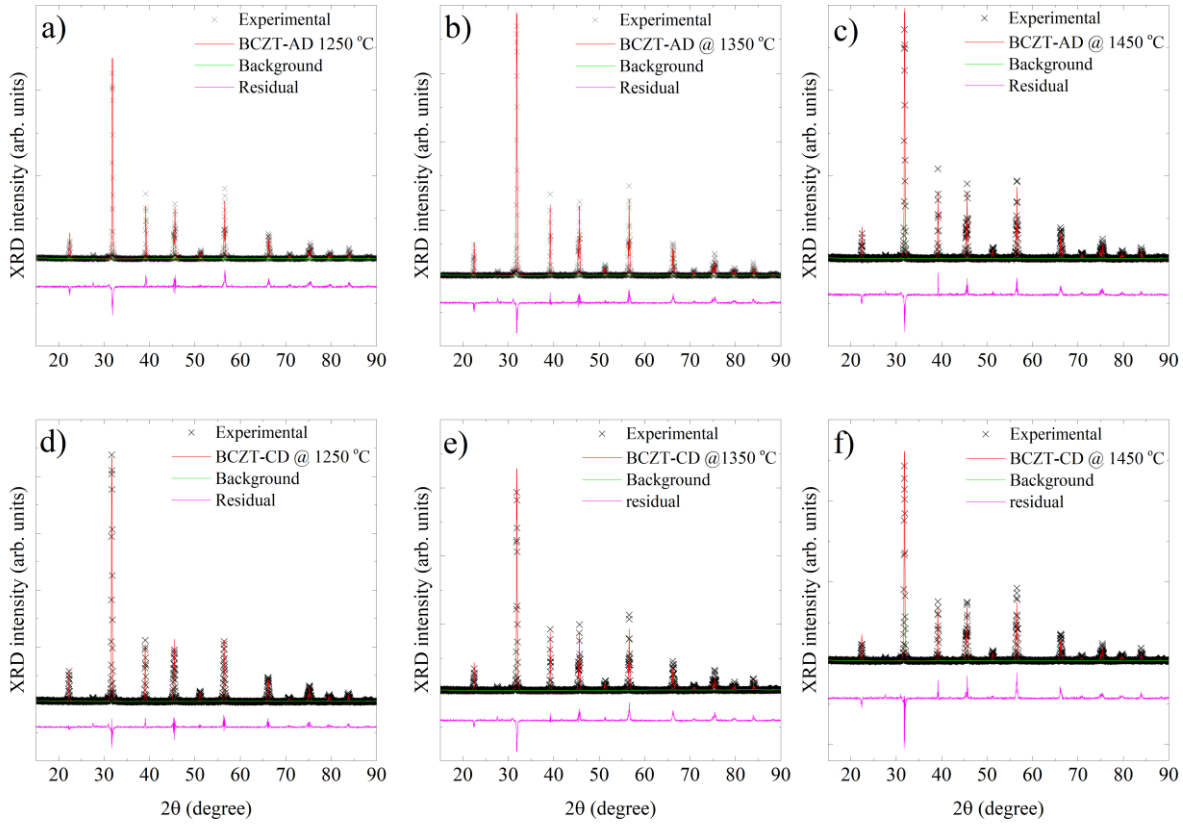

Source: own authorship

Caption: a) Rietveld refinement of BCZT-AD sample sintered at 1250 ºC, b) Rietveld refinement of BCZT- AD sample sintered at 1350 ºC, a) Rietveld refinement of BCZT- AD sample sintered at 1450 ºC, d) Rietveld refinement of BCZT-CD sample sintered at 1250 ºC, e) Rietveld refinement of BCZT- CD sample sintered at 1350 ºC, f) Rietveld refinement of BCZT- CD sample sintered at 1450 ºC.

Figure 16 – Rietveld refinement results for high-vanadium co-doped samples

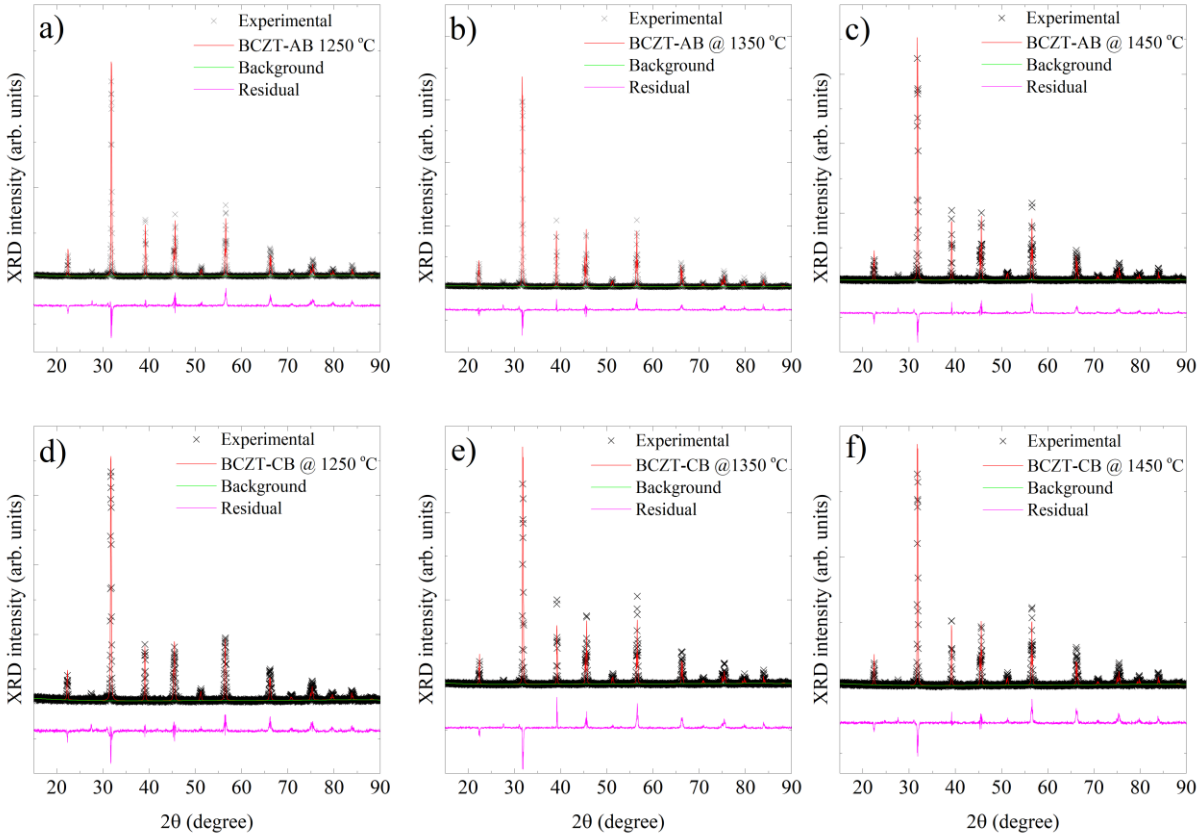

Source: own authorship

Caption: a) Rietveld refinement of BCZT-AB sample sintered at 1250 ºC, b) Rietveld refinement of BCZT- AB sample sintered at 1350 ºC, a) Rietveld refinement of BCZT-AB sample sintered at 1450 ºC, d) Rietveld refinement of BCZT-CB sample sintered at 1250 ºC, e) Rietveld refinement of BCZT-CB sample sintered at 1350 ºC, f) Rietveld refinement of BCZT-CB sample sintered at 1450 ºC.

The lattice parameters and discrepancy values obtained from the refinement performed can be summarized in Table 6. Similar to what was seen for calcinated samples, low values of χ^2 are obtained. However, atypical high values of R_{wp} and R_p are observed. This arises from a flaw in the structural model to represent the phase that is being fitted. Considering the success of the Rietveld refinement performed on the patterns of calcinated samples, it can be inferred that the model might be incomplete in describing all structural elements or instrumental features.

Nevertheless, it is possible to guarantee that the samples crystallize in the ferroelectric structure and that the introduction of the dopants is successful. Regarding lattice parameters, slight variation can be observed between the samples, which is to be expected considering the dopant concentration. The Rietveld refinement confirms the V occupation of the B site and the complex dopant occupation when co-doping is performed.

Table 6 – Lattice parameters and discrepancy values obtained from Rietveld refinement of sintered samples

(continues)

Sample	Sintering temperature (ºC)	χ^2	R_{wp} (%)	R_p (%)	Lattice parameters
BCZT-U	1250	1.674	19.28	15.17	a = b = 3.998147 (0.000177); c = 4.005210 (0.000259) volume = 64.024 (0.008) c/a = 1.00176
	1350	2.103	19.68	16.12	a = b = 4.000834 (0.000123); c = 3.995228 (0.000186) volume = 63.950 (0.006) c/a = 1.0014
	1450	1.482	30	23.82	a = b = 3.995238 (0.000247); c = 4.002859 (0.000341) volume = 63.893 (0.011) c/a =1.0019
BCZT-A	1250	1.772	17.18	14.01	a = b = 3.999778 (0.000133); c = 4.005583 (0.0002) volume = 64.082 (0.006) c/a = 1.0011
	1350	1.906	16.28	12.71	a = b = 3.996374 (0.000096); c = 4.002098 (0.00014) volume = 63.918 (0.004) c/a =1.0014
	1450	2.416	21.38	17.41	a = b = 3.996956 (0.000158); c = 4.001212 (0.000251) volume = 63.922 (0.007) c/a =1.001
BCZT-C	1250	1.756	15.46	12.22	a = b = 4.000879 (0.000105); c = 4.006641 (0.000156) volume = 64.134 (0.005) c/a = 1.0014
	1350	2.087	19.66	16.25	a = b = 3.999275 (0.00012); c = 4.003257 (0.000188) volume = 64.029 (0.005) c/a = 1.0014
	1450	2.067	17	13.61	a = b = 3.999866 (0.000177); c = 4.000220 (0.000337) volume = 63.999 (0.003) c/a ≈1
BCZT-B	1250	2.436	18.24	14.16	a = b = 3.987839 (0.000112); c = 4.010127 (0.000143) volume = 63.772 (0.005) c/a = 1.005
	1350	2.048	16.55	12.72	a = b = 3.987311 (0.000096); c = 4.010310 (0.000122) volume = 63.758 (0.004) c/a =1.0057
	1450	2.236	17.52	13.85	a = b = 3.987094 (0.000112); c = 4.009620 (0.000142) volume = 63.741 (0.005) c/a =1.005
BCZT-D	1250	2.162	24.8	20.33	a = b = 3.992003 (0.000312); c = 4.009486 (0.000421) volume = 63.896 (0.014) c/a = 1.004
	1350	1.842	16.25	12.68	a = b = 3.985212 (0.000103); c = 4.010404 (0.000128) volume = 63.693 (0.004) c/a =1.006

Table 6 – Lattice parameters and discrepancy values obtained from Rietveld refinement of calcinated samples

(conclusion)

	1450	1.833	15.19	11.42	a = b = 3.986969 (0.000077); c = 4.010375 (0.000099) volume = 63.749 (0.003) c/a =1.005
BCZT-AB	1250	2.415	21.65	17.63	a = b = 3.987322 (0.000183); c = 4.011381 (0.000231) volume = 63.776 (0.008) c/a = 1.006
	1350	2.035	18.19	14.22	a = b = 3.985756 (0.000115); c = 4.012161 (0.000141) volume = 63.738 (0.005) c/a = 1.006
	1450	2.465	19.76	15.86	a = b = 3.985440 (0.000127); c = 4.011856 (0.000157) volume = 63.723 (0.006) c/a = 1.006
BCZT-AD	1250	2.305	21.65	17.85	a = b = 3.987532 (0.000155); c = 4.010853 (0.000196) volume = 63.774 (0.007) c/a = 1.0058
	1350	2.280	17.99	14.48	a = b = 3.987315 (0.000109); c = 4.011115 (0.000137) volume = 63.771 (0.005) c/a = 1.0059
	1450	2.374	20.82	16.81	a = b = 3.987316 (0.000127); c = 4.010939 (0.000162) volume = 63.769 (0.006) c/a = 1.0059
BCZT-CB	1250	2.130	22.35	17.7	a = b = 3.989494 (0.000246); c = 4.008492 (0.000325) volume = 63.799 (0.011) c/a = 1.0047
	1350	2.884	23.73	19.91	a = b = 3.987165 (0.000153); c = 4.010954 (0.000191) volume = 63.764 (0.007) c/a = 1.0059
	1450	2.193	23.54	19.25	a = b = 3.987709 (0.000178); c = 4.010982 (0.000221) volume = 63.782 (0.008) c/a = 1.0058
BCZT-CD	1250	2.296	17.23	13.42	a = b = 3.992425 (0.000131); c = 4.008570 (0.000172) volume = 63.894 (0.006) c/a = 1.004
	1350	2.631	21.3	17.5	a = b = 3.987529 (0.000131); c = 4.010464 (0.000165) volume = 63.768 (0.006) c/a = 1.0057
	1450	2.720	22.12	17.78	a = b = 3.988000 (0.000187); c = 4.009525 (0.000242) volume = 63.768 (0.008) c/a = 1.0053

Source: Own authorship

Sintered samples had their apparent densification gauged by weighting them before and after sintering. This was expressed as mass loss percentage (densification) as a function of sintering temperature, shown in Figure 17. The mass loss due to the PVA is the first thing to be

considered. This value should be virtually the same for all samples since the burning of PVA occurs before the sintering truly begins, and this part of the process is identical for all samples. As the PVA addition was done with a pipette, it could be that the amount, in grams, was somewhat different for each sample.

Regardless, it is unlikely that the difference is significant enough to cause any real impact on these measurements. Additionally, through the XRD data, it can be attested that no secondary phase originates from the PVA addition. This is important because there is a noticeably wide dispersion range for the values obtained, making it hard to gauge detailed information from the data. This issue most likely arose from the limitations of the balance, considering the significant figures, which made the values disperse, as seen in Figure 17. Still, the densities of the samples were measured through Archimedes' method to determine the sintering temperature influence on densification so that this data can be analyzed in conjunction.

Nevertheless, it is clear from Figure 17 that samples present a trend regarding densification. From 1250 to 1350 ºC, samples lose more mass, which is expected. However, the apparent reduction in densification at 1450 ºC demands to be analyzed considering the density values, for volatilization can account for this phenomenon, thermally induced when the sintering temperature reaches a critical point. However, extrinsic factors can also contribute. The densification when the sintering temperature is raised from 1350 to 1450 ºC is not as acute as the one from 1250 to 1350 ºC, which makes the absence of significant figures more important.

Figure 17 – Densification of sintered samples

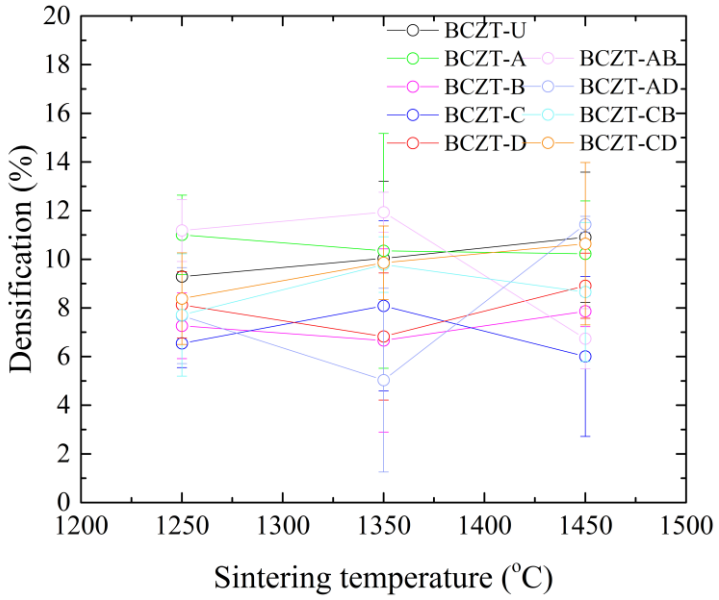

Source: Own authorship.

Density is a crucial property for piezoceramics, which directly impacts overall performance. To ensure adequate densification was achieved and incidentally gather additional information about microstructural characteristics, density values were calculated for all compositions and presented as a function of sintering temperature, presented in Figure 18.

Comparing density values for doped and co-doped BCZT with undoped BCZT ceramics, it is noticeable that BCZT-U density varies almost linearly with sintering temperature. Doping, however, alters this behavior according to concentration and dopants present. The theoretical density of BCZT-U is 5.772 g/cm^3. Sintering at 1450 ºC yields samples with 98.04% relative density, which is adequate considering the sintering method adopted and consistent with values found in published scientific literature (Chandrakala *et al.*, 2016; Coondoo *et al.*, 2018).

As Ce-doping is carried out in small concentrations, density values of Ce-doped samples are very similar to the ones of BCZT-U throughout the sintering temperature range, similar to the form in which density varies as a function of sintering temperature, as seen in Figure 18 a).

Vanadium doping, however, is carried out at higher concentrations, so density values of V-doped BCZT and co-doped BCZT samples are more affected, as seen in Figure 18, b) and c). For high vanadium concentration samples, density stays almost unchanged for the sintering temperature range studied, which means that full densification can be achieved at a lower sintering temperature. This phenomenon is even more poignant at the lowest sintering temperature investigated, 1250 ºC. High-concentration V co-doped samples present a considerably smaller gain in density when the sintering temperature is increased from 1250 to 1350 ºC, a range in which density gain is critical for undoped BCZT and Ce-doped BCZT samples. The reduction in density observed for co-doped samples when the sintering temperature is increased has already been observed in Ce-doped samples (Bijalwan *et al.*, 2019b). A similar phenomenon can be seen when co-doping is in play, especially when sintering increases from 1350 to 1450 ºC.

Figure 18 – Density values of sintered samples

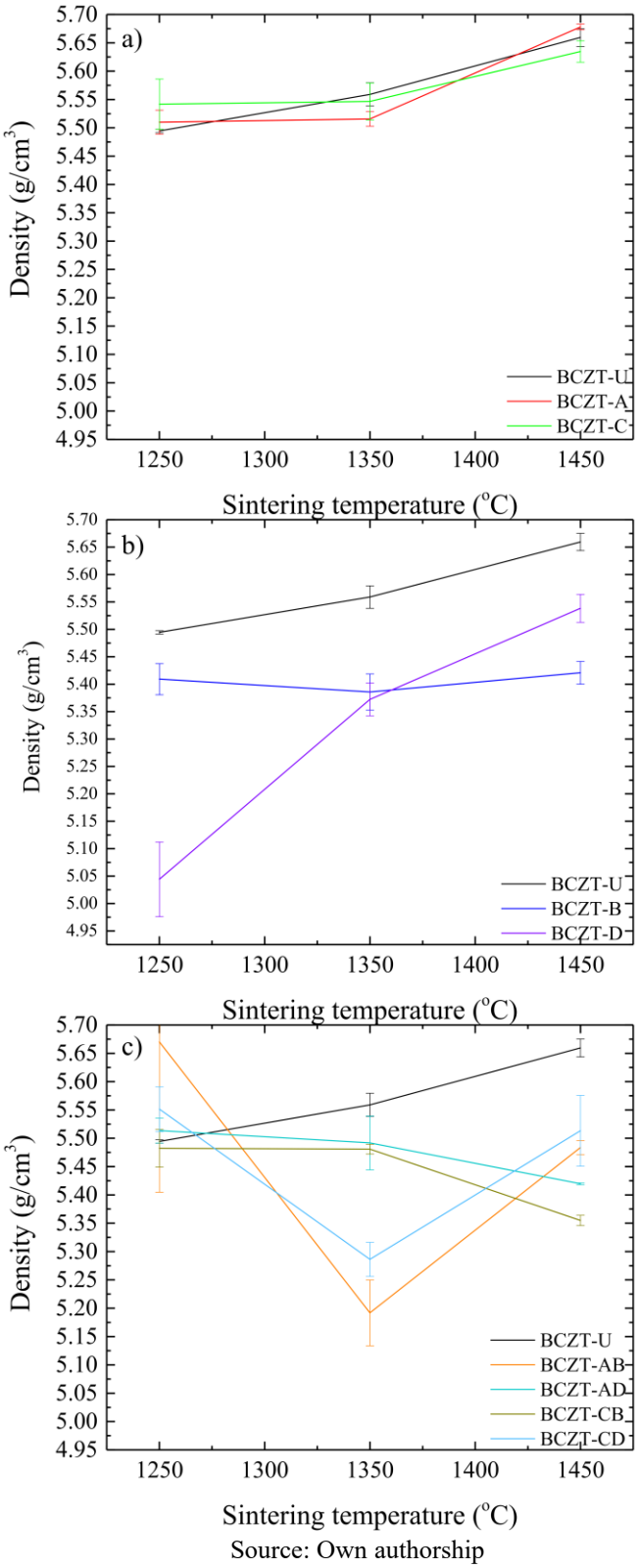

Source: Own authorship

Caption: a) Density as a function of sintering temperature for undoped samples and Ce-doped samples, b) Density as a function of sintering temperature for undoped samples and V-doped samples, and c) Density as a function of sintering temperature for undoped samples and co-doped samples.

SEM imaging, shown in Figure 19 and Figure 20, reveals details of the microstructures developed by V and Ce-doping and the effects of different sintering temperatures.

Figure 19 – SEM images of undoped and Ce-doped BCZT samples

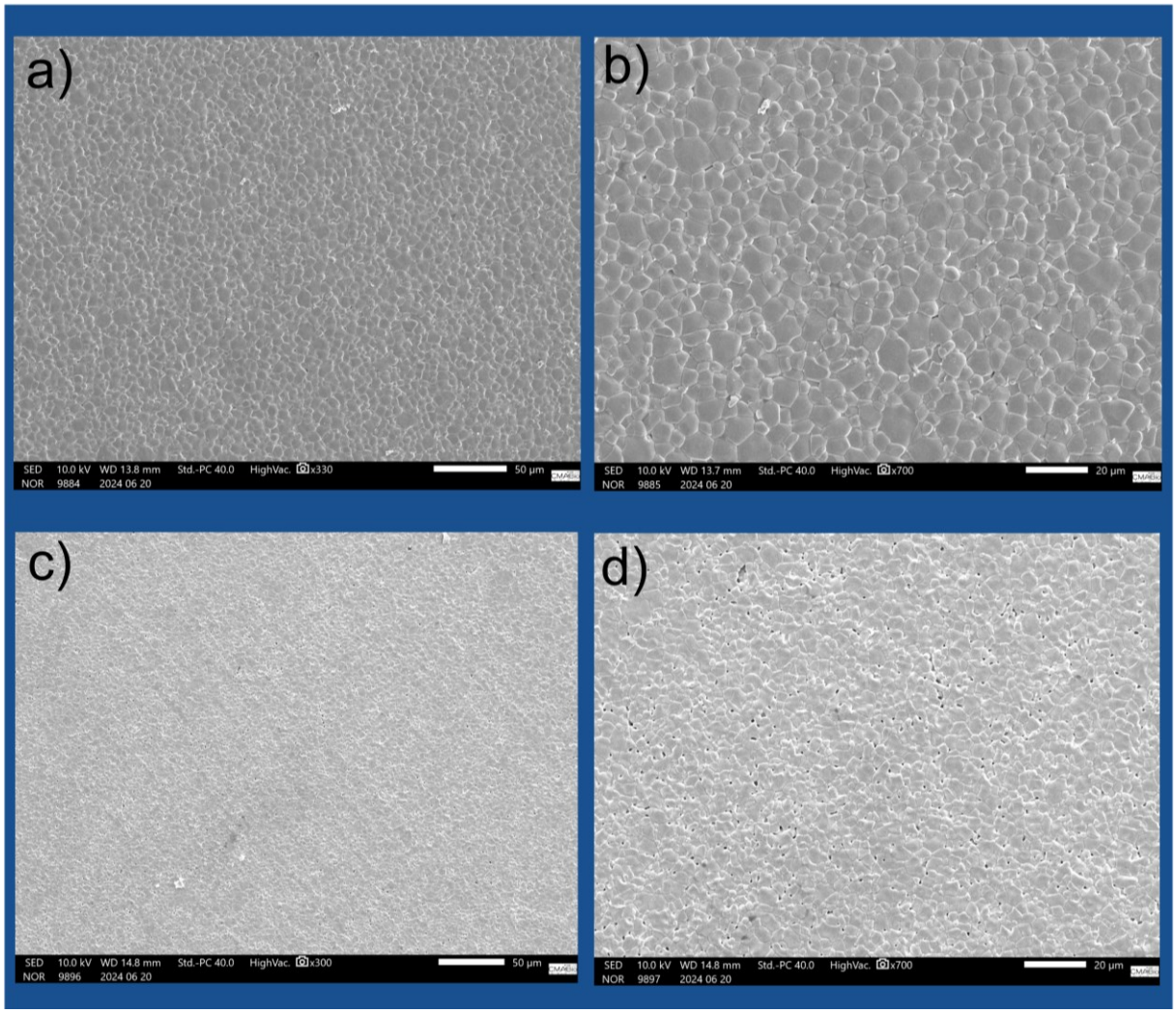

Source: Own authorship

Caption: a) SEM image of the surface of BCZT-U sample sintered at 1450 ºC (scale bar of 50 µm), b) BCZT-U, magnified (scale bar of 20 µm), c) SEM image of the surface of BCZT-A sample sintered at 1350 ºC (scale bar of 50 µm), d) BCZT-A, magnified (scale bar of 20 µm).

SEM micrographs help elucidate the reasons behind the poor performance of Ce-doped samples compared to undoped BCZT, as shown in Figure 19 c) and d). In Figure 19 c) and d), small grains and increased porosity are evident, with a measured 4.63 µm mean grain size (SD = 1.72) when compared to BCZT-U, Figure 19 a) and b), presenting grain size of 7.6 µm (SD = 2.6). On the other hand, co-doped BCZT samples, even at low temperatures, present coarser grains of 10.05 µm (SD = 3.4), as seen in Figure 20 c) and d). This is prompted by V-doping as seen by the micrographs of V-doped samples, Figure 20 a) and b), which showed a mean grain

size of 25.16 µm (SD=15.6). Another critical feature is grain size distribution. V-doped samples present a very large distribution, confirmed by the SD (standard deviation) values. This can be controlled through processing to promote a more uniform microstructure, potentially improving piezoelectric response. On the other hand, the bigger grains, compared to the BCZT-U sample, allow for a better performance overall. Significant porosity in Ce-doped samples, however, is a defect and pores act as pining points for the movement of domains hindering piezoelectricity which is one of the reasons for the poorer piezoelectric performance of these samples.

Figure 20 – SEM images of V-doped and co-doped BCZT samples

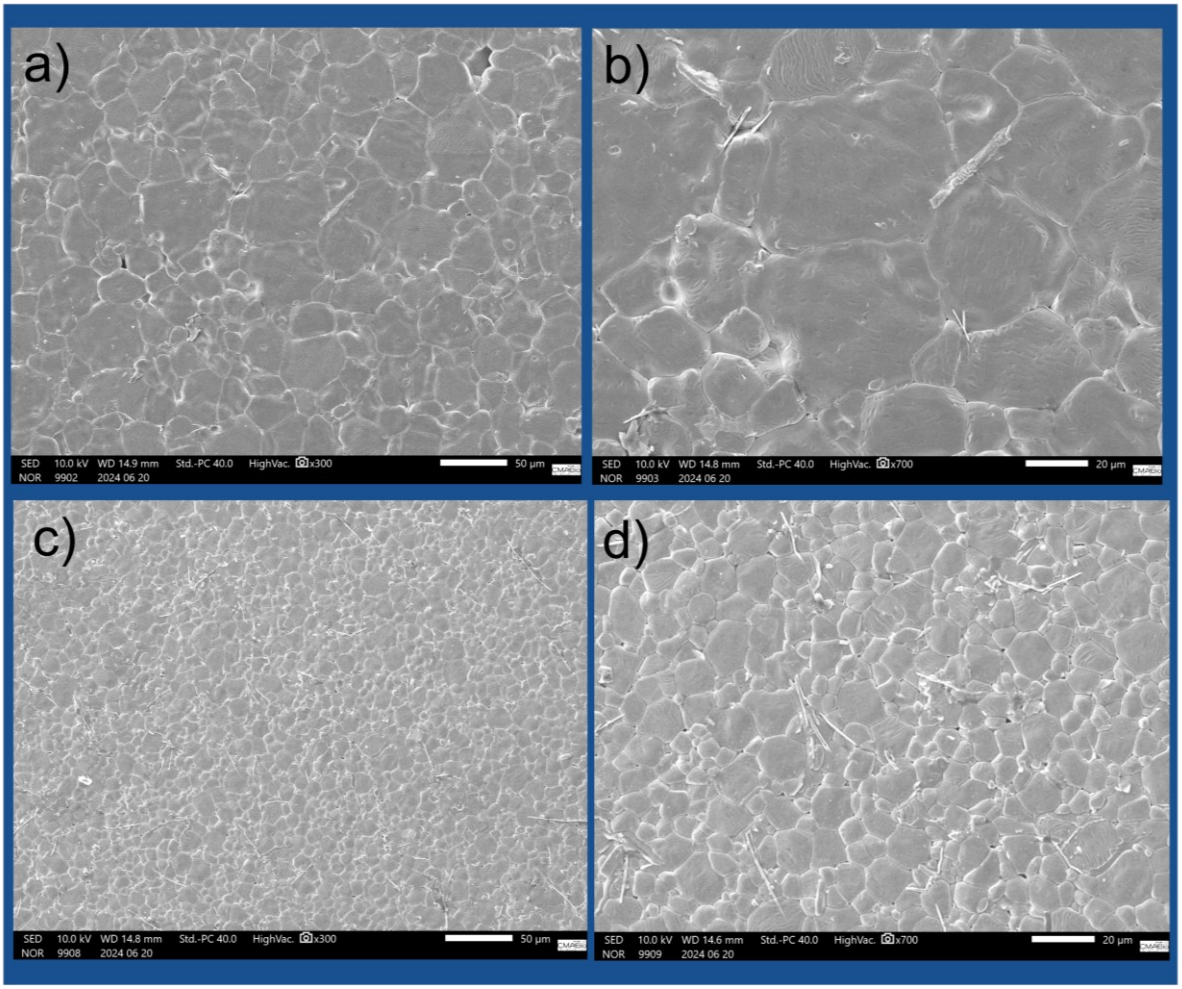

Source: Own authorship

Caption: a) SEM image of the surface of BCZT-D sample sintered at 1450 ºC (scale bar of 50 µm), b) BCZT-D, magnified (scale bar of 20 µm), c) SEM image of the surface of BCZT-AB sample sintered at 1350 ºC (scale bar of 50 µm), d) BCZT-AB, magnified (scale bar of 20 µm).

4.2 DIELECTRIC, FERROELECTRIC AND PIEZOELECTRIC ANALYSIS

The impact of structural changes induced by Ce and V doping can be observed in the functional properties measured.

These changes can be seen in the d_{33} values of polarized samples, shown in Figure 21. In the composition range studied, cerium addition is deleterious to the piezoelectric properties of BCZT, Figure 21 a), while capacitance remains almost unchanged, Figure 21 b). As expected, both properties improve with the increase in sintering temperature. This behavior is consistent with the density values obtained, and it is known that densification and larger grains greater than 30 μm improve permittivity and piezoelectric performance in BCZT (Bijalwan *et al.*, 2019b). The d_{33} values obtained for all samples are inferior to those usually developed, as seen in the work of Liu and Ren and Table 2 (Liu; Ren, 2009). This is understandable when it is considered that microstructure plays a critical role in piezoelectric properties, as confirmed by SEM imaging. Another important point is the polarization process, which must be optimized to obtain the best piezoelectric response possible.

On the other hand, vanadium doping, Figure 21 c) and d) has a more varied impact on the piezoelectrics properties of BCZT compared to the Ce-doped samples. V-doped BCZT samples perform better, especially when subjected to low sintering temperatures, such as 1250 ºC. When sintered at 1350 ºC, the BCZT-D sample shows the most significant increase in d_{33} amongst all samples, potentially due to the link between grain size and sintering temperature. V can be seen as the causing agent for this improved performance at lower temperatures, as all co-doped samples also outperform undoped and Ce-doped samples when sintered at 1250 ºC, as do BCZT-AB and BCZT-CB when sintered at 1350 ºC, both high vanadium concentration samples. When increasing the sintering temperature to 1450 ºC, BCZT-D presents slightly better piezoelectric performance than undoped BCZT. Vanadium presents a deleterious impact on capacitance for the whole V doping range, as seen in Figure 21 d), except for the BCZT-B composition sintered at the lowest sintering temperature, which is consistent with d_{33} coefficient values obtained.

For the co-doped samples, Figure 21 e), it is apparent that vanadium addition is responsible for better piezoelectric performance in the composition range investigated. All co-doped samples outperform the undoped sample when sintered at the lowest sintering temperature investigated, 1250 ºC. When increasing the sintering temperature to 1350 ºC, vanadium-rich samples BCZT-AB and BCZT-CB outperform undoped samples as well. For the highest sintering temperature carried out, however, there is a degradation of piezoelectric properties of co-doped samples that are potentially related to a decrease in density in higher

sintering temperatures, which was previously mentioned. Capacitance, however, suffers a significant reduction considering all co-doped samples when sintering is carried out above the critical temperature of 1350 ºC, Figure 21 f), another effect of vanadium doping.

Figure 21 – d_{33} and capacitance values as a function of sintering temperature

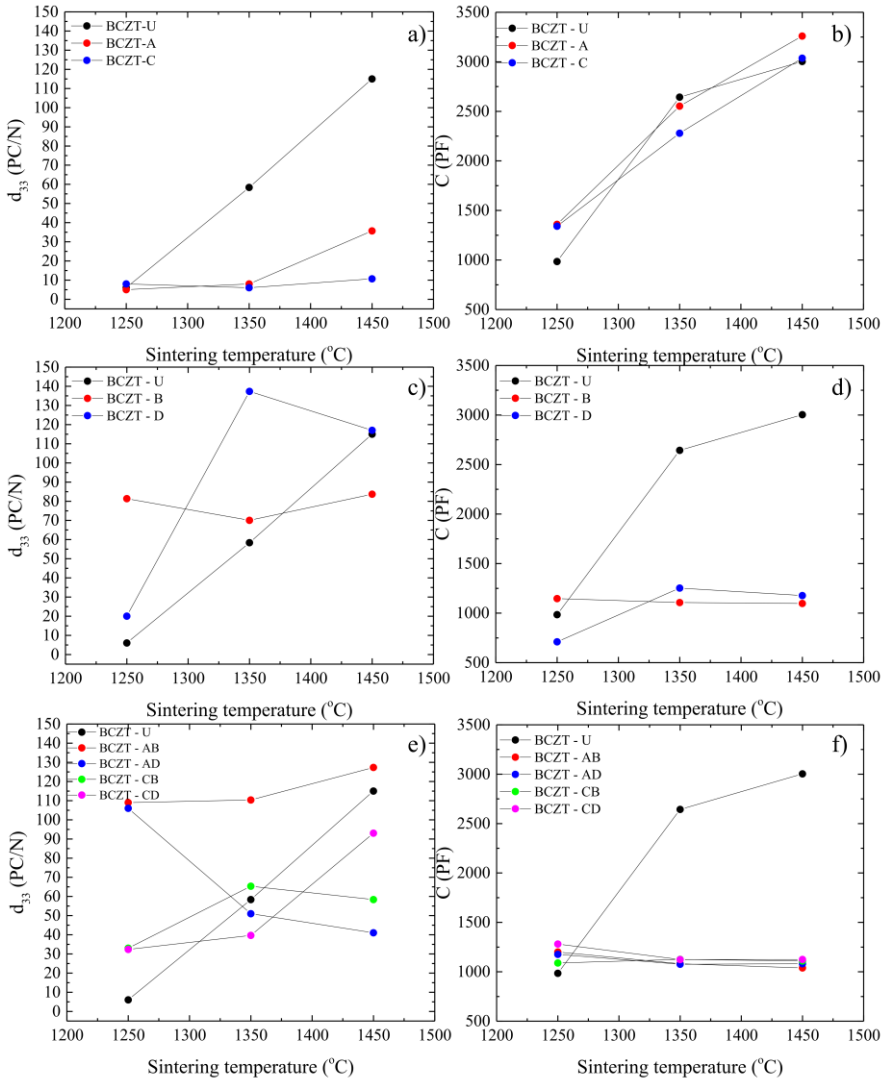

Source: Own authorship

Caption: a) Undoped and Ce-doped d_{33} values as a function of sintering temperature, b) Undoped and Ce-doped capacitance values as a function of sintering temperature, c) Undoped and V-doped d_{33} values as a function of sintering temperature, d) Undoped and V-doped capacitance values as a function of sintering temperature, e) Undoped and co-doped d_{33} values as a function of sintering temperature, and f) Undoped and co-doped capacitance values as function of sintering temperature

The positive impact of vanadium doping can be further attested by in situ dielectric measurements as a function of temperature, shown in Figure 22, for the frequency of 1 kHz. With the increase of sintering temperature from 1250 to 1350 ºC, all samples experiment an increase in dielectric permittivity. One key aspect, however, is that high-concentration V-doped

samples present more stable values, so the increase, although it happens, is more subtle, Figure 22 a), c), and e).

Densification and microstructural thermally activated modifications linked to adequate grain and domain size are most likely the cause for this overall increase in dielectric permittivity values. Additionally, it explains why V-doped samples do not present such a significant increase in dielectric permittivity in the same temperature range as the Ce-doped and BCZT-U samples. Their density values are stable for the temperature range studied. Increasing the sintering temperature further makes this phenomenon even more poignant, for the dielectric permittivity of Ce-doped and undoped BCZT samples increased, accompanied by densification. However, the density of V-doped samples had already reached a maximum when sintered at 1250 ºC. Consequently, dielectric permittivity does not increase or is less significant because there is no further densification, and possibly increased grain size does not seem to have a positive impact here. When vanadium-doped samples are considered, there is no advantage in increasing the sintering temperature to 1450 ºC.

Sintering at 1350 ºC guarantees adequate dielectric loss values for all samples in the composition range studied, Figure 22 b), d), and f). Sintering at 1250 ºC is not as efficient for all samples. However, most samples present losses inferior to one of the BCZT-U samples except for the BCZT-A and BCZT-CB samples, which leads to the conclusion that, overall, vanadium and cerium co-doping of BCZT is beneficial to lower dielectric losses and that samples present adequate losses even at the lowest sintering temperature. Increasing the sintering temperature to 1450 ºC does not help reduce dielectric loss values further. It is also worth noticing that dissipation does not vary considerably with the increase in sintering temperature.

Another remarkable finding is that vanadium is responsible for considerably increasing Curie temperature. It is noticeable that V-doped samples present higher Curie temperatures than undoped BCZT or Ce-doped BCZT, considering the sintering temperature range studied. Curie temperature is vastly improved when V is added to BCZT, going from 71 to almost 120 ºC for the BCZT-AB and BCZT-AD samples, even when the sintering temperature is extremely low, 1250 ºC. Although Curie temperature is improved substantially by vanadium doping, room temperature values of permittivity are not. When vanadium and cerium are inserted into BCZT's structure, room temperature ε_r values suffer a significant reduction compared to the undoped samples. Depending on the sintering temperature, undoped samples can reach up to 6500 permittivity values at room temperature. In contrast, vanadium-doped and co-doped samples

reach a maximum of approximately 2000, which is a substantial reduction and may be related to the non-uniform microstructure observed by SEM imaging, but mostly, because the T_C is close to room temperature for the BCZT-U sample, which is directly related to unusually high permittivity values observed.

Figure 22 – In situ measurements of dielectric permittivity and dissipation factor of sintered samples at 1 kHz frequency

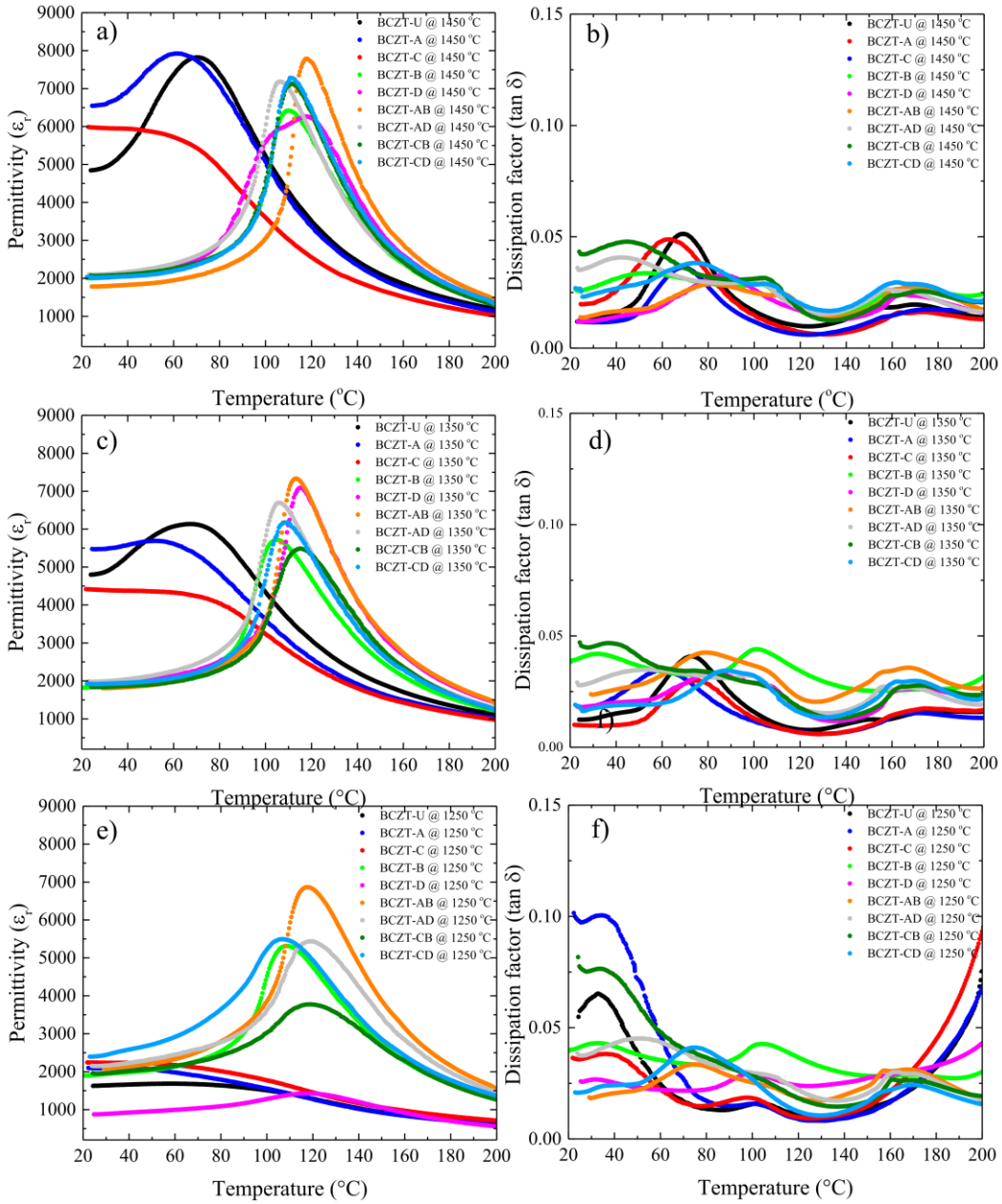

Source: Own authorship

Caption: In situ measurements of dielectric permittivity of samples sintered at a) 1450 ºC, c) 1350 ºC, and f) 1250 ºC. Dissipation factor measurements of samples sintered at b) 1450 ºC, d) 1350 ºC, and f) 1250 ºC, as a function of temperature at 1 kHz frequency.

To determine the effects of frequency on permittivity and dissipation, the measurements of these properties were also performed for a range of frequencies: 100, 1 k, 10 k, 100 k, and 1 MHz. The results for all sintered samples can be seen in Figure 23, Figure 24, Figure 25, Figure 26, Figure 27, Figure 28, Figure 29, Figure 30, and Figure 31.

Figure 23 – BCZT-U in situ permittivity and tan δ measurements as a function of temperature for several frequencies

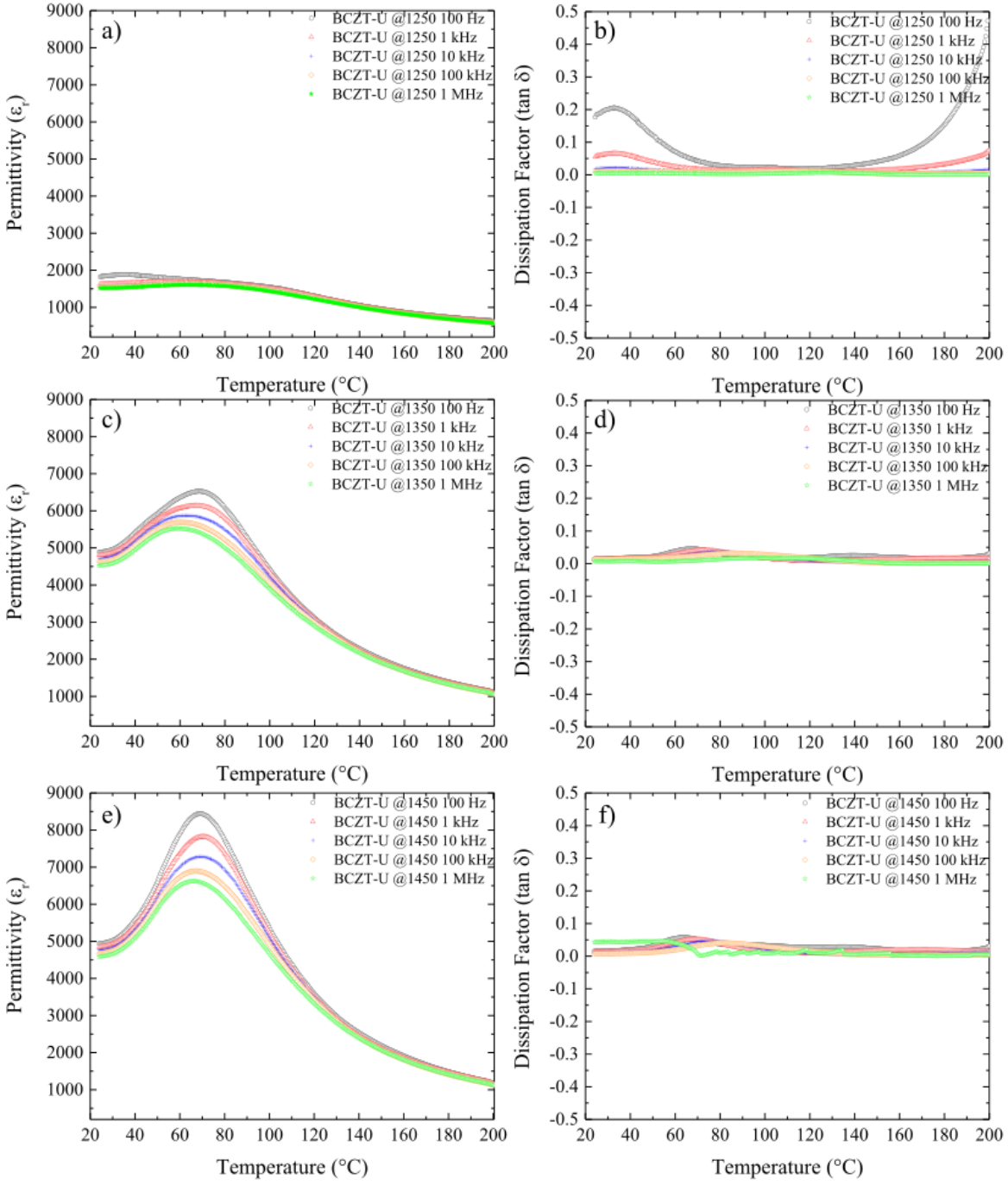

Source: Own authorship

Caption: ε_r and tan δ values as a function of temperature a) ε_r at 1250 ºC, b) respective Tan δ measurements, c) ε_r at 1350 ºC, d) respective Tan δ measurements, e) ε_r at 1450 ºC, and f) respective Tan δ measurements.

As expected, samples present classical ferroelectric behavior with little dispersion of the maximum permittivity value point as a function of frequency. The variation of permittivity as a function of frequency is expected since it is based on a frequency-dependent phenomenon, polarization. Dielectric losses, not only for the BCZT-U sample, are remarkably low, and little variation caused by frequency can be observed. For cerium-doped samples, refer to Figure 24 and Figure 26, dielectric behavior is quite similar to undoped BCZT regarding T_C and the dispersion of the point of maximum permittivity as a function of temperature and frequency.

Figure 24 – BCZT-A in situ permittivity and tan δ measurements as a function of temperature for several frequencies

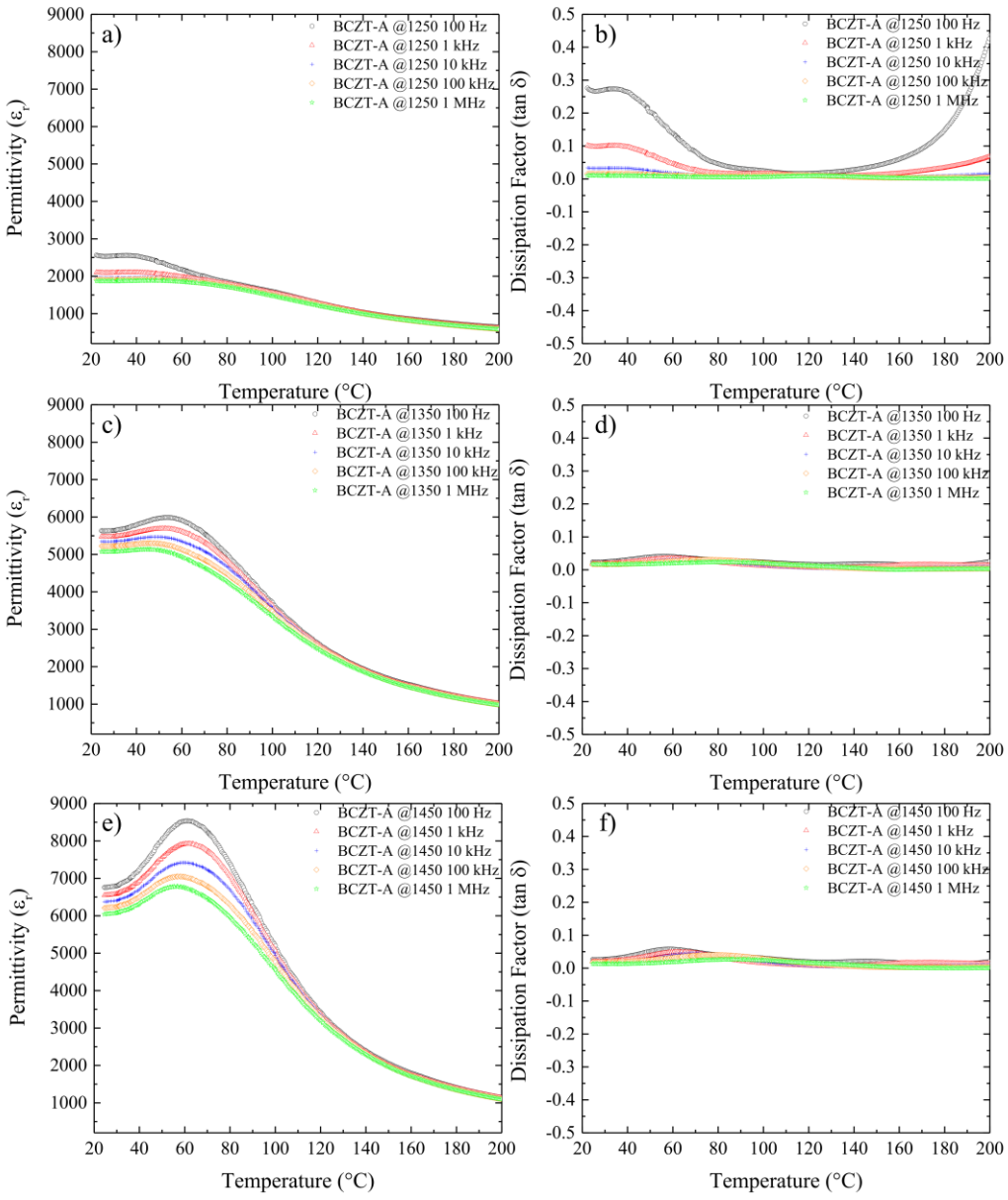

Source: Own authorship

Caption: ε_r and tan δ values as a function of temperature a) ε_r at 1250 ºC, b) respective Tan δ measurements, c) ε_r at 1350 ºC, d) respective Tan δ measurements, e) ε_r at 1450 ºC, and f) respective Tan δ measurements.

There is also little evidence of a relaxor behavior for vanadium-doped samples, Figure 25 and Figure 27.

Figure 25 – BCZT-B in situ permittivity and tan δ measurements as a function of temperature for several frequencies

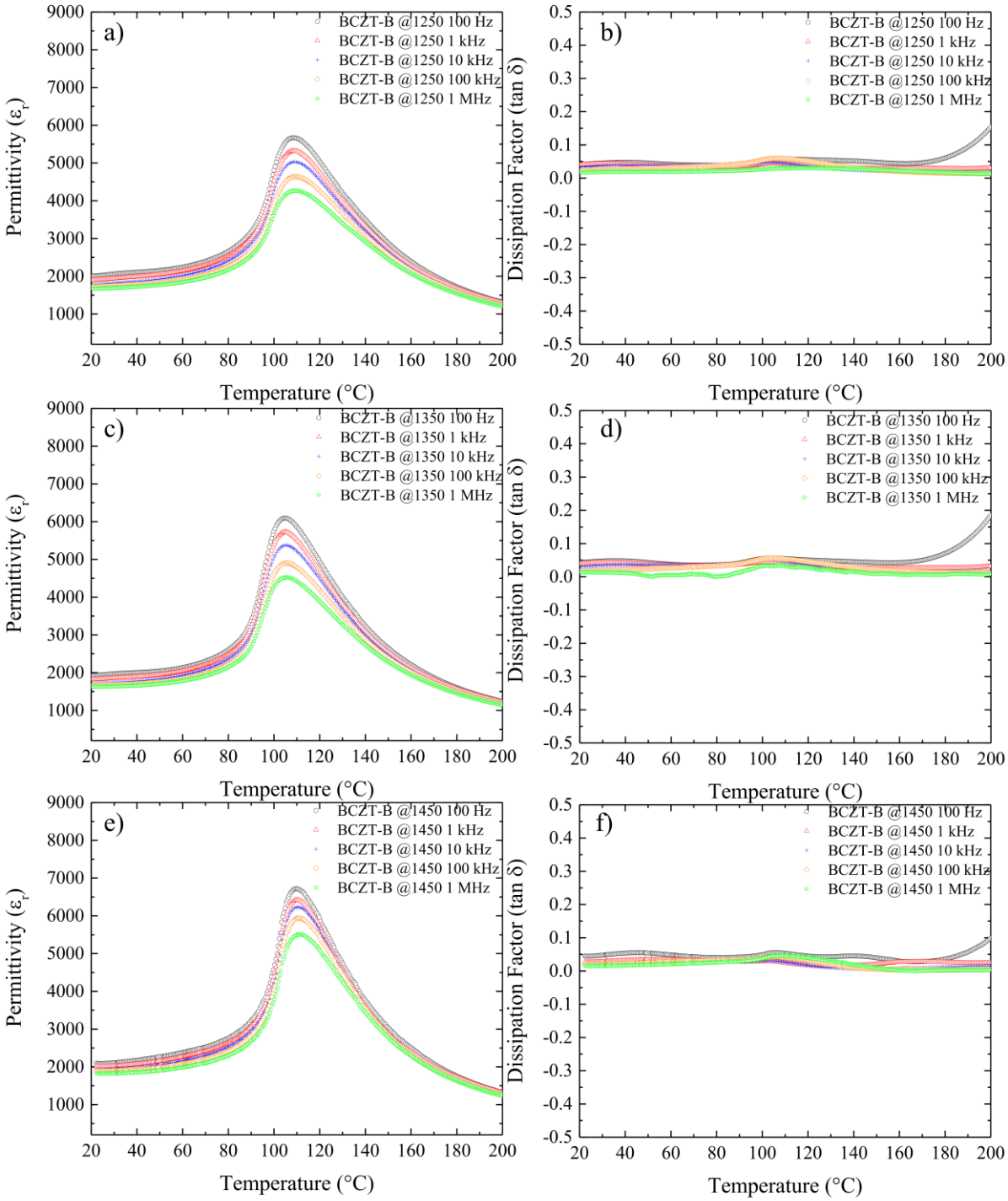

Source: Own authorship

Caption: ε_r and tan δ values as a function of temperature a) ε_r at 1250 ºC, b) respective Tan δ measurements, c) ε_r at 1350 ºC, d) respective Tan δ measurements, e) ε_r at 1450 ºC, and f) respective Tan δ measurements.

Figure 26 – BCZT-C in situ permittivity and tan δ measurements as a function of temperature for several frequencies

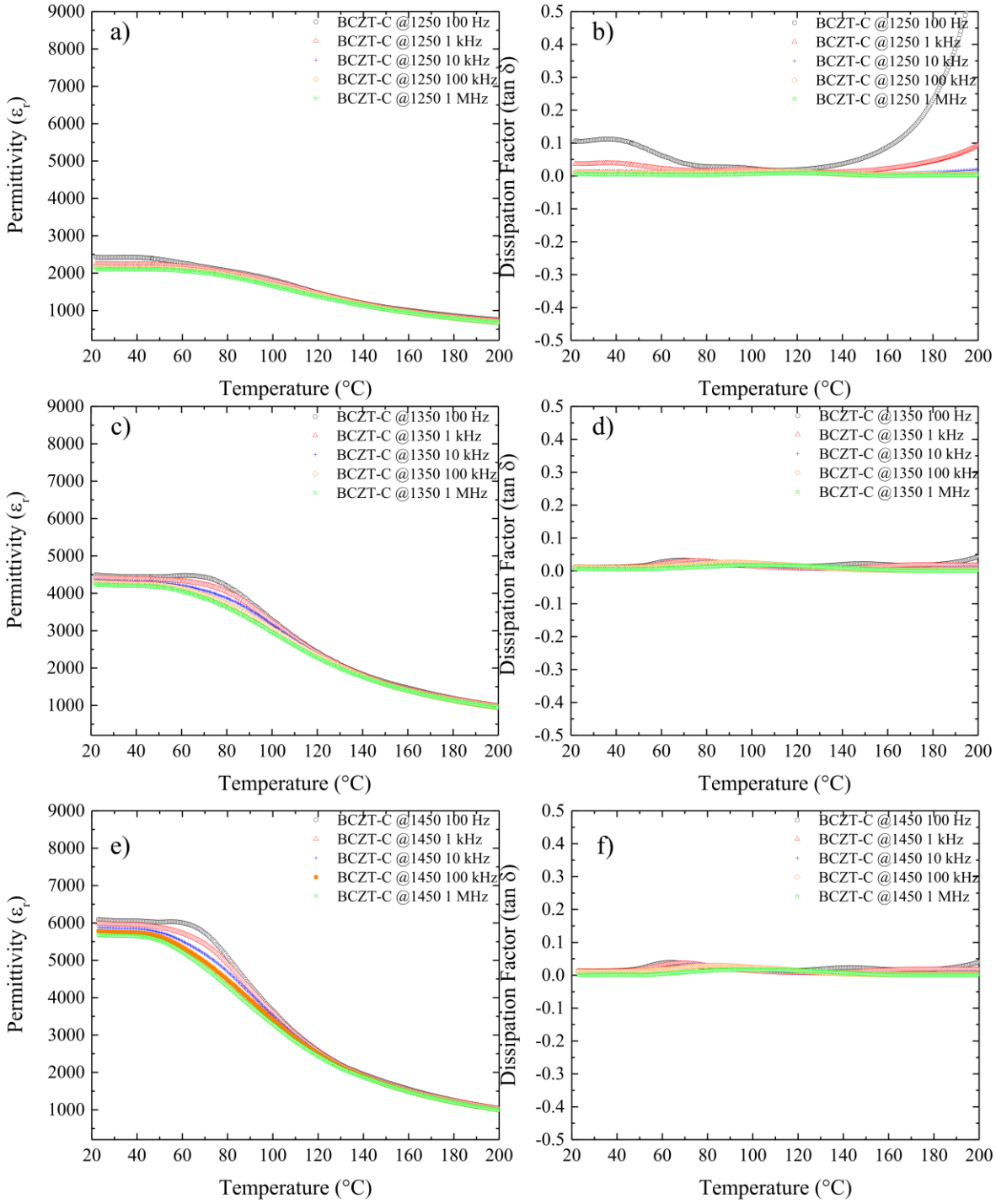

Source: Own authorship

Caption: ε_r and tan δ values as a function of temperature a) ε_r at 1250 ºC, b) respective Tan δ measurements, c) ε_r at 1350 ºC, d) respective Tan δ measurements, e) ε_r at 1450 ºC, and f) respective Tan δ measurements.

Figure 27 – BCZT-D in situ permittivity and tan δ measurements as a function of temperature for several frequencies

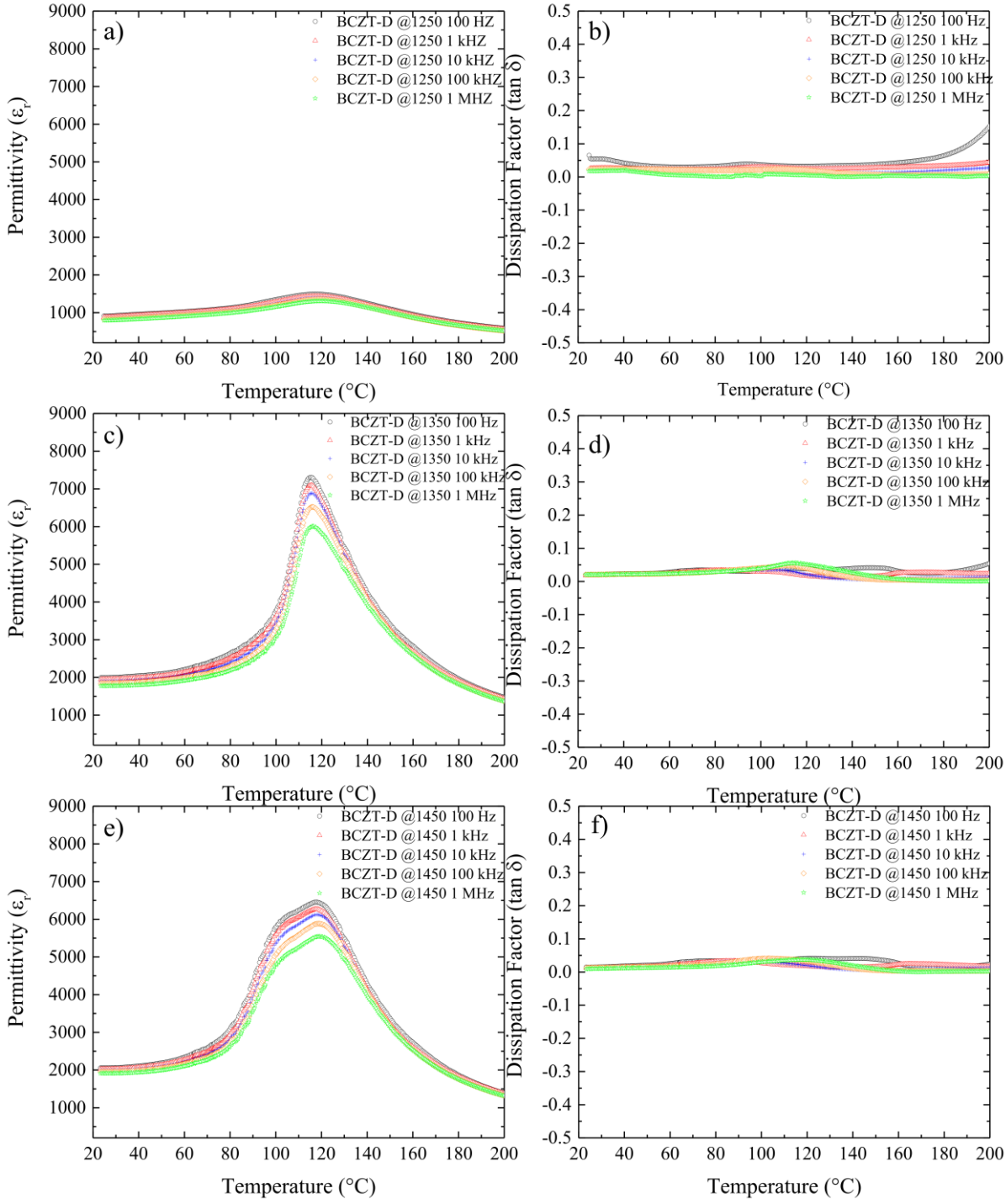

Source: Own authorship

Caption: ε_r and tan δ values as a function of temperature a) ε_r at 1250 °C, b) respective Tan δ measurements, c) ε_r at 1350 °C, d) respective Tan δ measurements, e) ε_r at 1450 °C, and f) respective Tan δ measurements.

All co-doped samples present little dispersion of the point of maximum of ε_r as a function of frequency as well.

Figure 28 – BCZT-AB in situ permittivity and tan δ measurements as a function of temperature for several frequencies

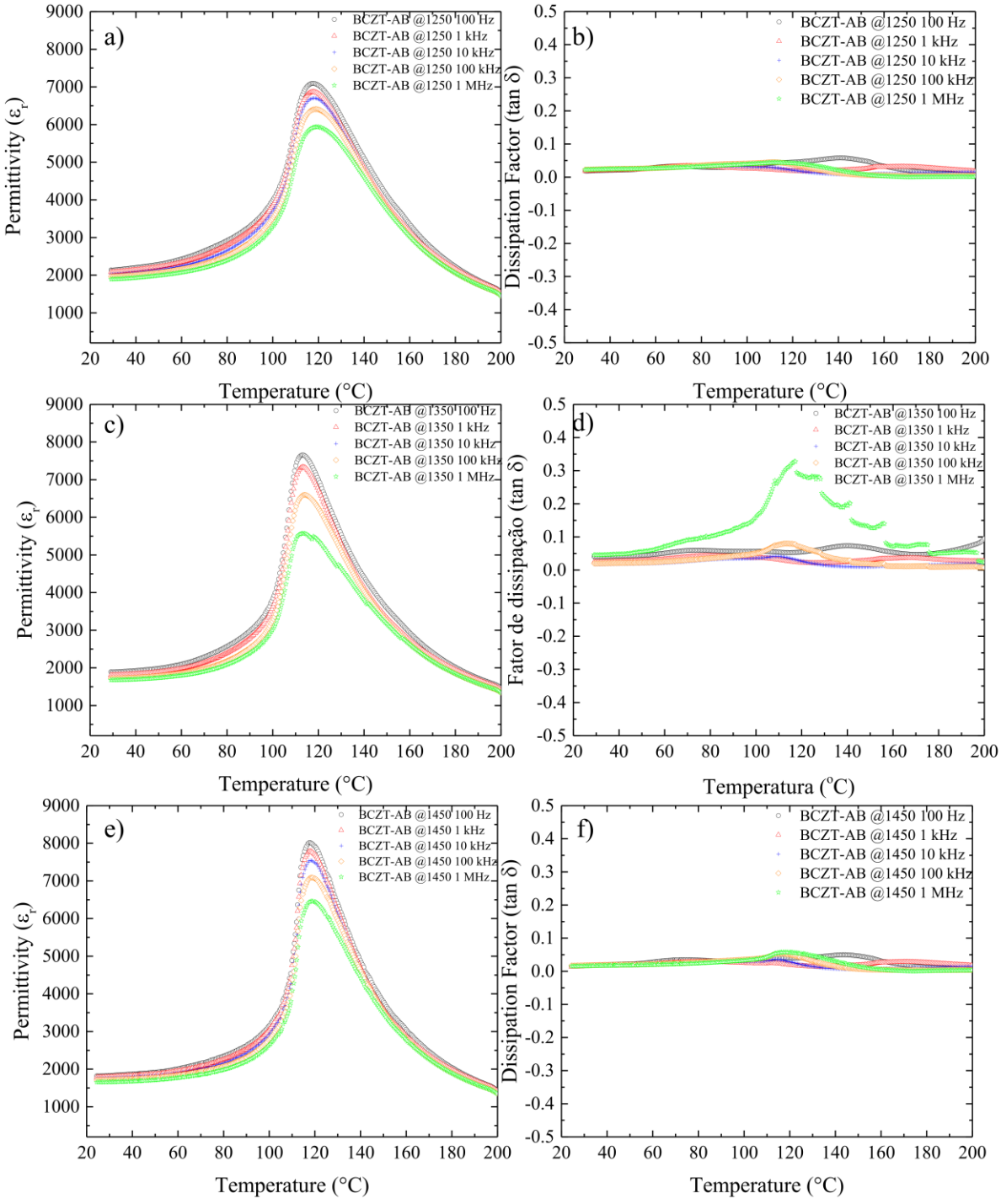

Source: Own authorship

Caption: ε_r and tan δ values as a function of temperature a) ε_r at 1250 °C, b) respective Tan δ measurements, c) ε_r at 1350 °C, d) respective Tan δ measurements, e) ε_r at 1450 °C, and f) respective Tan δ measurements.

Figure 29 – BCZT-AD in situ permittivity and tan δ measurements as a function of temperature for several frequencies

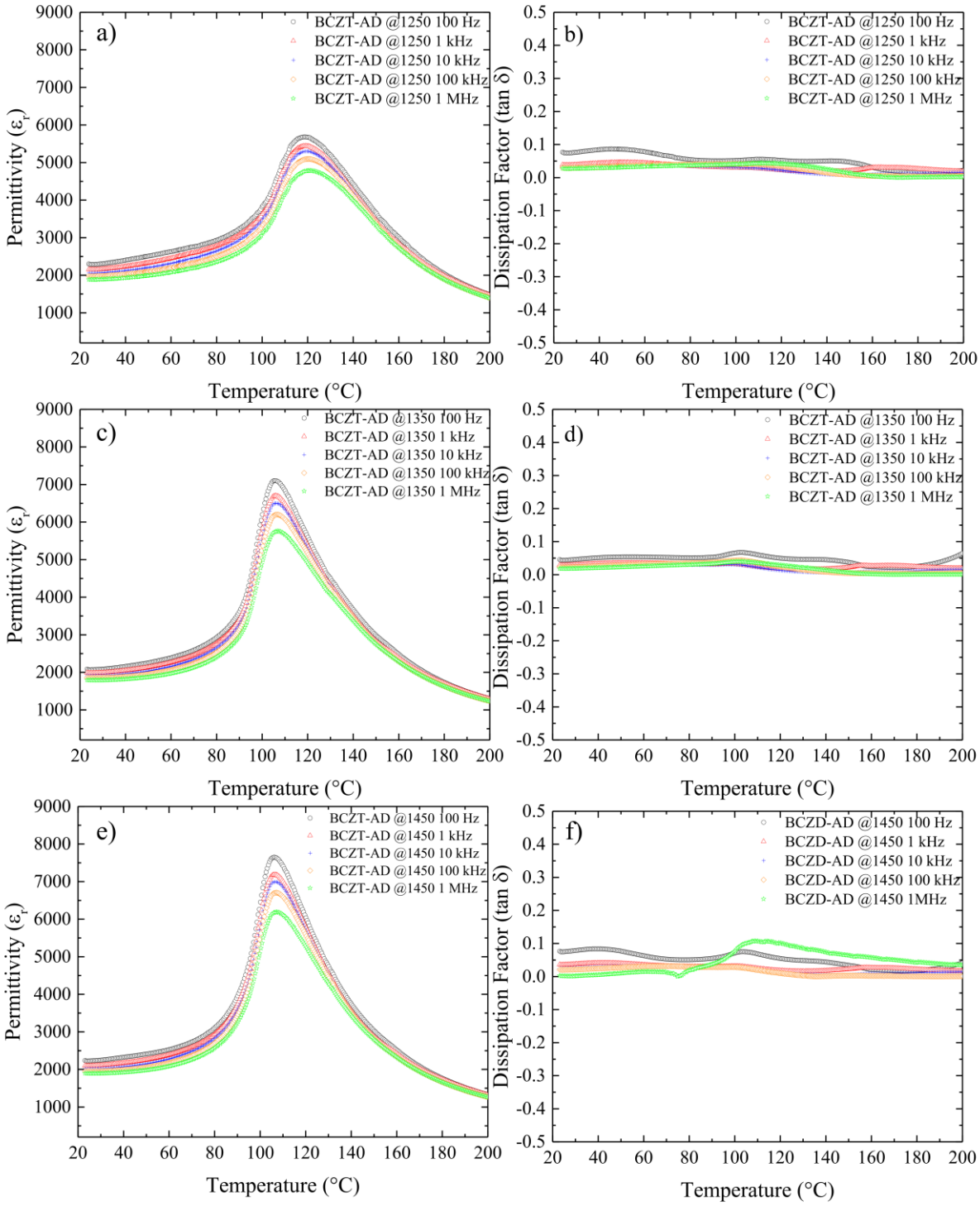

Source: Own authorship

Caption: ε_r and tan δ values as a function of temperature a) ε_r at 1250 ºC, b) respective Tan δ measurements, c) ε_r at 1350 ºC, d) respective Tan δ measurements, e) ε_r at 1450 ºC, and f) respective Tan δ measurements.

Figure 30 – BCZT-CB in situ permittivity and tan δ measurements as a function of temperature for several frequencies

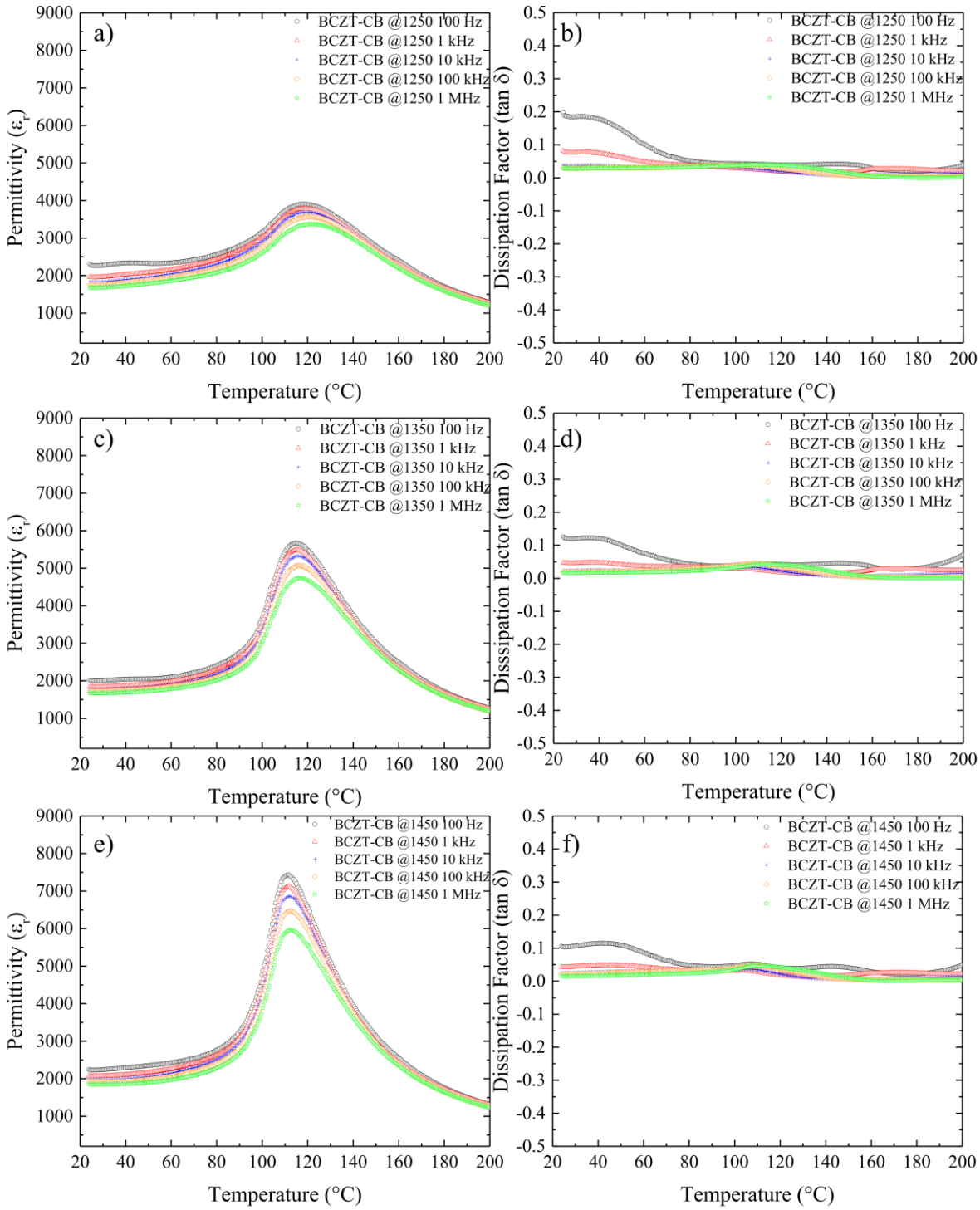

Source: Own authorship

Caption: ε_r and tan δ values as a function of temperature a) ε_r at 1250 ºC, b) respective Tan δ measurements, c) ε_r at 1350 ºC, d) respective Tan δ measurements, e) ε_r at 1450 ºC, and f) respective Tan δ measurements.

Figure 31 – BCZT-CD in situ permittivity and tan δ measurements as a function of temperature for several frequencies

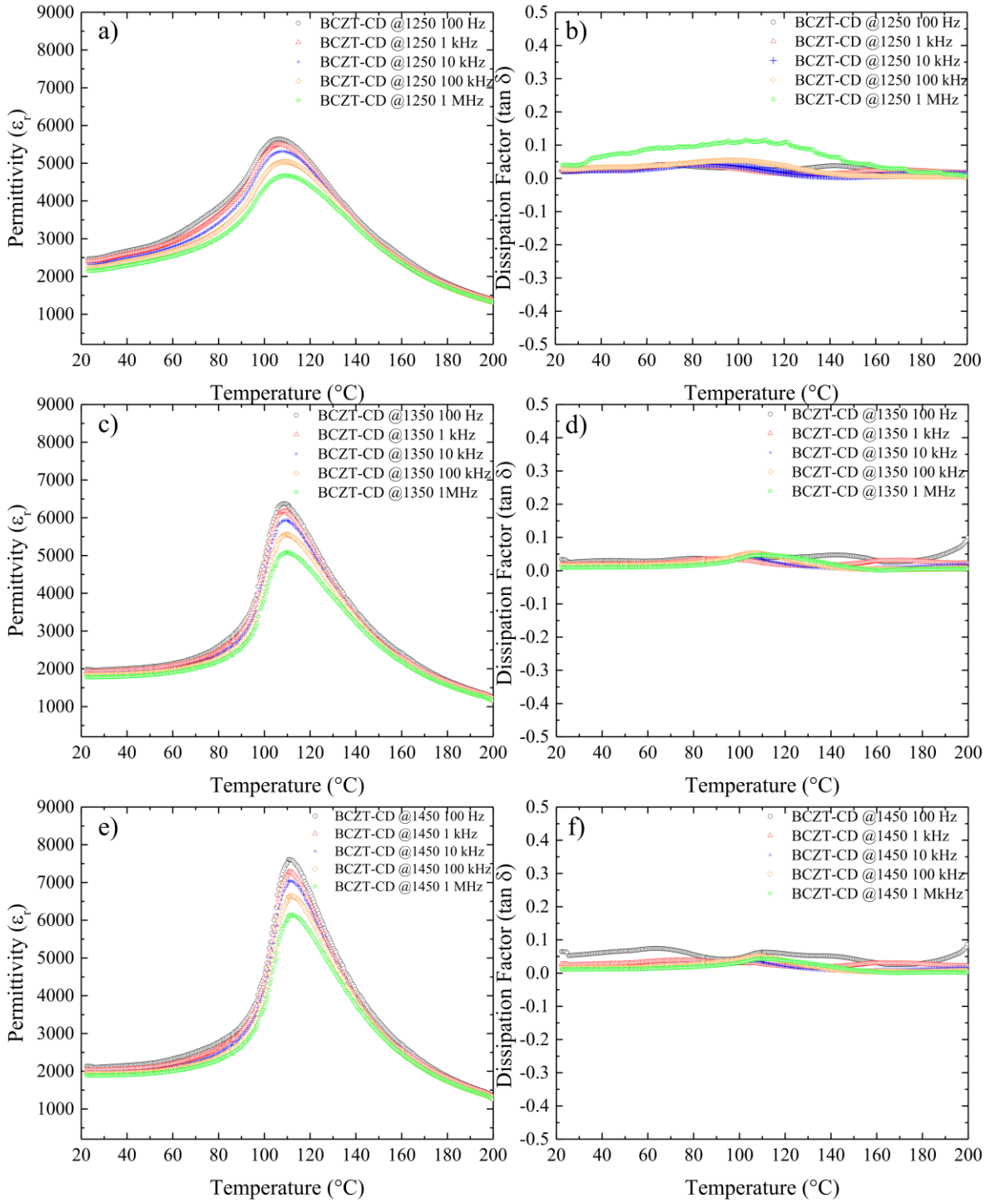

Source: Own authorship

Caption: ε_r and tan δ values as a function of temperature a) ε_r at 1250 ºC, b) respective Tan δ measurements, c) ε_r at 1350 ºC, d) respective Tan δ measurements, e) ε_r at 1450 ºC, and f) respective Tan δ measurements.

To gauge ferroelectric properties and strain response, P-E and S-E hysteresis loops were obtained and shown in Figure 32, Figure 33, Figure 34, Figure 35, Figure 36, Figure 37, Figure 38, Figure 39, and Figure 40.

Figure 32 – P-E and S-E loops of BCZT-U sintered samples

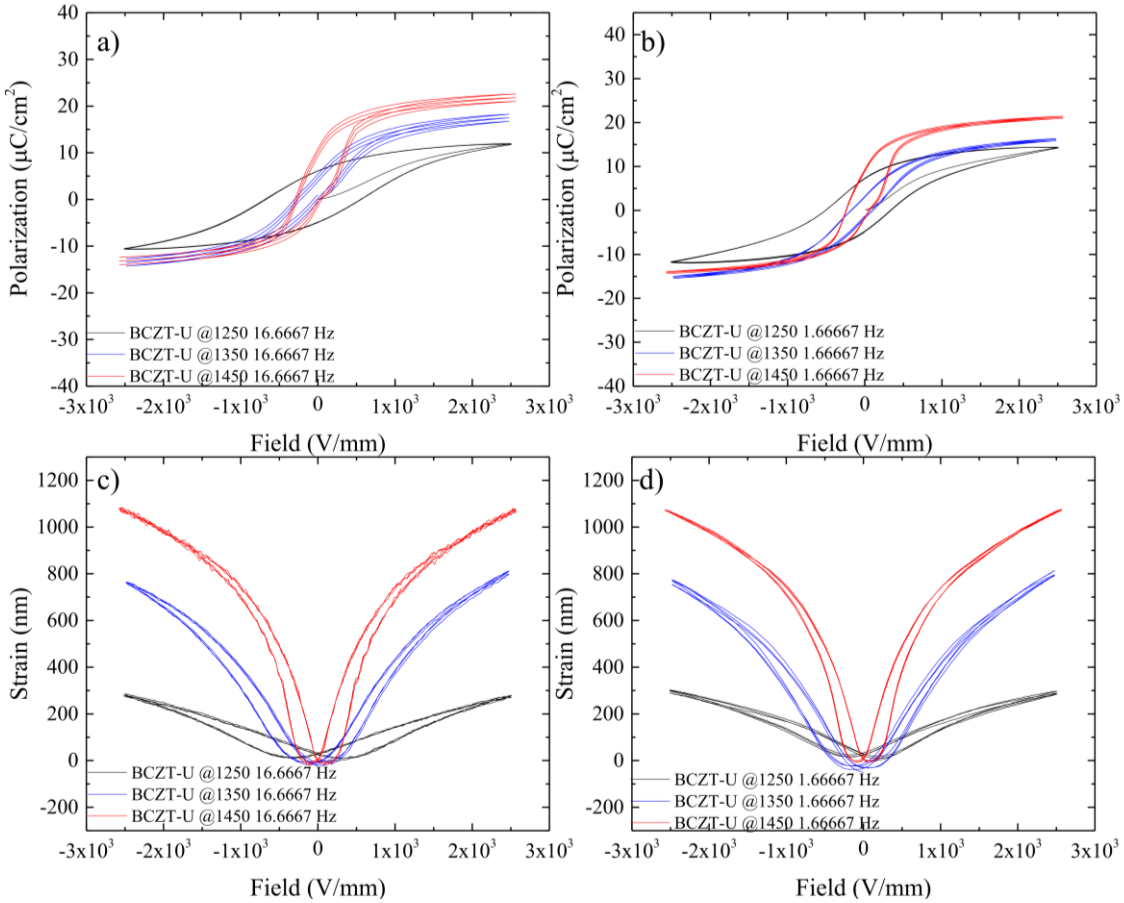

Source: Own authorship

Caption: P-E and S-E loops for the three sintering temperatures carried out, 1250, 1350, and 1450 ºC a) Showcases the P-E loop for the 16.667 Hz frequency b) Showcases the P-E loop for the 1.66667 Hz frequency, c) Showcases the S-E loops for the 16.667 Hz frequency d) Showcases the S-E loops for the 1.66667 Hz frequency.

These measurements were carried out for all sintered samples at room temperature for two different frequencies, 16.667 and 1.66667 Hz. Strain is given as the displacement value in nm. However, there were three exceptions: samples BCZT-A, BCZT-C, and BCZT-D, when sintered at 1250 ºC, the lowest sintering temperature performed, did not present a hysteresis loop potentially due to microstructural features linked to sintering temperature since these samples presented the paraelectric to ferroelectric transition during the in-situ dielectric measurement shown in Figure 22. Another feature present in all samples is the off-center position to the left of the hysteresis loops. This may be caused by the internal bias generated by charged defects. This bias negatively impacts intrinsic and extrinsic contributions to the

piezoelectric and dielectric performances, which can be one of the reasons why the d_{33} values obtained are lower than expected (Luo *et al.*, 2016).

Frequency has a limited effect in both polarization and strain for undoped samples, BCZT-U, cerium-doped samples, BCZT-A and BCZT-C, and vanadium-doped samples, BCZT-B and BCZT-D samples, as seen in Figure 32, Figure 33, Figure 34, Figure 35 and Figure 36. This behavior is overall maintained for co-doped samples, except for the BCZT-CB samples, as seen in Figure 39 b). In these graphs, it is possible to see that the lower frequency, 1.66667 Hz, causes the broadening of the hysteresis loops.

All samples present the characteristic ferroelectric butterfly S-E loops, including the rounded edges featured in polycrystalline materials due to a slower polarization reversal, which can be partially attributed to the randomized configuration of the crystalline axes observed in polycrystalline material (Kao, 2004).

Figure 33 – P-E and S-E loops of BCZT-A sintered samples

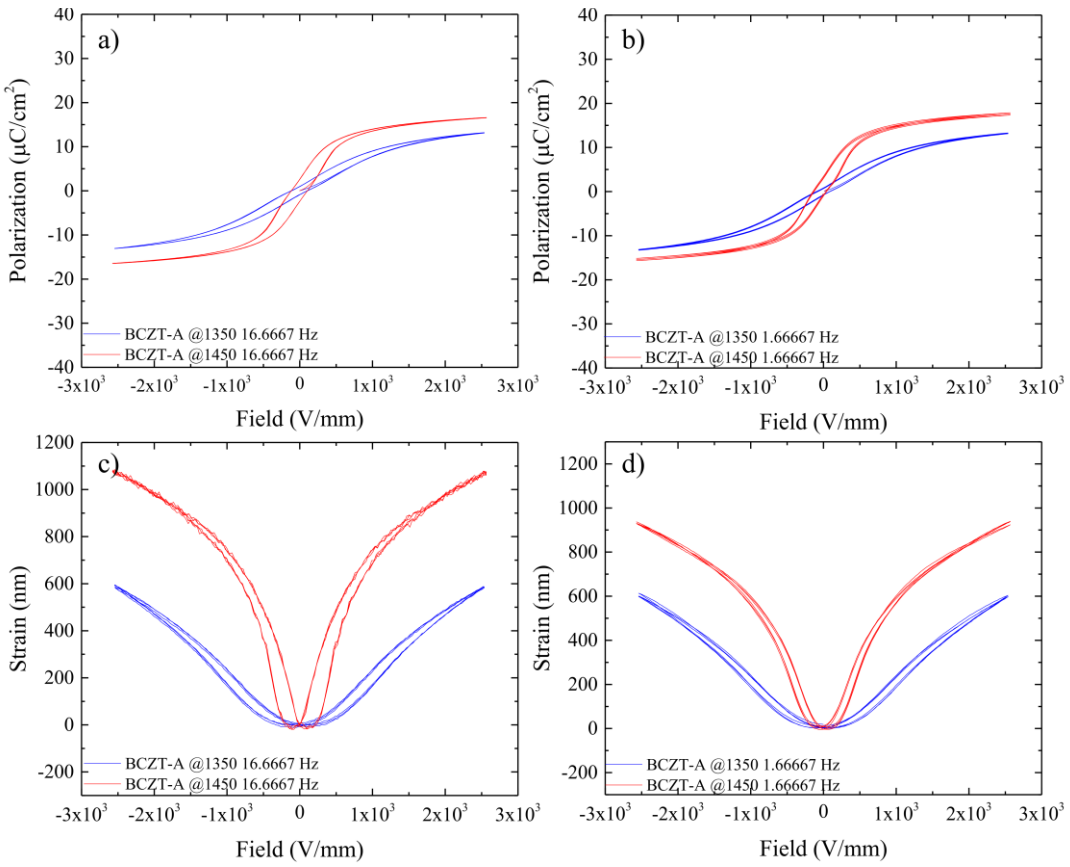

Source: Own authorship

Caption: P-E and S-E loops for two sintering temperatures carried out, 1350 and 1450 ºC a) Showcases the P-E loop for the 16.667 Hz frequency b) Showcases the P-E loop for the 1.66667 Hz frequency, c) Showcases the S-E loops for the 16.667 Hz frequency d) Showcases the S-E loops for the 1.66667 Hz frequency.

Considering the doped and undoped samples, S-E graphs show the effect of sintering temperature. For the BCZT-U and Ce-doped samples, strain response increases as a function of sintering temperature, as seen in Figure 32, Figure 33, and Figure 35 c) and d). However, vanadium-doped samples present stable strain responses regardless of the sintering temperature performed, as seen in Figure 34 and Figure 36 c) and d). Vanadium has a dominant effect in co-doped samples, which means they behave quite similarly to vanadium-doped samples, and sintering temperature has little impact on strain and polarization. Additionally, for all samples, the frequency carried out has little effect on the strain response.

Figure 34 – P-E and S-E loops of BCZT-B sintered samples

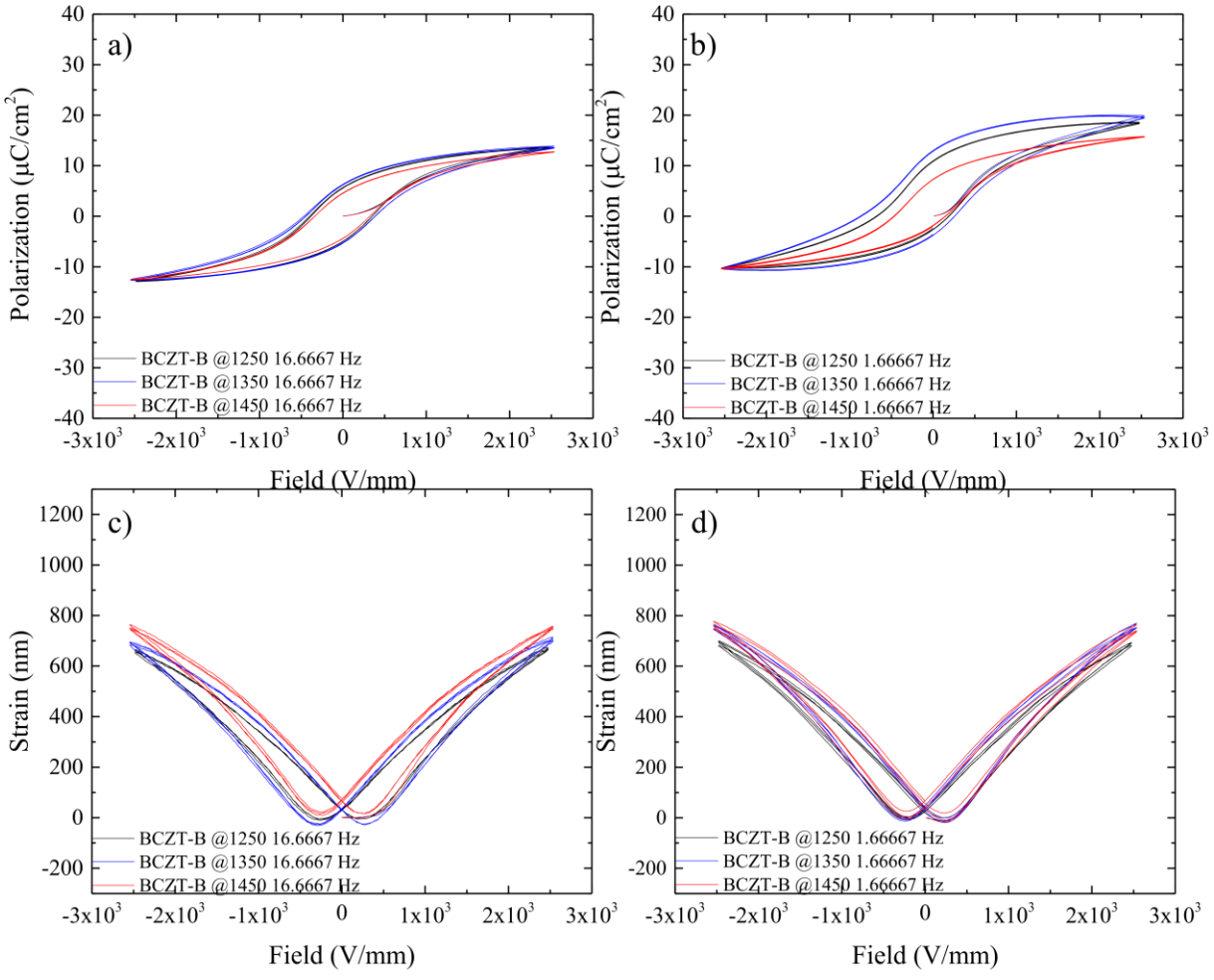

Source: Own authorship

Caption: P-E and S-E loops for the three sintering temperatures carried out, 1250, 1350, and 1450 ºC a) Showcases the P-E loop for the 16.667 Hz frequency b) Showcases the P-E loop for the 1.66667 Hz frequency, c) Showcases the S-E loops for the 16.667 Hz frequency d) Showcases the S-E loops for the 1.66667 Hz frequency.

Considering the magnitude of the strain response, both dopants decrease the strain response to different degrees compared to the undoped BCZT sample, BCZT-U. Ce-doping causes a slight reduction when Ce concentration is high, BCZT-A, and a more acute decrease when Ce concentration is lower, BCZT-C. Vanadium-doping, Figure 34, and Figure 36 causes this same reduction but is independent of concentration. Co-doped samples also present a reduced strain response compared to undoped samples, which varies slightly depending on dopant concentration. However, due to the presence of vanadium, this variation of response between co-doped samples is limited.

Figure 35 – P-E and S-E loops of BCZT-C sintered samples

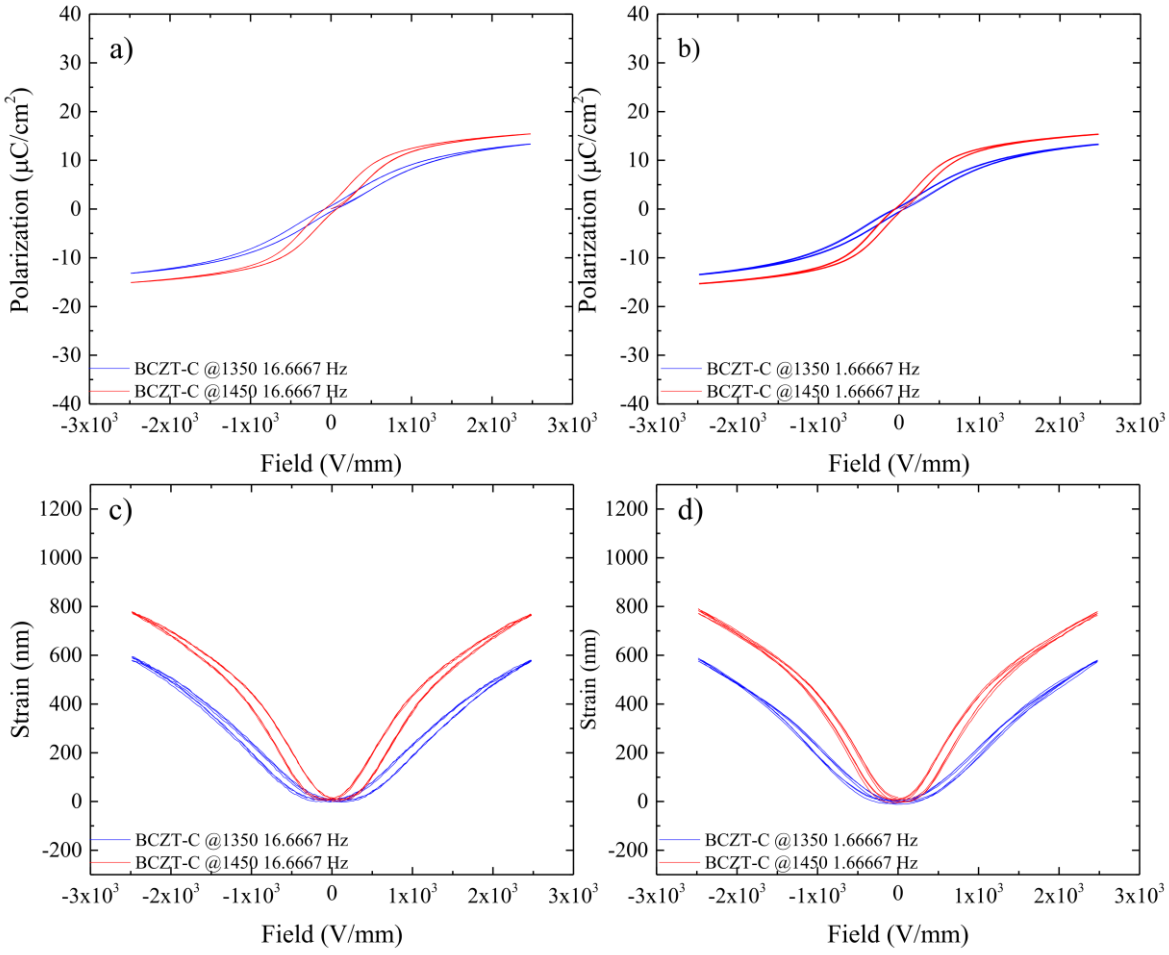

Source: Own authorship

Caption: P-E and S-E loops for two sintering temperatures carried out, 1350 and 1450 ºC a) Showcases the P-E loop for the 16.667 Hz frequency b) Showcases the P-E loop for the 1.66667 Hz frequency, c) Showcases the S-E loops for the 16.667 Hz frequency d) Showcases the S-E loops for the 1.66667 Hz frequency.

Figure 36 – P-E and S-E loops of BCZT-D sintered samples

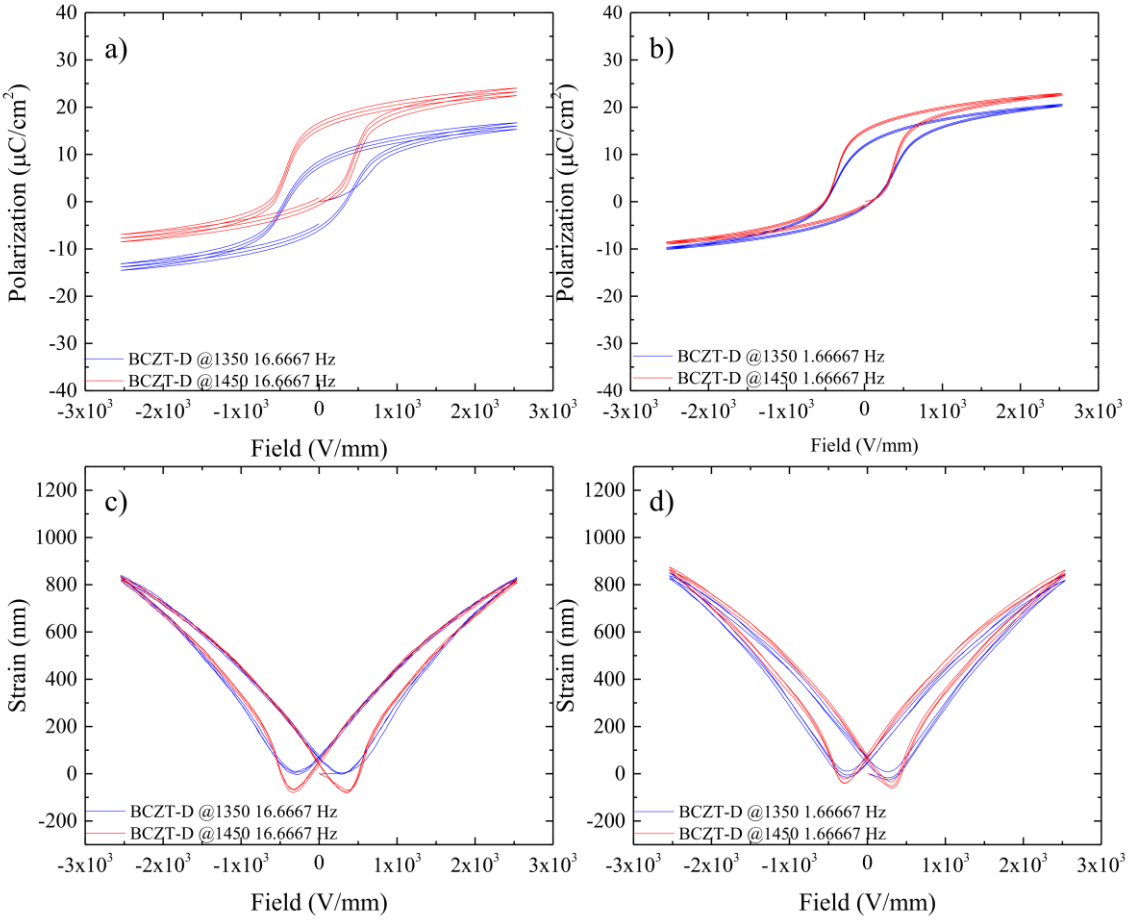

Source: Own authorship

Caption: P-E and S-E loops for the three sintering temperatures carried out, 1250, 1350, and 1450 ºC a) Showcases the P-E loop for the 16.667 Hz frequency b) Showcases the P-E loop for the 1.66667 Hz frequency, c) Showcases the S-E loops for the 16.667 Hz frequency d) Showcases the S-E loops for the 1.66667 Hz frequency.

Figure 37 – P-E and S-E loops of BCZT-AB sintered samples

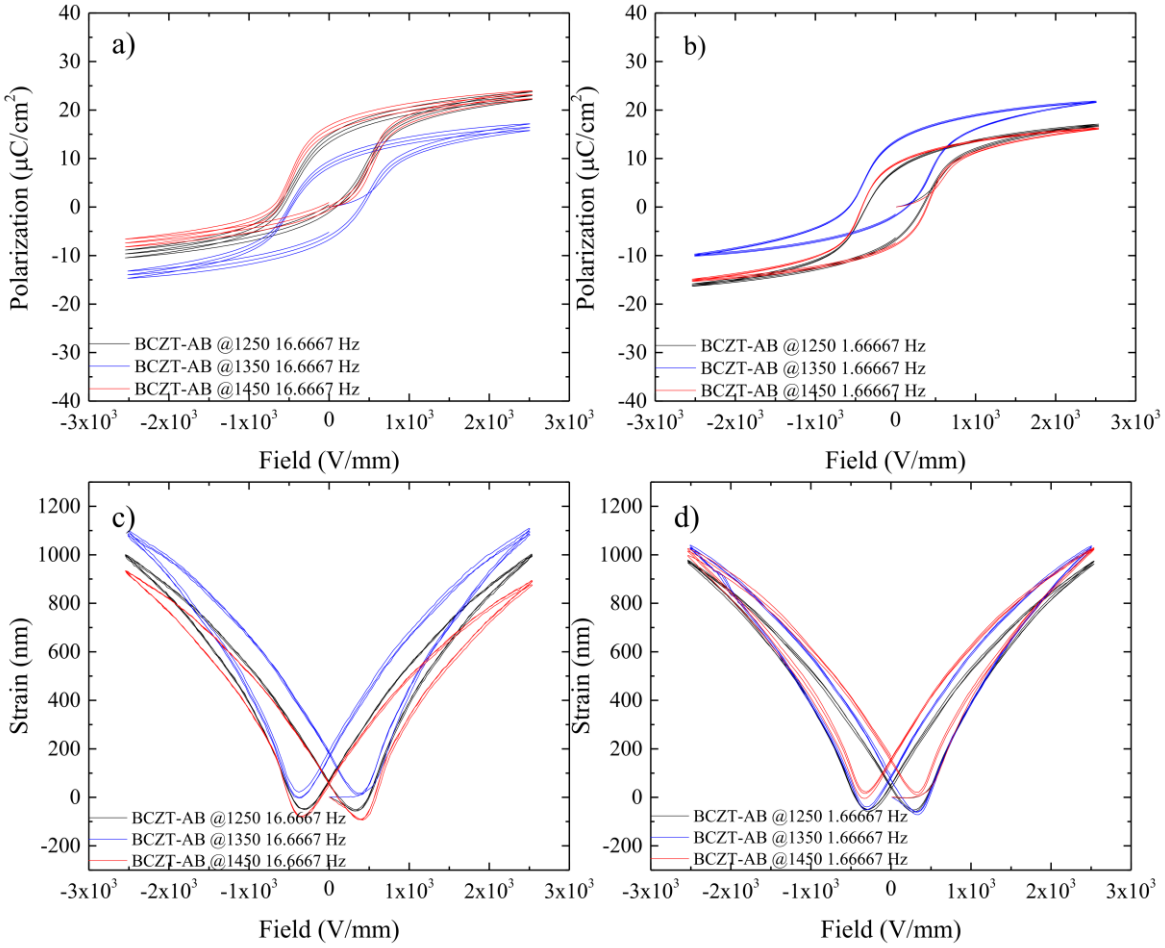

Source: Own authorship

Caption: P-E and S-E loops for the three sintering temperatures carried out, 1250, 1350, and 1450 ºC a) Showcases the P-E loop for the 16.667 Hz frequency b) Showcases the P-E loop for the 1.66667 Hz frequency, c) Showcases the S-E loops for the 16.667 Hz frequency d) Showcases the S-E loops for the 1.66667 Hz frequency.

Figure 38 – P-E and S-E loops of BCZT-AD sintered samples

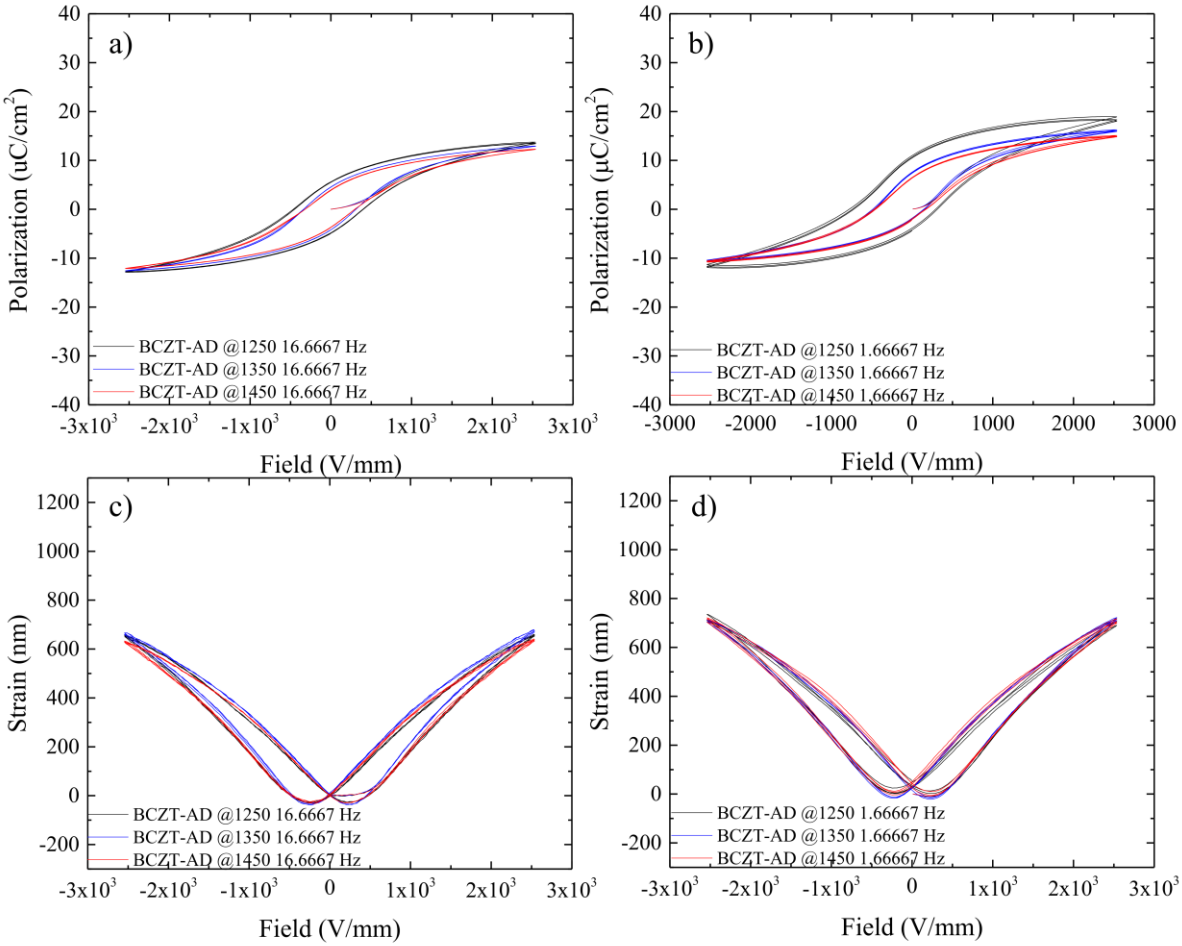

Source: Own authorship

Caption: P-E and S-E loops for the three sintering temperatures carried out, 1250, 1350, and 1450 ºC a) Showcases the P-E loop for the 16.667 Hz frequency b) Showcases the P-E loop for the 1.66667 Hz frequency, c) Showcases the S-E loops for the 16.667 Hz frequency d) Showcases the S-E loops for the 1.66667 Hz frequency.

Figure 39 – P-E and S-E loops of BCZT-CB sintered samples

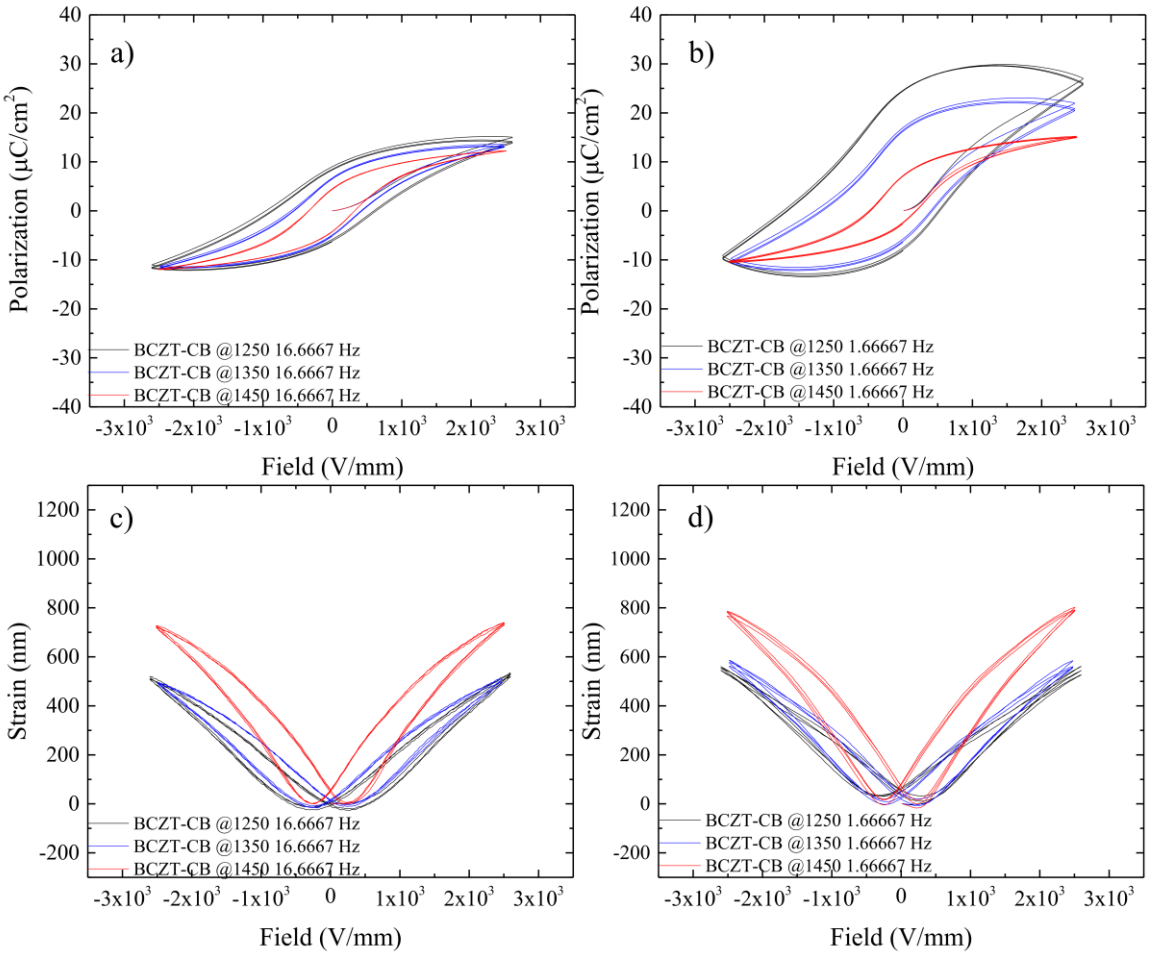

Source: Own authorship

Caption: P-E and S-E loops for the three sintering temperatures carried out, 1250, 1350, and 1450 ºC a) Showcases the P-E loop for the 16.667 Hz frequency b) Showcases the P-E loop for the 1.66667 Hz frequency, c) Showcases the S-E loops for the 16.667 Hz frequency d) Showcases the S-E loops for the 1.66667 Hz frequency.

Figure 40 – P-E and S-E loops of BCZT-CD sintered samples

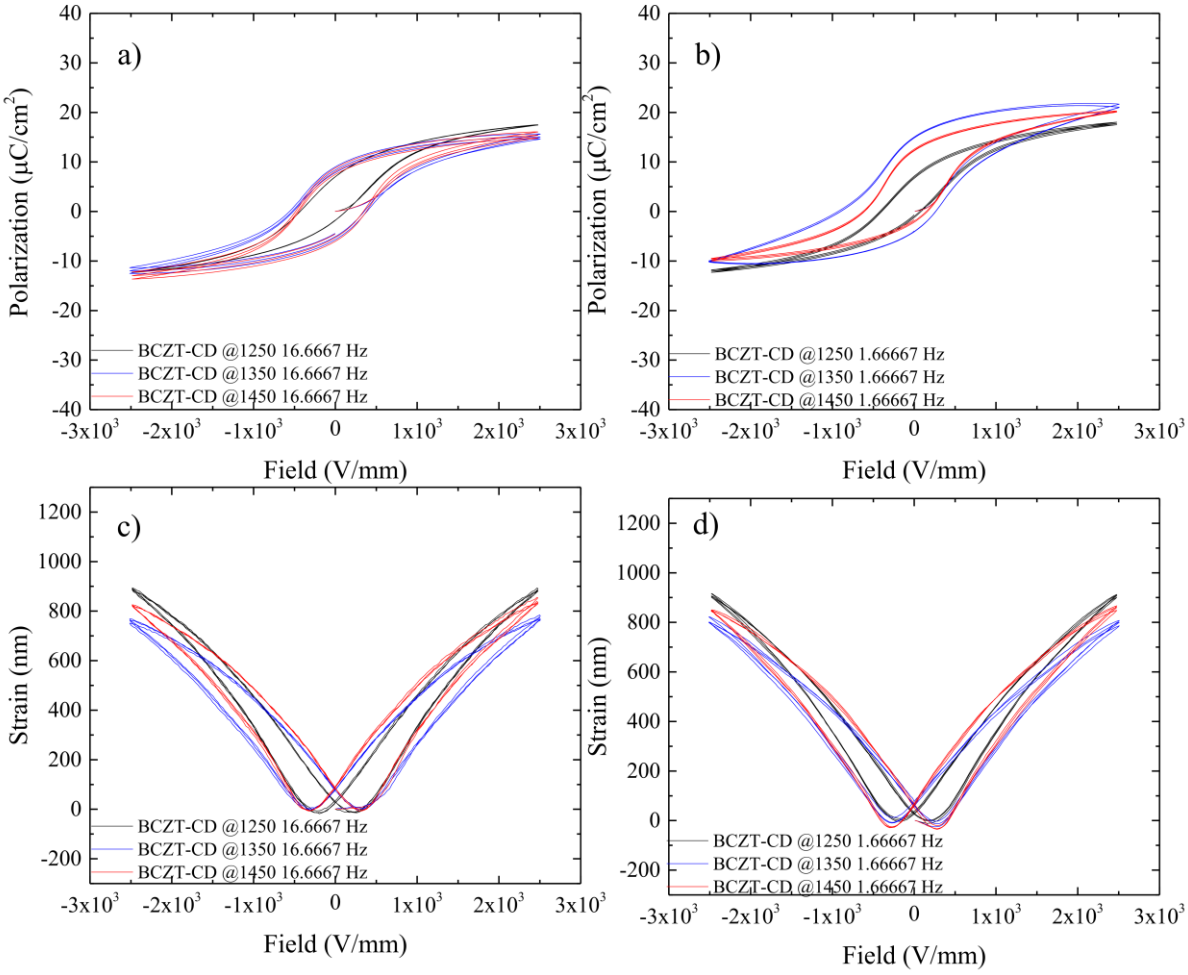

Source: Own authorship

Caption: P-E and S-E loops for the three sintering temperatures carried out, 1250, 1350, and 1450 ºC a) Showcases the P-E loop for the 16.667 Hz frequency b) Showcases the P-E loop for the 1.66667 Hz frequency, c) Showcases the S-E loops for the 16.667 Hz frequency d) Showcases the S-E loops for the 1.66667 Hz frequency.

The important values extracted from the P-E and S-E graphs were tabled in Table 7 to compare the polarization response of all samples.

Regarding remanent polarization, comparing values obtained for BCZT-U, seen in Table 7, to those registered in the scientific literature, the one reported by Liu and Ren, for example, of 16 μC/cm^2 (Liu; Ren, 2009). In addition, considering the doped and co-doped samples and comparing the values measured to the ones from references in Table 2, it is possible to determine that vanadium addition has an overall positive impact on P_r. For doped samples, there is a limited increase in P_r. However, the increase is substantial, reaching up to 24.44 μC/cm^2 for the BCZT-CB sample sintered at 1250 ºC, at 1.6667 Hz. Attesting to the positive influence of vanadium doping, the BCZT-AB samples, also high in vanadium concentration, presented substantial improvement in comparison to undoped BCZT, 13.21 μC/cm^2, when sintering is

carried out at 1250 ºC, 16.667 Hz. It is important to notice that excellent performance can be achieved for BCZT at low sintering temperatures when vanadium doping is performed.

Considering E_c values, seen in Table 7, all samples are soft ferroelectrics, presenting low E_c considering the references in Table 2. This includes the undoped BCZT sample, BCZT-U. However, several doped and co-doped samples present a moderate reduction in E_c when sintered at 1250 ºC compared to BCZT-U. For example, all co-doped samples present lower E_c for both frequencies measured. Ce, however, decidedly has a positive impact in reducing E_c for higher sintering temperatures, unlike vanadium, which only causes a reduction in E_c when the sintering temperature is 1250 ºC. Here, vanadium has a dominant effect, and most co-doped samples follow this pattern. Sintering temperature has little impact on E_c, where V-doped samples are considered.

Table 7 – P-E and S-E results

Sample	Sintering temperature (ºC)	P_{sat} (μC/cm²)		P_r (μC/cm²)		E_c (kV)	
		@16.667 Hz	@1.6667 Hz	@16.667 Hz	@1.6667 Hz	@16.667 Hz	@1.6667 Hz
BCZT-U	1250	10.73	14.48	6.04	7.14	0.682	0.516
	1350	13.70	12.29	3.73	2.98	0.223	0.178
	1450	18.64	18.17	9.14	8.76	0.258	0.241
BCZT-A	1250	-	-	-	-	-	-
	1350	9.61	8.94	0.94	0.613	0.111	0.072
	1450	13.87	14.97	2.54	2.89	0.114	0.127
BCZT-C	1250	-	-	-	-	-	-
	1350	8.81	9.04	0.095	0.256	0.072	0.029
	1450	11.65	11.66	1.02	0.518	0.075	0.040
BCZT-B	1250	10.96	17.59	5.552	10.75	0.381	0.667
	1350	12.26	20.13	6.14	12.95	0.441	0.854
	1450	9.92	12.76	4.53	7.17	0.335	0.459
BCZT-D	1250	-	-	-	-	-	-
	1350	12.18	17.03	7.17	11.54	0.403	0.487
	1450	19.58	19.80	15.12	14.68	0.565	0.496
BCZT-AB	1250	19.28	12.38	13.21	7.41	0.579	0.360
	1350	13.24	19.01	8.02	13.36	0.465	0.569
	1450	19.83	12.81	15.12	8.68	0.628	0.413
BCZT-AD	1250	11.85	18.65	5.48	10.42	0.448	0.719
	1350	10.54	13.08	4.5	7.3	0.332	0.463
	1450	9.68	13.41	3.82	6.29	0.315	0.448
BCZT-CB	1250	15.17	29.44	8.3	24.44	0.854	1.667
	1350	12.83	22.17	6.5	16.2	0.547	1.156
	1450	9.84	10.77	4.36	7.05	0.334	0.463
BCZT-CD	1250	13.43	13.16	6.97	6.63	0.429	0.394
	1350	13.79	20.30	7.79	14.81	0.511	0.894
	1450	12.20	18.05	7.43	12.16	0.445	0.603

Source: Own authorship.

In comparison to other lead-free and lead-based materials, seen in Table 8, the V-doped BCZT samples prepared in this work present properties compatible with conventional lead-free based compositions, although there is still a possibility to improve the piezoresponse with polarization optimization, microstructure engineering, and fine-tuning of V concentration to obtain improved T_C values (Sapkal; Kandasubramanian; Panda, 2022). Especially considering the excellent values of the coercive field and remnant polarization obtained.

Table 8 – Table of properties of piezoelectric materials

Properties	Conventional Lead-free	Lead-based	V-doped samples
d_{33} (PCN^{-1})	Up to 200	Between 200 and 530	Between 20 and 137
Curie temperature (ºC)	Between RT and 500	Between 200 and 450	Between 105 and 120

5 CONCLUSIONS

It has been demonstrated that the doping and co-doping of BCZT by vanadium and cerium can be entirely performed using the sol-gel method without performing any extra steps to add these dopants, which considerably improves over traditional methods. The novel straightforward sol-gel route devised for doping BCZT, followed by calcination at 800 ºC for 5 hours, was successful in inducing the crystallization of the tetragonal perovskite phase, space group *P4mm*, for the whole concentration range studied as XRD measurements and Rietveld analysis have attested it. Sintering at 1250, 1350, and 1450 ºC does not induce any secondary phase or phase transition nucleation. XRD and Rietveld analysis of sintered samples attest to the occupation of vanadium and cerium in the B site, substituting Zr and Ti atoms. Sintering studies determined that vanadium incorporation, even at low concentrations (0.3 and 0.4 mol%), is a powerful tool for lowering the sintering temperature of BCZT. This reduction can be substantial, reaching 200 ºC compared to undoped BCZT. This means a corresponding decrease in the energy necessary to process it, making it more environmentally friendly, especially considering the low calcination temperature employed. Although vanadium doping was shown to improve piezoelectric performance, gauged by d_{33} measurements, all samples underperformed when compared to the usual values observed in scientific literature, which may be attributed to the polarization process parameters and microstructural features, which is corroborated by SEM imaging where non-uniform and finer than ideal grains can be observed. Dielectric measurements attested to the substantial increase in T_C, reaching up to 120 ºC for V-doped samples, consisting of an almost 70% increase compared to undoped BCZT.

Room temperature permittivity values, however, suffer a significant decrease of more than 50% when vanadium doping is performed. Additionally, the in situ dielectric measurements have shown that V-doped samples present a stable dielectric behavior regarding sintering temperature, which means a more stable performance under a temperature gradient. The dissipation factor is low for undoped BCZT, and vanadium and cerium doping have a limited impact on all samples. Frequency-dependent dielectric measurements confirmed that Ce and V-doping do not induce relaxor behavior in BCZT, which is also corroborated by P-E and S-E measurements. P-E and S-E graphs have confirmed that doped BCZT and co-doped BCZT samples present the classical ferroelectric behavior for the concentration range studied, as indicated by the classic non-linearity and hysteresis of the P-E loops and the characteristic butterfly-shaped graphs obtained in S-E measurements. Ce and V doping of BCZT leads to a reduced strain response depending on the dopant concentration. However, co-doped samples may present only a slight reduction for compositions obtained at a substantially lower sintering temperature due to the presence of V. Considering polarization, V-doping can potentially increase remanent polarization in BCZT piezoceramics from 16 to around 24 $\mu C/cm^2$ carrying out less energy-consuming processing. Considering the concentration range studied, vanadium-doping can be an interesting tool in processing BCZT, reducing the energy necessary to obtain ferroelectric samples, increasing thermal stability, causing the softening of BCZT, and potentially increasing remanent polarization. Thus, there is great potential for further in-depth structural investigation of V-doped BCZT combined with additional fine-tuning of V-concentration and sintering parameters allied to further microstructural analysis to obtain a more homogenous microstructure. Additionally, polarization optimization can be investigated to obtain the best possible piezoelectric response and the fine-tuning of V concentration to obtain optimum T_C values.

REFERENCES

ACOSTA, M. *et al.* BaTiO3-based piezoelectrics: Fundamentals, current status, and perspectives. **Applied Physics Reviews**, [*s. l.*], v. 4, n. 4, p. 041305, 2017.

AEGERTER, Michel A.; MENNIG, Martin (org.). **Sol-Gel Technologies for Glass Producers and Users**. Boston, MA: Springer US, 2004. Disponível em: http://link.springer.com/10.1007/978-0-387-88953-5. Acesso em: 23 fev. 2024.

AMERICAN INSTITUTE OF PHYSICS; GRAY, Dwight E. (org.). **American Institute of Physics handbook: Section editors: Bruce H. Billings [and others] Coordinating editor: Dwight E. Gray**. 3d eded. New York: McGraw-Hill, 1972.

AOUJGAL, A. *et al.* Relaxor behavior in (Ba1−3/2Bi)(Zr Ti1−)O3 ceramics. **Ceramics International**, [*s. l.*], v. 37, n. 7, p. 2069–2074, 2011.

BAI, Yang *et al.* (Ba,Ca)(Zr,Ti)O3 lead-free piezoelectric ceramics—The critical role of processing on properties. **Journal of the European Ceramic Society**, [*s. l.*], v. 35, n. 13, p. 3445–3456, 2015.

BAIN, Ashim Kumar; CHAND, Prem. **Ferroelectrics: principles and applications**. Weinheim, Germany: Wiley-VCH, 2017.

BAO, Huixin *et al.* A modified lead-free piezoelectric BZT–xBCT system with higher T_C. **Journal of Physics D: Applied Physics**, [*s. l.*], v. 43, n. 46, p. 465401, 2010.

BAY DE S., Graciano *et al.* Amorphous SiO2 ambigels as hosts for simulated PWR multicomponent nuclear waste. **Journal of Non-Crystalline Solids**, [*s. l.*], v. 461, p. 67–71, 2017.

BELKHADIR, S. *et al.* Impedance spectroscopy analysis of the diffuse phase transition in lead-free (Ba0,85Ca0,15)(Zr0.1Ti0.9)O3 ceramic elaborated by sol-gel method. **Superlattices and Microstructures**, [*s. l.*], v. 127, p. 71–79, 2019.

BIAN, Taiyu; ZHOU, Tianhong; ZHANG, Yang. Preparation and Applications of Rare-Earth-Doped Ferroelectric Oxides. **Energies**, [*s. l.*], v. 15, n. 22, p. 8442, 2022.

BIJALWAN, Vijay *et al.* Rapid pressureless sintering of barium titanate–based piezoceramics and their electromechanical harvesting performance. **Journal of the American Ceramic Society**, [*s. l.*], v. 105, n. 11, p. 6886–6897, 2022.

BIJALWAN, Vijay *et al.* The complex evaluation of functional properties of nearly dense BCZT ceramics and their dependence on the grain size. **Ceramics International**, [*s. l.*], v. 45, n. 1, p. 317–326, 2019a.

BIJALWAN, Vijay *et al.* The effect of sintering temperature on the microstructure and functional properties of BCZT-xCeO2 lead free ceramics. **Materials Research Bulletin**, [*s. l.*], v. 114, p. 121–129, 2019b.

BIJALWAN, Vijay; TOFEL, Pavel. Synthesis of high density sub-10 μm $(Ba_{0.85}Ca_{0.15})(Zr_{0.1}Ti_{0.9})O_3$ -$xCeO_2$ lead-free ceramics using a two-step sintering technique. **Journal of Asian Ceramic Societies**, [*s. l.*], v. 7, n. 4, p. 536–543, 2019.

BIJALWAN, Vijay; TOFEL, Pavel; HOLCMAN, Vladimir. Grain size dependence of the microstructures and functional properties of (Ba $_{0.85}$ Ca $_{0.15-x}$ Ce $_{x}$) (Zr $_{0.1}$ Ti $_{0.9}$) O $_{3}$ lead-free piezoelectric ceramics. **Journal of Asian Ceramic Societies**, [*s. l.*], v. 6, n. 4, p. 384–393, 2018.

BOROWSKI, Maxim (org.). **Perovskites: structure, properties, and uses**. Hauppauge, N.Y: Nova Science Publishers, 2010.

BOWEN, Christopher R.; TOPOLOV, Vitaly Yu.; KIM, Hyunsun Alicia. **Modern Piezoelectric Energy-Harvesting Materials**. Cham: Springer International Publishing, 2016. (Springer Series in Materials Science). v. 238 Disponível em: http://link.springer.com/10.1007/978-3-319-29143-7. Acesso em: 19 fev. 2024.

BRINKER, C. Jeffrey; SCHERER, George W. **Sol-gel science: the physics and chemistry of sol-gel processing**. Boston: Academic Press, 1990.

BUATIP, N. *et al.* Comparison of conventional and reactive sintering techniques for Lead–Free BCZT ferroelectric ceramics. **Radiation Physics and Chemistry**, [*s. l.*], v. 172, p. 108770, 2020.

BUATIP, N. *et al.* Investigation on electrical properties of BCZT ferroelectric ceramics prepared at various sintering conditions. **Integrated Ferroelectrics**, [*s. l.*], v. 187, n. 1, p. 45–52, 2018.

CAIN, Markys G. (org.). **Characterisation of Ferroelectric Bulk Materials and Thin Films**. Dordrecht: Springer Netherlands, 2014. (Springer Series in Measurement Science and Technology). v. 2 Disponível em: https://link.springer.com/10.1007/978-1-4020-9311-1. Acesso em: 18 fev. 2024.

CARDARELLI, François. **Materials Handbook: A Concise Desktop Reference**. Cham: Springer International Publishing, 2018. Disponível em: http://link.springer.com/10.1007/978-3-319-38925-7. Acesso em: 18 fev. 2024.

CHANDRAKALA, Elugu *et al.* Influence of Lattice Strain on Phase Transition and Piezoelectric Properties of Lead-Free (Ba $_{0.85}$ Ca $_{0.15}$)(Zr $_{0.1}$ Ti $_{0.9}$)O $_{3}$ Ceramics. **Transactions of the Indian Ceramic Society**, [*s. l.*], v. 79, n. 3, p. 144–151, 2020.

CHANDRAKALA, Elugu *et al.* Strain-Induced Structural Phase Transition and its Effect on Piezoelectric Properties of (BZT - BCT)-(CeO $_{2}$) Ceramics. **Journal of the American Ceramic Society**, [*s. l.*], v. 99, n. 11, p. 3659–3669, 2016.

CHARLEUX, Bernadette; COPÉRET, Christophe; LACÔTE, Emmanuel (org.). **Chemistry of Organo-Hybrids: Synthesis and Characterization of Functional Nano-Objects**. 1. ed. [*S. l.*]: Wiley, 2014. Disponível em: https://onlinelibrary.wiley.com/doi/book/10.1002/9781118870068. Acesso em: 16 fev. 2024.

CHEN, Tse-Lun *et al.* Implementation of green chemistry principles in circular economy system towards sustainable development goals: Challenges and perspectives. **Science of The Total Environment**, [*s. l.*], v. 716, p. 136998, 2020.

CHEN, Xiaofang; CHAO, Xiaolian; YANG, Zupei. Submicron barium calcium zirconium titanate ceramic for energy storage synthesised via the co-precipitation method. **Materials Research Bulletin**, [*s. l.*], v. 111, p. 259–266, 2019.

COONDOO, Indrani *et al.* A comparative study of structural and electrical properties in lead-free BCZT ceramics: Influence of the synthesis method. **Acta Materialia**, [*s. l.*], v. 155, p. 331–342, 2018.

CUI, Yerang *et al.* Lead-free (Ba0.85Ca0.15)(Ti0.9Zr0.1)O3–CeO2 ceramics with high piezoelectric coefficient obtained by low-temperature sintering. **Ceramics International**, [*s. l.*], v. 38, n. 6, p. 4761–4764, 2012.

CULLITY, Bernard D.; STOCK, Stuart R. **Elements of X-ray diffraction**. 3. ed., new internat. eded. Harlow: Pearson Education, 2014.

DANKS, A. E.; HALL, S. R.; SCHNEPP, Z. The evolution of 'sol–gel' chemistry as a technique for materials synthesis. **Materials Horizons**, [*s. l.*], v. 3, n. 2, p. 91–112, 2016.

FADHLINA, Haziqah; ATIQAH, A.; ZAINUDDIN, Zalita. A review on lithium doped lead-free piezoelectric materials. **Materials Today Communications**, [*s. l.*], v. 33, p. 104835, 2022.

FLEISCH, Daniel A. **A student's guide to Maxwell's equations**. Cambridge, UK ; New York: Cambridge University Press, 2008.

FLUCK, E. Inorganic crystal structure database (ICSD) and standardized data and crystal chemical characterization of inorganic structure types (TYPIX) - Two tools for inorganic chemists. **Journal of Research of the National Institute of Standards and Technology**, [*s. l.*], v. 101, n. 3, p. 217, 1996.

FU, Yongping *et al.* Metal halide perovskite nanostructures for optoelectronic applications and the study of physical properties. **Nature Reviews Materials**, [*s. l.*], v. 4, n. 3, p. 169–188, 2019.

GENENKO, Yuri A. *et al.* Mechanisms of aging and fatigue in ferroelectrics. **Materials Science and Engineering: B**, [*s. l.*], v. 192, p. 52–82, 2015.

H. M. NUSSENZVEIG. **Curso de física básica: eletromagnetismo**. [*S. l.*]: Editora Edgard Blucher, 2022.

HANANI, Z. *et al.* Enhancement of dielectric properties of lead-free BCZT ferroelectric ceramics by grain size engineering. **Superlattices and Microstructures**, [*s. l.*], v. 127, p. 109–117, 2019.

HASSANZADEH-TABRIZI, S.A. Precise calculation of crystallite size of nanomaterials: A review. **Journal of Alloys and Compounds**, [*s. l.*], v. 968, p. 171914, 2023.

HAYATI, Raziye *et al.* Electromechanical properties of Ce-doped (Ba0.85Ca0.15)(Zr0.1Ti0.9)O3 lead-free piezoceramics. **Journal of Advanced Ceramics**, [*s. l.*], v. 8, n. 2, p. 186–195, 2019.

HONG, Chang-Hyo *et al.* Lead-free piezoceramics – Where to move on?. **Journal of Materiomics**, [*s. l.*], v. 2, n. 1, p. 1–24, 2016.

IHLEFELD, Jon F. *et al.* Scaling Effects in Perovskite Ferroelectrics: Fundamental Limits and Process-Structure-Property Relations. **Journal of the American Ceramic Society**, [*s. l.*], v. 99, n. 8, p. 2537–2557, 2016.

IZADI, Rahman *et al.* An inclusive review on inorganic gels: classifications, synthesis methods and applications. **Journal of the Iranian Chemical Society**, [*s. l.*], v. 20, n. 8, p. 1757–1779, 2023.

KADDOUSSI, H. *et al.* Sequence of structural transitions and electrocaloric properties in (Ba1-xCax)(Zr0.1Ti0.9)O3 ceramics. **Journal of Alloys and Compounds**, [*s. l.*], v. 713, p. 164–179, 2017.

KAO, Kwan-Chi. **Dielectric phenomena in solids: with emphasis on physical concepts of electronic processes**. Amsterdam ; Boston: Academic Press, 2004.

KEEBLE, Dean S. *et al.* Revised structural phase diagram of (Ba0.7Ca0.3TiO3)-(BaZr0.2Ti0.8O3). **Applied Physics Letters**, [*s. l.*], v. 102, n. 9, p. 092903, 2013.

KLEIN, Lisa; APARICIO, Mario; JITIANU, Andrei (org.). **Handbook of Sol-Gel Science and Technology: Processing, Characterization and Applications**. Cham: Springer International Publishing, 2018. Disponível em: https://link.springer.com/10.1007/978-3-319-32101-1. Acesso em: 16 fev. 2024.

KOLA, Srimannarayana; RAMESH, K. V.; SWAMY, G. V. Structural Studies of Ce^{4+} Ion Substituted BCZT Perovskite Ceramics. **Integrated Ferroelectrics**, [*s. l.*], v. 237, n. 1, p. 197–207, 2023.

KÖLLNER, David *et al.* Energy-Reduced Fabrication of Light-Frame Ceramic Honeycombs by Replication of Additive Manufactured Templates. **Materials**, [*s. l.*], v. 16, n. 14, p. 4924, 2023.

KOU, Qiangwei *et al.* Tetragonal (Ba, Ca) (Zr, Ti)O3 textured ceramics with enhanced piezoelectric response and superior temperature stability. **Journal of Materiomics**, [*s. l.*], v. 8, n. 2, p. 366–374, 2022.

LACKS, Daniel J.; GORDON, Roy G. Crystal-structure calculations with distorted ions. **Physical Review B**, [*s. l.*], v. 48, n. 5, p. 2889–2908, 1993.

LEVY, David; ZAYAT, Marcos (org.). **The Sol-Gel Handbook**. 1. ed. [*S. l.*]: Wiley, 2015. Disponível em: https://onlinelibrary.wiley.com/doi/book/10.1002/9783527670819. Acesso em: 16 fev. 2024.

LIU, Wenfeng; CHENG, Lu; LI, Shengtao. Prospective of (BaCa)(ZrTi)O3 Lead-free Piezoelectric Ceramics. **Crystals**, [*s. l.*], v. 9, n. 3, p. 179, 2019.

LIU, Wenfeng; REN, Xiaobing. Large Piezoelectric Effect in Pb-Free Ceramics. **Physical Review Letters**, [*s. l.*], v. 103, n. 25, p. 257602, 2009.

LIVAGE, J.; SANCHEZ, C. Sol-gel chemistry. **Journal of Non-Crystalline Solids**, [*s. l.*], v. 145, p. 11–19, 1992.

LÖBMANN, Peer *et al.* Development of ferroelectric aerogels. **Journal of Sol-Gel Science and Technology**, [*s. l.*], v. 16, n. 1/2, p. 173–182, 1999.

LÖBMANN, Peer *et al.* Monolithic crystalline lead zirconate titanate aerogels. **Journal of Non-Crystalline Solids**, [*s. l.*], v. 225, p. 130–134, 1998.

LÖBMANN, Peer; GLAUBITT, Walther; GEIS, Stefan. PZT aerogels: sol-gel derived piezoelectric 3-3 composites. **Journal of Sol-Gel Science and Technology**, [*s. l.*], v. 19, n. 1/3, p. 145–148, 2000.

LUO, Nengneng *et al.* Crystallographic dependence of internal bias in domain engineered Mn-doped relaxor-PbTiO $_3$ single crystals. **Journal of Materials Chemistry C**, [*s. l.*], v. 4, n. 20, p. 4568–4576, 2016.

MAHAJAN, Sandeep *et al.* Study of Structural and Electrical Properties of Conventional Furnace and Microwave-Sintered BaZr $_{0.10}$ Ti $_{0.90}$ O $_3$ Ceramics. **Journal of the American Ceramic Society**, [*s. l.*], v. 92, n. 2, p. 416–423, 2009.

MAHANI, R.M. *et al.* Structure and dielectric behavior of nano-structure ferroelectric BaxSr1−xTiO3 prepared by sol–gel method. **Journal of Alloys and Compounds**, [*s. l.*], v. 508, n. 2, p. 354–358, 2010.

MARQUES, Larissa S. *et al.* Novel Sol-Gel Synthesis Route for Ce- and V-Doped Ba0.85Ca0.15Ti0.9Zr0.1O3 Piezoceramics. **Materials**, [*s. l.*], v. 17, n. 13, p. 3228, 2024.

MCCUSKER, L. B. *et al.* Rietveld refinement guidelines. **Journal of Applied Crystallography**, [*s. l.*], v. 32, n. 1, p. 36–50, 1999.

MEZZOURH, H. *et al.* Enhancing the dielectric, electrocaloric and energy storage properties of lead-free Ba0.85Ca0.15Zr0.1Ti0.9O3 ceramics prepared via sol-gel process. **Physica B: Condensed Matter**, [*s. l.*], v. 603, p. 412760, 2021.

MOMMA, Koichi; IZUMI, Fujio. *VESTA 3* for three-dimensional visualization of crystal, volumetric and morphology data. **Journal of Applied Crystallography**, [*s. l.*], v. 44, n. 6, p. 1272–1276, 2011.

NABAVI, M. *et al.* Chemical modification of metal alkoxides by solvents: A way to control sol-gel chemistry. **Journal of Non-Crystalline Solids**, [*s. l.*], v. 121, n. 1–3, p. 31–34, 1990.

NAVAS, Daniel *et al.* Review on Sol-Gel Synthesis of Perovskite and Oxide Nanomaterials. **Gels**, [*s. l.*], v. 7, n. 4, p. 275, 2021.

PAN, Likun; ZHU, Guang (org.). **Perovskite Materials - Synthesis, Characterisation, Properties, and Applications**. [*S. l.*]: InTech, 2016. Disponível em: http://www.intechopen.com/books/perovskite-materials-synthesis-characterisation-properties-and-applications. Acesso em: 19 fev. 2024.

PANDA, P. K. Review: environmental friendly lead-free piezoelectric materials. **Journal of Materials Science**, [*s. l.*], v. 44, n. 19, p. 5049–5062, 2009.

PRAVEEN, J. Paul *et al.* Effect of poling process on piezoelectric properties of sol–gel derived BZT–BCT ceramics. **Journal of the European Ceramic Society**, [*s. l.*], v. 35, n. 6, p. 1785–1798, 2015.

PYUN, Joo Young; KIM, Young Hun; PARK, Kwan Kyu. Design of Piezoelectric Acoustic Transducers for Underwater Applications. **Sensors**, [*s. l.*], v. 23, n. 4, p. 1821, 2023.

RECHBERGER, Felix *et al.* Assembly of BaTiO $_3$ Nanocrystals into Macroscopic Aerogel Monoliths with High Surface Area. **Angewandte Chemie International Edition**, [*s. l.*], v. 53, n. 26, p. 6823–6826, 2014.

SAHOO, B. *et al.* Effect of dopants on electrical properties of BCT-BZT lead free piezo ceramics: a review. **Ferroelectrics**, [*s. l.*], v. 582, n. 1, p. 46–62, 2021.

SAPKAL, Srujan; KANDASUBRAMANIAN, Balasubramanian; PANDA, Himanshu Sekhar. A review of piezoelectric materials for nanogenerator applications. **Journal of Materials Science: Materials in Electronics**, [*s. l.*], v. 33, n. 36, p. 26633–26677, 2022.

SCHNEIDER, Caroline A; RASBAND, Wayne S; ELICEIRI, Kevin W. NIH Image to ImageJ: 25 years of image analysis. **Nature Methods**, [*s. l.*], v. 9, n. 7, p. 671–675, 2012.

SEKHAR, Madunuri Chandra *et al.* A Review on Piezoelectric Materials and Their Applications. **Crystal Research and Technology**, [*s. l.*], v. 58, n. 2, p. 2200130, 2023.

SEZER, Nurettin; KOÇ, Muammer. A comprehensive review on the state-of-the-art of piezoelectric energy harvesting. **Nano Energy**, [*s. l.*], v. 80, p. 105567, 2021.

SHANNON, R. D.; PREWITT, C. T. Effective ionic radii in oxides and fluorides. **Acta Crystallographica Section B: Structural Crystallography and Crystal Chemistry**, [*s. l.*], v. 25, n. 5, p. 925–946, 1969.

SHAUKAT, Hamna *et al.* Piezoelectric materials: Advanced applications in electro-chemical processes. **Energy Reports**, [*s. l.*], v. 9, p. 4306–4324, 2023.

SHELLAIAH, Muthaiah; SUN, Kien Wen. Review on Sensing Applications of Perovskite Nanomaterials. **Chemosensors**, [*s. l.*], v. 8, n. 3, p. 55, 2020.

SONG, Henan *et al.* Review on the Vibration Suppression of Cantilever Beam through Piezoelectric Materials. **Advanced Engineering Materials**, [*s. l.*], v. 24, n. 11, p. 2200408, 2022.

TICHÝ, Jan *et al.* **Fundamentals of Piezoelectric Sensorics: Mechanical, Dielectric, and Thermodynamical Properties of Piezoelectric Materials**. Berlin, Heidelberg: Springer Berlin Heidelberg, 2010. Disponível em: https://link.springer.com/10.1007/978-3-540-68427-5. Acesso em: 4 nov. 2023.

TILLEY, R. J. D. **Perovskites: structure-property relationships**. First editioned. Chichester, West Sussex, United Kingdom: Wiley, 2016.

TOBY, Brian H.; VON DREELE, Robert B. *GSAS-II* : the genesis of a modern open-source all purpose crystallography software package. **Journal of Applied Crystallography**, [*s. l.*], v. 46, n. 2, p. 544–549, 2013.

UCHINO, Kenji (org.). **Advanced piezoelectric materials: science and technology**. Second editioned. Duxford, United Kingdom: Woodhead Publishing is an imprint of Elsevier, 2017.

VERMA, Ritesh *et al.* Structural, optical, and electrical properties of vanadium-doped, lead-free BCZT ceramics. **Journal of Alloys and Compounds**, [*s. l.*], v. 869, p. 159520, 2021.

VIDYASAGAR, C. C.; MUÑOZ FLORES, Blanca M.; JIMÉNEZ PÉREZ, Víctor M. Recent Advances in Synthesis and Properties of Hybrid Halide Perovskites for Photovoltaics. **Nano-Micro Letters**, [*s. l.*], v. 10, n. 4, p. 68, 2018.

WANG, Xinjian *et al.* Defect engineering of BCZT-based piezoelectric ceramics with high piezoelectric properties. **Journal of Advanced Ceramics**, [*s. l.*], v. 11, n. 1, p. 184–195, 2022.

WANG, Zhongming *et al.* Synthesis, structure, dielectric, piezoelectric, and energy storage performance of (Ba0.85Ca0.15)(Ti0.9Zr0.1)O3 ceramics prepared by different methods. **Journal of Materials Science: Materials in Electronics**, [*s. l.*], v. 27, n. 5, p. 5047–5058, 2016.

WANG, Pan; LI, Yongxiang; LU, Yiqing. Enhanced piezoelectric properties of (Ba0.85Ca0.15)(Ti0.9Zr0.1)O3 lead-free ceramics by optimizing calcination and sintering temperature. **Journal of the European Ceramic Society**, [*s. l.*], v. 31, n. 11, p. 2005–2012, 2011.

WAQAR, Moaz *et al.* Evolution from Lead-Based to Lead-Free Piezoelectrics: Engineering of Lattices, Domains, Boundaries, and Defects Leading to Giant Response. **Advanced Materials**, [*s. l.*], v. 34, n. 25, p. 2106845, 2022.

WU, Jiagang. Perovskite lead-free piezoelectric ceramics. **Journal of Applied Physics**, [*s. l.*], v. 127, n. 19, p. 190901, 2020.

YAMASHITA, Yohachi *et al.* A Review of Lead Perovskite Piezoelectric Single Crystals and Their Medical Transducers Application. **IEEE Transactions on Ultrasonics, Ferroelectrics, and Frequency Control**, [*s. l.*], v. 69, n. 11, p. 3048–3056, 2022.

YANG, Yixuan *et al.* Effects of V2O5 doping on the structure and electrical properties of BCZT lead-free piezoelectric ceramics. **Journal of Materials Science: Materials in Electronics**, [*s. l.*], v. 30, n. 3, p. 2854–2863, 2019.

YOU, Yajun; GUO, Xin. Grain size engineering enhanced dielectric, ferroelectric and energy storage properties in SnO2 modified BCZT lead-free ceramics. **Journal of Alloys and Compounds**, [*s. l.*], v. 918, p. 165557, 2022.

ZHANG, Hongjie *et al.* Electronic structure and photocatalytic properties of copper-doped CaTiO3. **International Journal of Hydrogen Energy**, [*s. l.*], v. 35, n. 7, p. 2713–2716, 2010.

ZHENG, Ting *et al.* Recent development in lead-free perovskite piezoelectric bulk materials. **Progress in Materials Science**, [*s. l.*], v. 98, p. 552–624, 2018.

ZIMMERMAN, Julie B. *et al.* Designing for a green chemistry future. **Science**, [*s. l.*], v. 367, n. 6476, p. 397–400, 2020.